



TECHNISCHE
UNIVERSITÄT
WIEN
Vienna University of Technology

DIPLOMARBEIT

Intra-fraction Tumor Motion Monitoring in Arbitrary Gantry Angles during Radiotherapy Treatments

zur Erlangung des akademischen Grades

Diplom-Ingenieurin

im Rahmen des Studiums

Biomedical Engineering

eingereicht von

Soraya Elmirad

Matrikelnummer 01325173

Ausgeführt am

Zentrum für Medizinische Physik und Biomedizinische Technik
der Medizinischen Universität Wien

in Zusammenarbeit mit dem

Institut für Angewandte Physik der Technischen Universität Wien

Betreuung

Univ.-Prof. Mag. Dr. Wolfgang Birkfellner

Ao.Univ.Prof. Dipl.-Ing. Dr.techn. Martin Gröschl

Hugo Furtado, MSc. PhD.

Wien, 14/09/2021



Die approbierte gedruckte Originalversion dieser Diplomarbeit ist an der TU Wien Bibliothek verfügbar
The approved original version of this thesis is available in print at TU Wien Bibliothek.

Declaration of Authorship

I, Soraya Elmirad, hereby declare, that the following master thesis has been written only by the undersigned and without any assistance from third parties. Furthermore, I confirm that no sources have been used in the preparation of this thesis other than those indicated in the thesis itself.

Soraya Elmirad
14/09/2021

Acknowledgments

I would like to express my deep gratitude to the following people:

Prof. Dietmar Georg for introducing me to the topic at the first place.

Hugo Furtado as my main supervisor, for all his support and his time for guiding me through the topic patiently.

Prof. Wolfgang Birkfellner for his support and his engaging lectures on medical image processing.

Prof. Martin Gröschl as my corresponding supervisor in TU Wien.

Special thanks to the *Center for Medical Physics and Biomedical Engineering* of Medical University of Vienna for providing the infrastructure for my work.

Last but by no means least, I would like to thank my family especially my *parents*, who made it possible for me to study abroad, and my *sister* who has been supporting me throughout my studies without any reservations.

Abstract

Intensity-based 2D-3D registration, using onboard Kilovoltage and Megavoltage imaging, is a promising approach for real-time tumor monitoring to reduce intra-fraction variations in thoracic radiotherapy. This approach has the advantage of being non-invasive, independent of external markers, with no presumption about the patient's breathing pattern. However, when using one projection image set, the motion along the imaging beam axis is not resolved. This study investigates the impact of using additional portal Megavoltage images paired with kV images on registration results at arbitrary gantry angles.

Planning computed tomography and sequences of Kilovoltage and Megavoltage images were obtained for five patients suffering from non-small cell lung cancer undergoing stereotactic body radiation therapy. FIRE, an open-source software, was used for the 2D-3D registration of x-ray sequences with the digitally reconstructed radiographs of the region of interest encompassing tumors. The registration results, holding the motion in the craniocaudal and anteroposterior axis, were plotted against a reference signal, and their similarities were validated numerically using the correlation coefficient.

The results suggested that unsuccessful registration using only Kilovoltage images benefited from an additional Megavoltage image set. Using kV-MV image pairs, the craniocaudal motion, as the dominant motion axis, as well as the anteroposterior motion were extracted. A large number of configuration parameters influenced the registration outcome though tumor visibility within the selected region of interest was the main critical factor for the success of registration. Consequently, using two orthogonal projection image sets increased the overall chance of tumor visibility for the majority of gantry angles. A potent weighting factor, in favor of the projection image set with better tumor visibility, could be introduced in the future to further improve the registration results.

Kurzfassung

Die intensitätsbasierte 2D-3D-Registrierung, unter Verwendung von Onboard-Kilovolt- und Megavolt-Bildgebung, ist ein vielversprechender Ansatz für das Echtzeit Tumor-monitoring, um die intrafraktionelle Variation bei der thorakalen Strahlentherapie zu reduzieren. Dieser Ansatz hat den Vorteil, dass er nicht invasiv und unabhängig von externen Markern ist, und Annahmen über das Atemmuster des Patienten auskommt. Bei Verwendung eines Projektionsbildsatzes wird jedoch die Bewegung entlang der Abbildungsstrahlachse nicht aufgelöst. Diese Studie untersucht die Auswirkungen der Verwendung zusätzlicher Portal-Megavolt-Bilder gekoppelt mit kV-Bildern auf Registrierungsergebnisse bei beliebigen Gantry-Winkeln.

Planungscomputertomographie und Sequenzen von Kilovolt- und Megavolt-Bildern wurden für fünf Patienten mit nicht-kleinzelligem Lungenkrebs, die sich einer stereotaktischen Körperbestrahlungstherapie unterzogen, erhalten. FIRE, eine Open-Source-Software, wurde für die 2D-3D-Registrierung von Röntgensequenzen mit den digital rekonstruierten Röntgenbildern der relevanten Region mit Tumoren verwendet. Die Registrierungsergebnisse für die Bewegung in der kраниокаудalen und anteroposterioren Achse wurden gegen ein Referenzsignal aufgetragen und ihre Ähnlichkeiten wurden numerisch mit dem Korrelationskoeffizienten validiert.

Die Ergebnisse deuten an, dass erfolglose Registrierungen mit nur Kilovolt-Bildern von einem zusätzlichen Megavolt-Bildersatz profitierten. Unter Verwendung von kV-MV-Bildpaaren wurden die kраниокаудale Bewegung als dominante Bewegungsachse sowie die anteroposteriore Bewegung extrahiert. Eine große Anzahl von Konfigurationsparametern beeinflusste das Registrierungsergebnis, obwohl die Sichtbarkeit des Tumors innerhalb der ausgewählten Region der Hauptkritikfaktor für den Erfolg der Registrierung war. Folglich erhöhte die Verwendung von zwei orthogonalen Projektionsbildsätzen die Gesamtwahrscheinlichkeit der Tumorsichtbarkeit für die Mehrheit der Gantry-Winkel. Ein potenter Gewichtungsfaktor zugunsten des Projektionsbildsatzes mit besserer Tumorsichtbarkeit könnte in Zukunft eingeführt werden, um die Registrierungsergebnisse weiter zu verbessern.

Foreword

This master thesis is organized into six chapters:

Chapter one, *Introduction*, provides an introduction to radiation therapy with a focus on image-guided radiotherapy. Uncertainties in radiotherapy and motion management strategies are described, followed by the objective of this thesis.

Image registration is a significant part of this thesis, thus, *Image Registration - Theoretical Background* in Chapters two is devoted to explaining the necessary steps for 2D-3D registration of medical images. This chapter also outlines an overview of the image registration classification as well as validation methods.

Chapter three, *Lung Cancer Patient Study - Methods*, elaborates the proposed workflow, starting with the patient data, the required pre-processing steps, and utilized software and hardware. Then it continues with the description of the 2D-3D registration process.

The correlation coefficient of the registration result with the diaphragm motion serving as our reference signal is reported in chapter four, *Results*. For a visual evaluation, all the plots are presented in the appendix.

Chapter five, *Discussion*, is devoted to the evaluation and interpretation of the results. Finally, Chapter six, *Conclusion*, draws a conclusion with suggestions for future improvement.

Contents

Contents	vi
List of Figures	viii
List of Tables	x
1 Introduction	1
1.1 Radiation Therapy	1
1.1.1 Clinical Workflow in EBRT	3
1.1.2 Treatment Techniques in EBRT	7
1.1.3 Image Guidance Technologies	8
1.2 Uncertainty in Radiotherapy	13
1.2.1 Radiography Margins	16
1.2.2 Patient Positioning and Immobilization	19
1.2.3 Respiratory Motion Management	21
1.3 Motivation: Lung Cancer IGRT	26
2 Image Registration - Theoretical Background	31
2.1 Classification of Image Registration Methods	32
2.2 2D - 3D Intensity-based Registration	35
2.2.1 DRR	35
2.2.2 Merit Function	36
2.2.3 Optimization	38
2.3 Evaluation of Registration Result	41
3 NSCLC Patient Study - Material and Methods	43
3.1 Patient Data	43
3.2 Soft- and Hardware	45
3.3 Workflow	46
3.3.1 Data Preprocessing	46
3.3.2 3D-3D Registration	46
3.3.3 Mask Generation	47
3.3.4 Motion Extraction	49
3.3.5 kV - MV Correlation	52
3.4 2D - 3D Registration	54

3.5	Registration Result	58
3.5.1	Qualitative Evaluation of Results	59
3.5.2	Quantitative Evaluation of Results	60
4	Results	61
5	Discussion	67
6	Conclusion	80
6.1	Tumor Illustration with MV Projections	82
6.2	Patient 2	83
6.3	Patient 5	89
6.4	Patient 6	95
6.5	Patient 9	97
6.6	Patient 12	103
	Bibliography	109

List of Figures

1.1	Dose-Depth Curve	2
1.2	Elekta Synergy system and its components	3
1.3	DICOM data transfer	4
1.4	Clinical workflow of EBRT	5
1.5	Examples of radiation-based IGRT systems	12
1.6	Examples of physiological changes	13
1.7	Error comparison in online and offline correction protocols	14
1.8	PTV margins in different correction protocols	16
1.9	ICRU volume definition	18
1.10	Examples of different breathing pattern	22
1.11	Variation in tumor trajectories	23
2.1	The basic process of image registration algorithm	31
2.2	2D-3D registration methods	34
2.3	Illustration of downhill simplex method	40
2.4	Examples of qualitative measures for registration result evaluation	42
3.1	Tumor position in the studied patients	44
3.2	Registration interface in Analyze	47
3.3	Example of delineated structures on a kV image	48
3.4	Mask annotation in Matlab	48
3.5	Diaphragm motion extraction with Hough transform and edge detection	50
3.6	Example of extracted motion signal	51
3.7	The process of kV-MV image pair alignment	53
3.8	Configuration tab in FIRE	54
3.9	Registration tab in FIRE	55
3.10	Corresponding image pair in FIRE before mask application	56
3.11	Workflow of registration in FIRE	57
3.12	Batch Registration tab in FIRE	58
3.13	Translational and rotational parameters of registration result	59
5.1	kV-MV image pair	69
5.2	Examples of extracted diaphragm motion	72
5.3	CC motion displacement in kV images	76

5.4	Examples of MV image contribution	76
5.5	Performance of merit function	77
5.6	Comparison of merit function performance	78

List of Tables

1.1	Comparison of different methods of respiratory motion control	26
2.1	Summary of registration classification	32
2.2	Quantitative metrics for image registration evaluation	42
4.1	Patient 2 _ Summary of Results	62
4.2	Patient 5 _ Summary of Results	63
4.3	Patient 6 _ Summary of Results	64
4.4	Patient 9 _ Summary of Results	65
4.5	Patient 12 _ Summary of Results	66

List of Abbreviations

2D	Two-dimensional
3D	Three-dimensional
4D	Four-dimensional
4DCT	Four-dimensional Computed Tomograph
ABC	Active Breathing Control
AP	Anterior-posterior
ART	Adaptive Radiotherapy
CBCT	Cone Beam CT
CC	Cranial-caudal
CT	Computed Tomograph
CTV	Clinical Target Volume
DIBH	Deep Inspiration Breath Hold
DICOM	Digital Imaging and Communications in Medicine
DNA	Deoxyribonucleic Acid
DOF	Degrees-of-freedom
DRR	Digitally Reconstructed Radiograph
DVH	Dose Volume Histogram
EBRT	External Beam Radiotherapy
EPID	Electronic Portal Imaging Device
FIRE	Fast Image Registration
Fr.	Fraction
G.a.	Gantry Angle

GTV	Gross Tumor Volume
Gy	Gray
Hz	Herz
IGRT	Image Guided Radiotherapy
IM	Internal Margin
IMRT	Intensity Modulated Radiotherapy
ITV	Internal Target Volume
kV	Kilovoltage
Linac	Linear Accelerator
MIP	Maximum Intensity Projection
ML	Medio-lateral
MLC	Multi-leaf Collimator
MV	Megavoltage
NAL	No Action Level
NifTI	Neuroimaging Informatics Technology Initiative
NSCLC	Non-small Cell Lung Cancer
OAR	Organ at Risk
PGM	Portable Gray Map
PRV	Planning Organ at Risk Volume
PTV	Planning Target Volume
ROI	Region of Interest
s	Second
SAL	Shrinking Action Level
SBRT	Stereotactic Body Radiotherapy
SM	Set-up Margin
TPS	Treatment Planning System
VMAT	Volumetric Modulated Arc Therapy



Die approbierte gedruckte Originalversion dieser Diplomarbeit ist an der TU Wien Bibliothek verfügbar
The approved original version of this thesis is available in print at TU Wien Bibliothek.

1 Introduction

1.1 Radiation Therapy

Radiation therapy refers to the application of ionizing radiation from photons, electrons, protons, or heavy ions in cancer treatment. The goal of radiotherapy is to deliver enough dose to the tumor while sparing normal tissue. Different types of radiation show different properties and consequently adopted for various applications:

- **Indirect Ionizing Radiation with neutral particles**

High energy gamma and x-ray radiations are produced with a linear accelerator (Linac). The produced beam is then used for destroying malignant cells by damaging their deoxyribonucleic acid (DNA) directly or by the generation of free radicals that will later damage the genetic structure of the cell.

- **Direct Ionizing Radiation with charged particles**

Charged particles such as electrons, protons, or heavy ions deliver similar results but with a different depth-dose-profile. Electron radiation is absorbed in a short distance and, only a minimal dose remains. Its main application is for superficial tumors, with an advantage for tumors situated in front of a sensible structure. On the other hand, targeted dose delivery to the tumor and less dose to the tissue surrounding the tumor are the main features of radiotherapy with protons and heavy ions. This is explained by the so-called Bragg peak effect. Application of heavier charged particles in radiotherapy is less common because they require more complex and expensive equipment.

As shown in figure 1.1, x-ray photons deliver their maximum dose at a much shorter distance than protons. Another difference is dose contribution in photon radiotherapy after maximum dose decreases slowly over the whole range while it decreases rapidly for the proton with much higher energy. Electrons have the shortest penetration depth but a very focused dose delivery with almost no remaining dose after their maximum dose.

Radiation therapy is characterized according to the delivery of the radiation source:

- **External Beam Radiotherapy (EBRT)**

One or more irradiating beam originating from a radiation source outside of the patient body is aimed at the target volume by passing through the healthy tissue. External beam radiotherapy is carried out mainly with an x-ray machine, Cobalt 60, or linac equipment, producing either x rays or electron beam for clinical use.

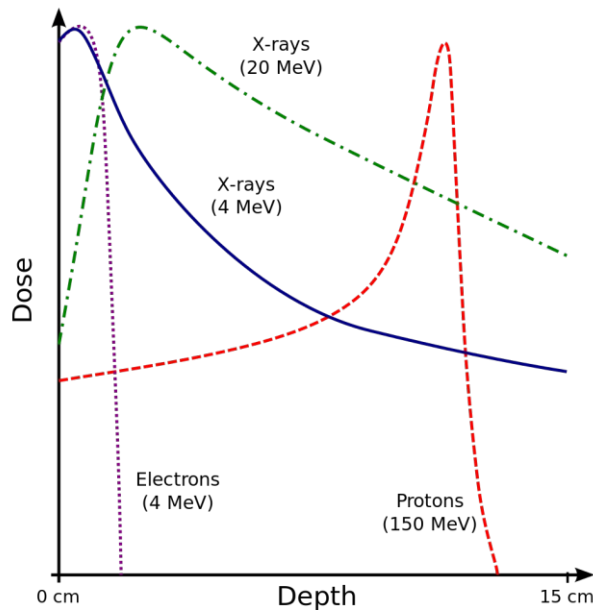


Figure 1.1: Dose-Depth-Curve for x-rays in green and blue, electrons in purple, and protons in red. (Figure from [57])

- **Brachytherapy**

A small radioactive source is inserted into the tumor or placed in a body cavity. This source can be removed after a certain amount of time or implanted as the radionuclide activity decreases constantly. It provides a localized solution for some cancers such as breast, prostate, and cervical cancer.

- **Radioisotope Therapy**

It uses the functionality of metabolism and circulation to deliver isotopes to specific target regions. Isotopes are delivered to the patient by infusion or oral ingestion. A well-known example is iodine therapy, which is specifically absorbed in the thyroid gland, used in thyroid cancer treatment.

Radioisotope sources like cesium, or cobalt, radiate all the time but because of problems concerning the acquisition, handling, and disposal of radioactive material, they are mainly replaced by linear accelerator producing both photon and electron beams. Linac's main component consist of the gantry, gantry stand and support, modulator cabinet, patient support assembly, and control console. As seen in figure 1.2.a, the principle behind linac is that electrons are accelerated from an electron gun toward a high-density target by a radiofrequency power generator. The acceleration happens in the so-called accelerating waveguide, located in the gantry head or the stand based on the design version. The accelerated electrons then are guided to the treatment head with the help of bending magnets, where it hits a target and creates photons in the Mega voltage

(MV) range, also called bremsstrahlung. The resulting photon beam is then modulated by collimators and filters and directed at the isocentre. Linac rotate at the isocenter point; in fact, this is the origin of a coordinate system, where all linac motion is referred to. The Elekta Synergy system shown in figure 1.2.b is an example of a linac with a gantry-mounted kV imaging system used for the treatments investigated in this study.

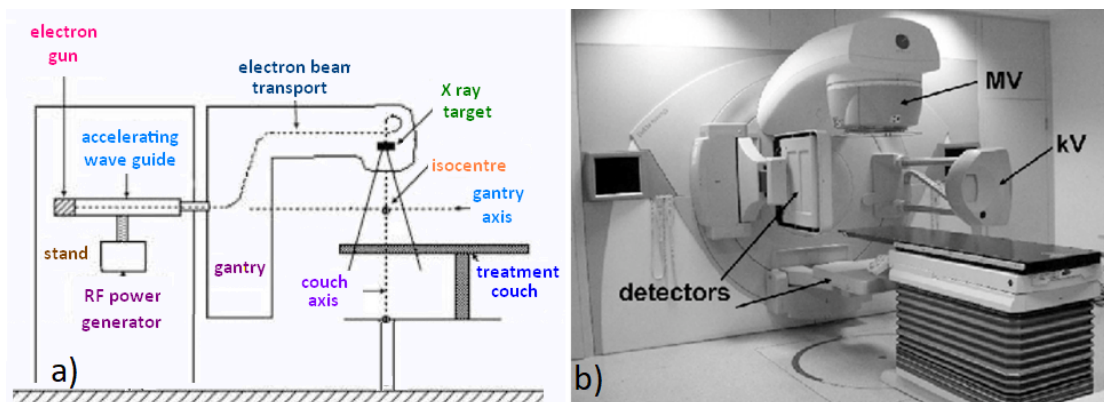


Figure 1.2: a) LINAC component b) Elekta Synergy with a foldout MV-detector (iViewGT) and a kV-CBCT system (XVI). (Figures from [56])

1.1.1 Clinical Workflow in EBRT

Successful radiotherapy means treatment optimization so that more healthy tissue gets spared and the prescribed dose is delivered solely to the malignant tissue. The treatment workflow starts with patient positioning and immobilization, followed by scanning with one or multi-modalities imaging system. Then shape and location of the tumor and organs at risk are delineated and delivered to the treatment planning system. The treatment plan goes through some verification and pre-treatment imaging before the dose is delivered. The process of obtaining high-precision radiotherapy is shown in consecutive blocks in figure 1.4. [5]

The first step is the acquisition of the anatomical images of the patient with the immobilization techniques for delineation of the targeted volume. Immobilizing devices immobilize the patient during treatment and with applied markers or tattoos provide a reliable means of reproducing the patient's position in each step. Therefore, in EBRT clinical practice, a planning computed tomography (CT) is taken with the so-called CT simulator before the treatment starts. A CT simulator is a diagnostic x-ray machine mounted on a rotating gantry that provides geometries identical to those found on linacs. As a result, the achieved CT scan is with the patient at the treatment position. CT simulator has excellent soft-tissue contrast allowing for improved tumor localization and

definition. Other image modalities could help for achieving a better target delineation. These additional images are then fused with planning CT and used for dose calculation. Lecchi et al. [38] provide a list of the advantages and disadvantages of CT, MRI, and PET for the planning stage. Virtual simulation is another advantage of the CT simulator, which enables rendering synthetic radiographs of the patient for arbitrary geometries. These digitally reconstructed radiographs (DRRs) can later be compared with EPID or other images to verify patient setup and beam arrangement. [42]

After the planning CT acquisition, a medical doctor goes through a delineation process on the Treatment Planning System (TPS). These delineated targets could also directly be projected onto the DRRs. To take organ motions and patient displacements into account, more margins are added to the tumor volume, and hence more healthy tissue is inevitably irradiated. These additional margins are introduced later. The TPS creates the DICOM RT file, where the coordinates of the contour points are stored. DICOM stands for Digital Imaging and Communications in Medicine. All current digital image acquisition devices produce DICOM images and communicate through DICOM networks. The flow of information from different modalities and manufacturers at each stage of radiotherapy is done through the DICOM network, as shown in figure 1.3. Data - patients, studies, medical devices, and so on - are viewed by DICOM as objects with respective properties or attributes such as the patient's name, ID, the date the image was taken, and the pixel image information. In tomographic imaging, each slice of the volume is stored on one DICOM file and the whole volume is stored in numerated consecutive DICOM files. Segmentation of the tomographic images results in a set of structures, defined by the DICOM RT structure set object. [45]

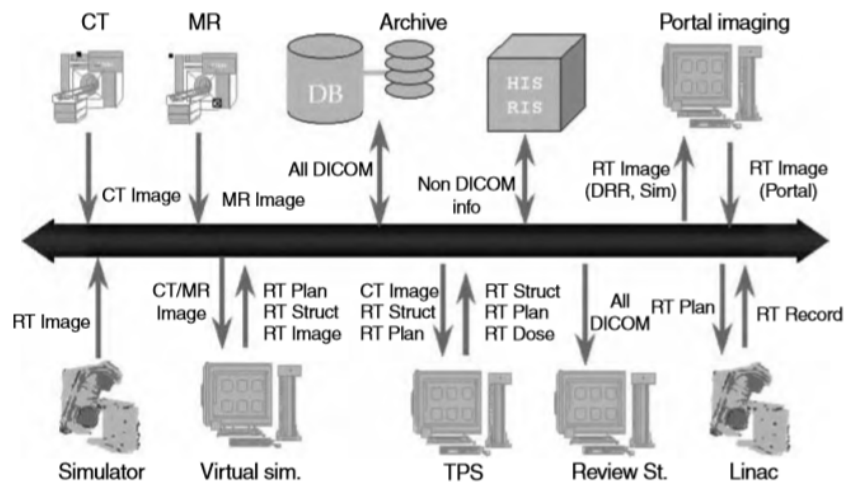


Figure 1.3: Diagram showing the transfer of DICOM data at different stages of the treatment planning and delivery process. (Figure from [42])

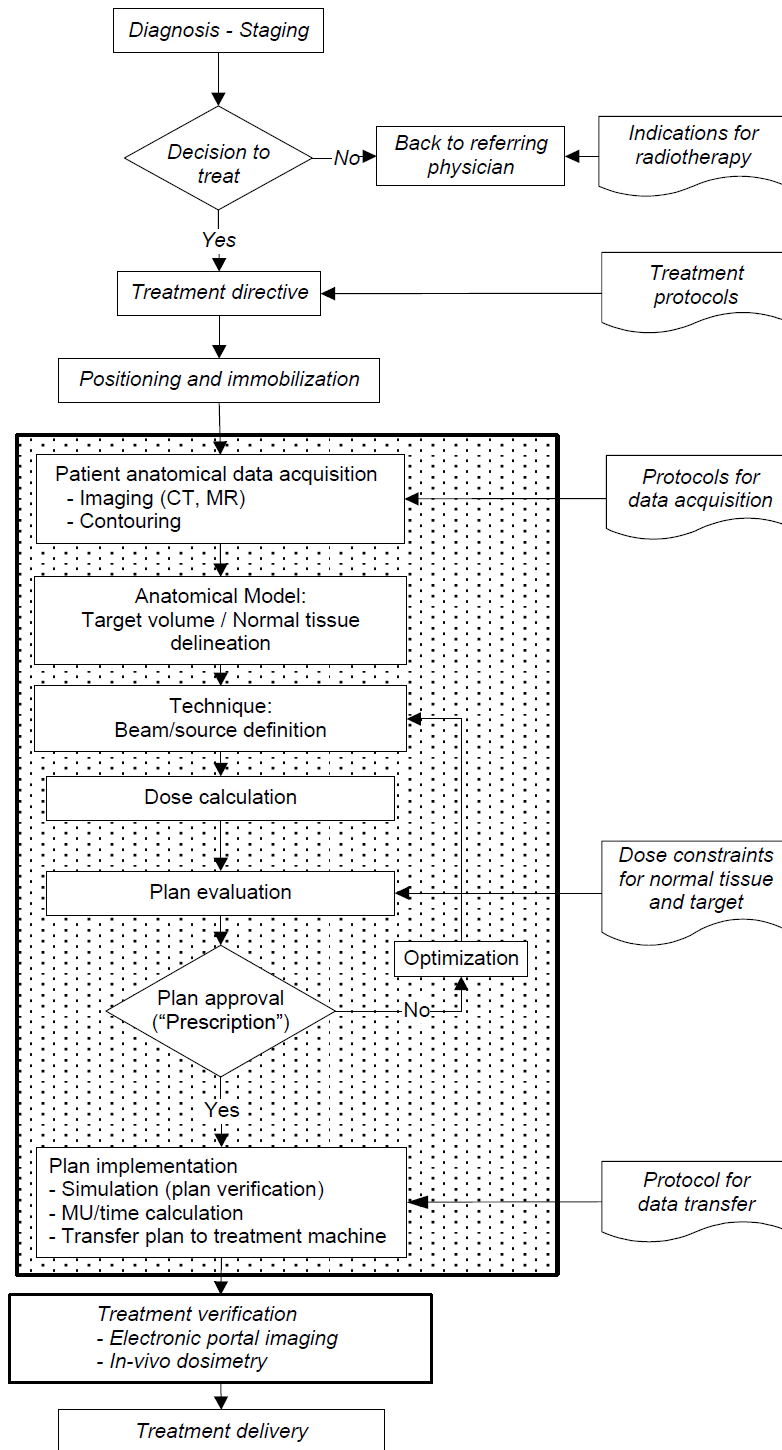


Figure 1.4: The chart shows steps involved in the clinical workflow of EBRT. The treatment planning process is in the shaded background and international protocols for each step are shown on the right side.(Figure from [5])

Treatment planning systems are essential tools in radiotherapy, consisting of software packages for computation and planning of the treatment delivery. All the information about the patient acquired during the treatment planning process, such as anatomical data, isodose lines, beam configuration, patient personal data, is stored in the TPS. Once the structures are defined, the selection of an appropriate method for planning an individual treatment is based on, on-site availability, tumor size, shape, and position. The delivered dose to the delineated structures is calculated by a dose calculation algorithm in two different ways: inversely or forwardly. In forward planning, the planner places beams into a radiotherapy treatment planning system that can deliver sufficient radiation to a tumor dependent on tumor locations, organs at risk, and other medical considerations. In the next step, the software calculates parameters for the treatment, including collimations and field sizes. This simulation and calculation in TPS generate a radiation dose distribution around the target volume and organs at risk. On the other hand, in inverse planning, the planner gives target doses and constraints for each delineation, and it is up to the optimizer to find the best treatment plan according to the inserted criteria. In other words, inverse planning starts with desired dose distribution to derive the beam parameters instead of the trial and error process of the forward planning, which starts with beam parameters.

In order to improve dose distribution characteristics, the treatment beam can get modified by collimators; the most widely used are multi-leaf collimator (MLC) located on the gantry. To match the target shape and depth, the beam coming out of the linac is shaped by the means of MLC. The advantage of using MLCs in shaping fields is that no manual intervention is necessary to change the shape of the fields. The treatment planning system generates the field shape according to MLC location then the appropriate settings are delivered to the linear accelerator for beam delivery. [51]

To evaluate the dose-calculation-plan multiple tools are available. Isodose curves, orthogonal planes and isodose surfaces, dose distribution statistics, differential dose volume histogram (DVH) and cumulative dose volume histogram are all tools for evaluating the planned dose distribution. DVHs are a quantitative evaluation of treatment plans as it represents a frequency distribution of dose values within a defined volume such as the tumor. It is a dose-to-the-organ representation, which shows the dose value (x-axes) delivered to a given amount of volume (on the y-axes) for a specific organ or target. If dose uniformity within the target volume is not achieved, then beam arrangement might need readjustment, and dose calculation needs to be repeated.

In conventional radiotherapy, photons are focused on the malignant cells for a predefined time to deliver a prescribed dose in a predefined number of fractions. As mentioned earlier, while achieving the therapeutic advantage, the dose to the surrounding healthy tissues should be kept as low as possible. In fractionated therapy a higher cell survival rate of the healthy tissues is obtained compared to the cancerous cells.[31] Also, repair mechanisms of tumor cells are generally less efficient between fractions. Additionally, tumor cells exhibit periodically changing radioresistance. By fractionation, radio-resistant

cells in one treatment may become more sensitive to irradiation in subsequent sessions. It is also possible to deliver the dose differently compared to the standard fractionation schemes. *Hypo-fractionation* consists of higher dose delivery in fewer fractions, while *Hyper-fractionation* refers to smaller dose delivery per treatment in more numbers of fractions.

Before delivering the radiation, the matching of the planning and treatment isocenter needs to be verified. This matching verification requires comparing simulation scans with DRRs from TPS and portal images from the linac. Portal images are presented later in this chapter. Once the tumor is correctly positioned on the treatment table of the linac, the gantry rotates around the patient, applying the dose from different angles. During treatment, due to patient's motions, and throughout treatment, which often takes several weeks, the tumors may also change in size and position. All the anatomic changes lead to variations in the planned dose distribution. Therefore tracking the patient anatomy by imaging modalities during or before each treatment fraction is necessary to evaluate the total delivered dose at each fraction, and make the necessary corrections. Lung cancer is distinctly affected by this problem because of the breathing motion. Different techniques to overcome organ motion in lung cancer treatments are introduced later in this chapter. Finally, those modalities used in the diagnosis can also be used for response assessment.

1.1.2 Treatment Techniques in EBRT

External Beam Radiotherapy has improved over time in the direction of achieving higher conformity. EBRT with photons is performed using many different techniques, briefly presented here:

- **Conventional radiotherapy (2D CRT)**
Targets are delineated on orthogonal films or few CT projections. Only a few roughly shaped field (typically simple square or rectangular) and broad margins are used for setup. This low conformity results in a high dose volume of the field which also encompasses healthy tissue near the tumor.
- **Three-dimensional Conformal Radiotherapy (3D CRT)**
Using newer three-dimensional (3D) imaging modalities, immobilization devices, and MLCs made it possible to overcome the limitation of 2D RT. Involving the geometrical shape of the tumor with better delineation of volumes of interest results in better conformality.
- **Stereotactic radiotherapy (SRT)**
Stereotactic irradiation focuses on precise dose delivery with sub-millimeter accuracy. Fewer dose fractionation with high doses or even delivering total dose in a single fraction, in the case of stereotactic radiosurgery, leads to reduced toxicity in tissues. Special frames are used in an invasive or non-invasive approach, in high precision delivery, to provide positioning and immobilization of the patient. Frameless

treatment take advantage of image-guided technology to achieve the same result. Its main application is the treatment of brain tumors as well as NSCLC.

- **Intensity Modulated Radiotherapy (IMRT)**

IMRT combines two advanced concepts to deliver 3D conformal radiation therapy; these include inverse planning and intensity modulation of the radiation beam during treatment. The incident fluence could vary across the field for different beams or even across the tumor for a specific beam. Offering concavities in treatment volumes, contrary to 3D CRT that only provides convexity treatment volumes, leads to better organ at risk (OAR) sparing. Prostate cancer serves as a valid example as it has a concave shape with bladder and rectum in proximity.

- **Volumetric Modulated Arc Therapy (VMAT)**

It is similar to IMRT but is more time-saving as the gantry is rotating during the whole irradiation phase following an arc. The optimization algorithm provides the possibility to continuously change the position of the MLCs to shape each subfield beam, the dose rate, and the rotation speed of the gantry.

- **Image-guided radiotherapy (IGRT)**

In a modern clinical setting, radiotherapy is inevitably an image-guided intervention, and imaging is involved in every step from diagnosis, simulation, treatment planning, verification, and radiation delivery and evaluation of delivered treatment with the help of follow-up images. However, the term IGRT as used now implies the use of a 3D imaging system on the treatment machine to correct patient positioning inter as well as intra-fractionally.[42]

- **Adaptive Radiotherapy (ART)**

The idea of Adaptive Radiotherapy is based on imaging information offered by IGRT to adjust or optimize the treatment during its process. The observation and modeling of setup uncertainties, organ and target motion, and changes in tumor physiology could signify that a treatment plan modification is necessary. Such modifications result in a heavier workload for the staff.

1.1.3 Image Guidance Technologies

Generally, the image-guided system must meet certain requirements; such as integration in treatment machine, minimally invasive, fast enough to follow time scale of patient changes while not prolonging the treatment, geometric precision, and providing good soft-tissue contrast while causing low risk and dose to the patient.[26] A detailed description of the IGRT procedure along the methodology and associated tools is found in *Accuracy Requirements and Uncertainties in Radiotherapy*. [5].The developed technologies for tumor motion monitoring could be radiation or non-radiation based. Especially in the case of non-radiation-based techniques, requiring an image is not a necessity. However, the radiation-based systems could be further categorized based on their beam quality, collimation, or dimension. Each of these tools or techniques has particular advantages

and disadvantages, and not all of them are practiced clinically. A short introduction of available techniques based on Goyal and Kataria [25], Birkfellner [6], AAPM Task Group [27], Herman et al. [30] is presented here:

1. Non-radiation Based Systems

- **Ultrasound-Based Systems**

Ultrasound could help with inter-fraction corrections as a means for cross-modality or intra-modality verification. In cross-modality, the ultrasound system as a pre-treatment modality is compared with the planning CT. While in intra-modality verification, ultrasound is involved in the planning process and acquiring the planning volume with the CT modality. Geometric accuracy is 3–5 mm, and typical applications include pelvic, upper abdomen and, breast radiotherapy. The use of ultrasound in prostate cancer has dropped significantly with the introduction of fiducial markers and 3D modalities. Despite being an inexpensive, non-invasive real-time technique with no radiation involvement, it suffers from different limitations. For instance, ultrasound is not suitable for a deeper target. Also, the pressure from the transducer could lead to a change of position and shape in the target organ. The training phase as well as a subjective assessment of the images are among other limiting factors.

- **Camera-Based or Optical Tracking Systems**

Using external surrogates with an established relationship with the internal target or mounted markers on the chest, for respiratory motion tracking is a common practice, with an accuracy in the range of 0.3 mm. However, the line-of-sight of the camera should always remain free to be able to follow the markers.

- **Electromagnetic Tracking Systems**

Using electromagnetic waves instead of ionizing radiation is an alternative for target tracking during or prior to treatment. These systems use wired or wireless transponders -also called beacons- embedded within the target of interest, and based on their emitted electromagnetic signal, a detector array in their proximity could pick up their location. In particular models, infra-red cameras then locate these detector arrays relative to the room isocenter. Different transponders are available such as permanent transponders for prostate cancer, anchored lung transponders, and surface transponders on the chest wall. This technique could provide real-time intra-fractional motion monitoring with geometric accuracy of <2 mm. Presence of any conductive or ferromagnetic materials could interfere with the emitted signal, and MRI can not be the follow-up imaging modality in the case of permanent transponders. Also, implantation and size of the transponders make it unsuitable for some anatomical sites.

- **MRI-Guided IGRT**

Real-time assessment of internal soft tissue anatomy and motion using soft

tissue imaging with MRI allows for intra-fractional corrections. The geometric accuracy of the system is 1-2 mm with a wide application potential such as prostate, liver, and brain, as well as for brachytherapy.

2. Radiation-Based Systems

Some examples of the mentioned systems are presented in figure 1.5.

- **In-room Planar X-ray based IGRT**

Gantry-mounted 2D imaging: Different systems may use either KV or MV X-rays for portal imaging to verify that the planned irradiation area matches with the area actually treated on the patient. Portal images are compared to reference images, which are often DRRs developed from the planning CT data set. The matching is based on bony surrogates or fiducial implants. Nowadays, this is achieved digitally with the help of Electronic Portal Imaging Devices (EPID). EPIDS have different detection systems such as video camera-based, liquid ionization chamber-based, and amorphous silicon-based with the latter one as standard EPID. In modern EPID, Si-based flat-panel detector is mounted on retractable arms, opposite to the high-energy treatment beam. Higher doses and lack of soft-tissue contrast compared to KV images are the main limitations of the EPID system. However, in MV images, distortion from metallic implants is less, and there is less need for calibration, as treatment beam and imaging beam are the same. Also, EPID is used for dose verification. When using orthogonal image pair of kV and MV, translational changes in all axes could be determined. Planar images are used for verification of the patient setup, assessment of target, and organ motion for corrections just before the treatment is delivered. On the other hand, intra-fraction motion tracking, as well as soft-tissue contrast, are not addressed by these gantry-mounted systems.

Floor-ceiling mounted 2D Imaging: These systems take advantage of a pair of KV source plus Imager mounted in ceiling and floor orthogonally so that the imaging plane intersects at isocenters. Moreover, a robotic couch helps with rotational corrections. Imaging happens at a lower dose, faster rate, and independent of gantry movement. The main applications of such systems are in hypofractionated treatments as well as respiratory motion tracking using external surrogates coupled with other motion detection systems such as optical tracking. Exactrac, Cyberknife are examples of such hybrid systems combining both ceiling/floor-mounted and gantry-mounted systems to offer real-time motion detection.

- **In-room CT based IGRT**

Kilovoltage CT: These systems have a kilovoltage X-ray source, which provides volumetric information with the advantage of better soft-tissue con-

trast. This lead to obtaining the setup information, and the anatomical changes without the help of surrogates or bony structure. The main application is determining pre-treatment inter-fraction uncertainty. The x-ray source could either be in a separate diagnostic CT connected to the treatment unit with rails, called kV CT on a rail or a cone-beam source mounted on the treatment unit, also used for planar KV images. The difference between these two approaches is the fan and cone-shaped beam, and the use of bow tie filter in the kV CBCT setting to improve the image quality plus reducing imaging dose to the skin. Varian OBI and Elekta XVI are examples of such CBCT systems. Longer scanning time, artifacts, and lower image quality in comparison with diagnostic CT is the main limitation of these technologies.

Megavoltage CT: The same beamline used for treatment is for imaging in Mega voltage CT. Despite the poor image quality in distinction to KV CT, fewer metal artifacts are visible. Moreover, considering dose recalculation is easier, MV CT is commonly preferred for adaptive planning. Depending on the beam configuration different systems are available. Tomotherapy has fan-beam and an arc detector and uses a lower energy beam for imaging while Siemens Artiste offers a cone-beam MV CT with a flat panel detector and the same beam energy but with lower linac output to minimize imaging dose.

Additional Imaging Dose

Different dose contributors exist in the process of treatment that is not easy to account for, such as linac leakage and scatter dose. Imaging dose in IGRT is another omni-directional contributor, counter to the treatment beam dose distribution. The improved accuracy in patient positioning plus margin reduction by using more and more image modalities results in additional dose burden, which eventually could lead to risk for secondary cancer induction. Considering the vast number of commercially available systems, the added dose from IGRT procedures has been investigated in many studies for different phantoms and anatomical sites.[9, 28] It is shown that throughout the treatment procedure, in some cases, the accumulative dose could exceed the reported threshold for secondary malignancy occurrence. Stock et al. [53] compared additional dose from IGRT using ExacTrac and anthropomorphic phantom for four different imaging modalities. The result suggested that the maximum additional imaging dose contribution to the treatment dose would be 1.7% for planar MV imaging, 2.8% for CBCT based, 0.2% for kV planar based and 2.9% for an adaptive radiotherapy (ART) setting employing CBCT, showing kV imaging delivers doses smaller than MV or CBCT based methods. AAPM Task Group 75 provides a summary of the approximate dose delivered by each modality as a function of patient characteristics and treatment site.[43]

Cone-beam CT, particularly MV IGRT, requires more attention as it could lead to higher doses that in specific treatment could exceed the deterministic limits. Pediatric treatments, patients with implanted devices, larger field of view applications, or in cases

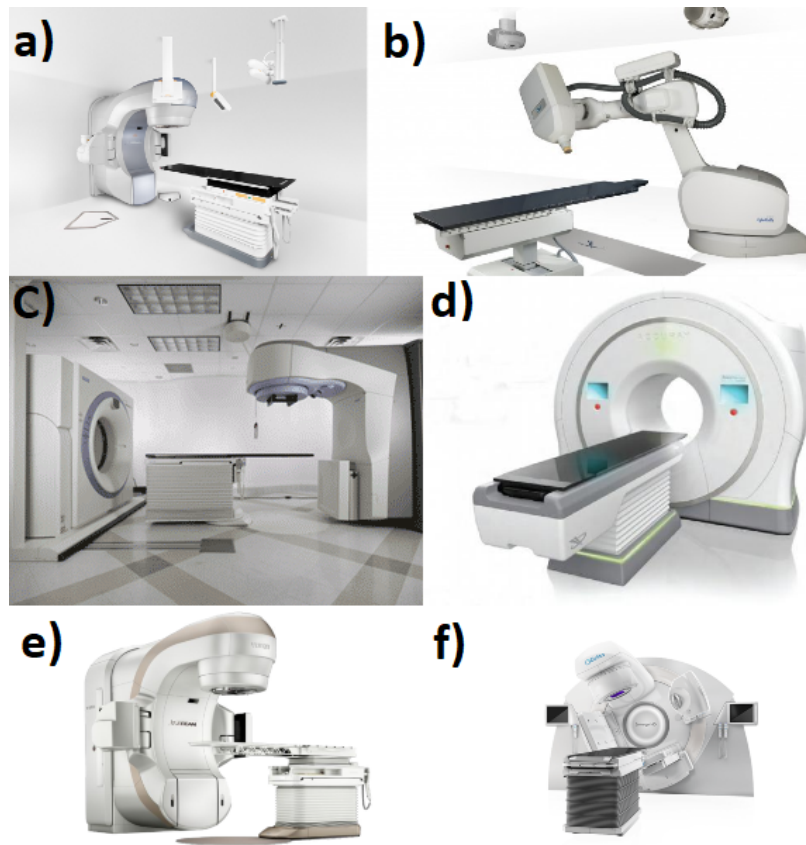


Figure 1.5: Commercial radiation-based IGRT systems:
Floor-ceiling mounted 2D Imaging : (a) ExacTrac, (b) Cyberknife,
Fan beam CT: (c) Siemens KV CT, (d) Accuracy Tomotherapy MV CT,
kV CBCT : (e) Varian Truebeam, (f) Elekta Synergy.

where the treatment doses already reaching the limits for OAR require more careful consideration. Also, whenever it is feasible, the imaging dose needs to be included in TPS. However, this is not easy in KV CBCT as the TPS can not easily incorporate the dose in the kV range. Using a narrow field of view, plus an efficient imaging mode aims to reduce the imaging dose. Newer low KV modes are under development; that said, it depends on image receptor sensitivity, acquisition modes, and imaged anatomy. In general, the ALARA convention, As Low As Readily Achievable, is as well applied to additional doses from imaging modalities. In special cases, exceeding deterministic limits, based on the risk-benefit counterbalance the oncologist should make the final decision on using IGRT.

1.2 Uncertainty in Radiotherapy

The error refers to any mismatch between the actual anatomy, planned, and the treated area. This section provides an overview of typical occurring errors. Errors could be classified based on their source, time, and pattern of occurrence. Thus their minimization, as well as corrections, need a different strategy accordingly.

Errors based on the source of origin

Errors could happen in any step of the RT chain, from imaging to treatment delivery. Wrong choice of imaging modality, distortions, or image fusion when using multiple imaging modalities could be the sources of errors in imaging. The delineation process itself is highly error-prone because of the inter and intra-observer variations. Inaccurate target delineation consequently results in systematic errors, and when not corrected, it is present in all fractions. Setup errors happen when positioning and immobilization of the patient are in place. Technical or quality assurance issues such as laser misalignment, isocenter misalignment, or couch sag are examples of this. Verification with 2D and 3D image modalities and comparison with planning CT or DRRs help detect and correct these scenarios. Organ motion and physiological changes within the course of treatment are among other sources of error. Any changes in position, size, and shape of the target could lead to different dose distributions. Response to a fractionated RT could lead to tumor shrinkage, weight loss, or resolving atelectasis in lung cancers (opening of blocked airways). In ??, the time-scale of examples of such physiological changes is shown. The changes happening up to minutes require motion management, while the longer ones demand imaging and setup correction, and in case of long-term changes over weeks, adaptive planning is required.

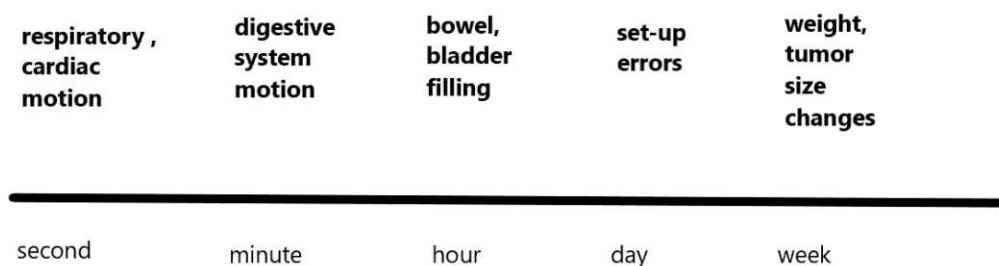


Figure 1.6: Examples of physiological changes during treatment

Errors based on the pattern of occurrence

The pattern of deviation needs to be known as these components are used in PTV margin calculation and delivered dose, which is described in detail when introducing

radiotherapy margins.

- **Random errors**

The direction and magnitude of deviation vary for each fraction. Random errors blur the cumulative dose distribution.

- **Systematic errors**

The direction and magnitude of deviation remain the same for each fraction. Systematic uncertainty results in a sharp shifted cumulative dose distribution which in turn results in persistent under dosage of same part of the target.

IGRT is a powerful tool to deal with inaccuracies. As shown in figure 1.7, daily position without image guidance shows a high systematic error (10 mm) and high random uncertainty. Using offline IGRT has reduced higher systematic errors without affecting the random errors, whereas random errors improved only with online correction strategies in place.[11]

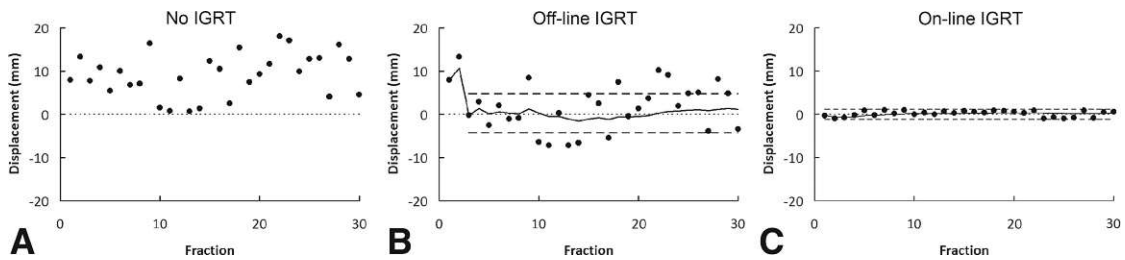


Figure 1.7: Circles show daily position, the solid line the mean, and dashed lines the control limits. a) The daily position without image guidance shows a large systematic and random errors, b) offline correction protocol controls systematic errors, and c) online correction protocols controls both the systematic and random errors. (Figure from[13])

Errors based on time of occurrence

Our ability to account for motion is dependent on how much reaction time is available. As a result, we have to differentiate between the displacement happening in-between the treatment sessions or during the treatment session.

- **Inter-Fraction Motion**

These errors occur in days between the fractions. Inter-fraction motion causes a shift of the dose distribution, and consequently, adaptive planning is required for the upcoming fraction. Such deviation are because of setup errors and anatomical and physiological changes. The correction strategies for the latter example focus on immobilization devices as well as proper patient preparation, namely, bladder filling protocols. However, setup errors are dealt with using PTV margin recipes and image guidance verification.

- **Intra-Fraction Motion**

The errors occur during the treatment delivery and cause the static dose distribution blurring over the motion path. Intra-fraction motion can be non-periodic (including patient movement and physiological changes such as swallowing motion) or periodic (including respiration, cardiac). Corrective strategies for periodic motion such as respiration is of high importance; especially for the treatment of lung and upper abdomen section. It needs to be real-time or implemented before the treatment delivery. Non-periodic motions get resolved with different motion management equipment such as endorectal balloons, abdominal compression since external immobilization is not a big help. Published motion study data, as well as individualized margins based on patient motion patterns, are integrated into the target volume, that is presented later.

Offline and Online Correction Strategies

When facing uncertainties, various correction strategies may be applied; from imaging, patient preparation, repositioning, to even replanning and changing of margins. Imaging plays a significant role in detecting and verifying uncertainties in different phases of treatment:

- **Offline verification**

Comparison of planning images with in-room imaging takes place after the treatment delivery. The calculated uncertainty derives from the analysis of multiple image-set from a few fractions, representing mainly the systematic errors. Then it is used for the correction of subsequent fractions.

- **Online verification**

The comparison of planning images with in-room imaging happens before the treatment delivery, and the changes are applied for the treatment of the same day. It is based on single images before each fraction, leading to the improvement of both systematic and random errors.

As it is shown in figure 1.8, with no protocol in place, the uncertainty is not addressed, and PTV does not fully cover the tumor in each fraction. Using offline protocols helps to calculate and apply systematic error. As a result, the new isocenter gets adjusted by the mean value and PTV covers the target. With online protocols in place, daily corrections could account for both random and systematic errors, and the target is brought within the PTV.

The shrinking action level protocol (SAL) and No action level (NAL) protocol are common offline strategies. The action level is the maximum permissible error. NAL steps in for correction after a few fractions; this requires less imaging, plus it is easier to perform. While SAL has a threshold value that shrinks for each fraction; with corrections happening only when this threshold exceeds. Online correction strategies employ the

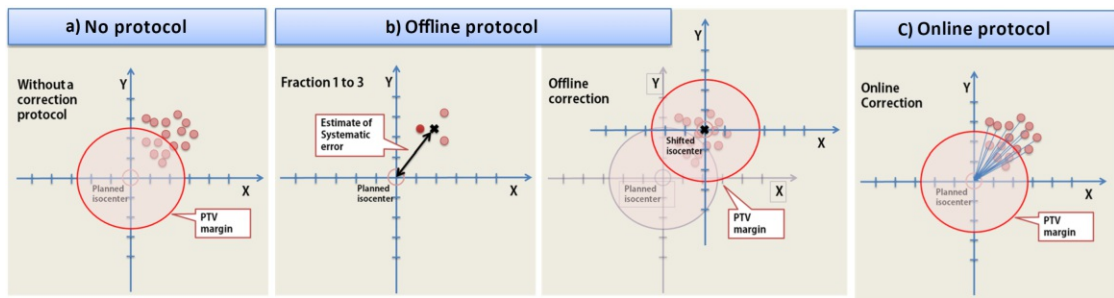


Figure 1.8: Representation of PTV margins when a) No correction strategy is applied b) Offline protocol c) Online protocol applied. (Figure from[1])

same concept of the action level. Daily imaging and error calculation is compared against an action level. In case of exceeding that level, corrections are made before the treatment on the same day. This correction certainly comes at the cost of more dose to the patient and more workload for the staff and thus preferred only for small PTVs in stereotactic treatments. Sites with harder immobilization practicability and more daily variation in the target motion benefit most from online procedures. When such correction is not feasible at all, larger PTVs are irradiated.

1.2.1 Radiography Margins

It is almost impossible to deliver the dose to the cancerous cells without irradiating the surrounding tissues; therefore, International Commission on Radiation Units and Measurements (ICRU) introduced various volumes and margin concepts for standardizing, describing, and analyzing the dose to the irradiated volumes, as found in figure 1.9. This standardization ensures that the objective of treatment is achieved even in the presence of discussed uncertainty. A detailed description of the volume and margin concepts are available in the ICRU Reports 50, 62, and 83 (1993, 1999, 2010). [36, 37, 4]

- **GTV**
Gross Tumor Volume is the palpable size of the malignant tumor obtained from a combination of imaging modalities. It may consist of primary tumors and metastases.
- **CTV**
Clinical Target Volume includes the GTV and surrounding tissue that contains the microscopic disease and other areas considered to be at risk, which require elimination. It is determined based on the pattern of invasion or spread.
- **ITV**
Internal Target Volume consists of CTV and an additional internal margin (IM) for variation in the size, shape, and position of CTV relative to a reference frame of the patient. Respiratory motion, rectum, or bladder filling are examples of

physiological changes causing these variations and examples of the sites that need such individualized target volume the most.

- **PTV**

Planning Target Volume is the most significant volume in radiation therapy. It is a geometrical concept that expands CTV by a margin containing both IM and setup margin (SM). SM margins account for day-to-day errors in beam alignment, delivery, and patient positioning inaccuracies; basically, everything that affects a fixed reference point in the target. PTV accounts for the net effect of all possible inaccuracies during planning and delivery so that CTV receives the prescribed dose. Hence, PTV is closely related to image guidance.

- **OAR**

The organ at risk is normal healthy tissue adjacent to PTV. The radiation for OAR needs to be minimized, so its radiation sensitivity influences the prescribed dose significantly.

- **PRV**

Planning Organ at risk Volume could be described as PTV for OAR, taking the setup and organ movement into account for the OAR instead of the tumor.

PTV calculation

Conformal radiotherapy techniques try to deliver high doses wrapped around the tumor or in other words, the PTV. PTV is used for planning and treatment delivery, consequently calculating correct PTV volume is crucial to ensure the delivered dose to CTV is as prescribed. Precise PTV calculation guarantees delivery of maximum dose to the tumor while sparing the OAR. PTV calculation is established based on the setup and organ motion uncertainties:

- **PTV margins for SM**

Calculations are from formulas, or so-called, margin recipes, derived from the calculation of systematic and random errors from a population of similar patients. Different recipes use different weights for combining systematic and random errors. A simplified known margin recipe is the following formula[55]

$$PTV = 2.5\Sigma + 0.7\sigma \quad (1.1)$$

with Σ the quadratic sum of the standard deviation of all preparation systematic errors and σ quadratic sum of SD of all execution (random) errors. Greater weight is given to systematic error as it causes a persistent dose shift. This formula ensures CTV coverage for 90% of the patients with 95% isodose.

- **PTV margins for IM**

Dealing with predictable patient motion during treatment based on available motion studies leads to a rough estimation. These population-based margins are based

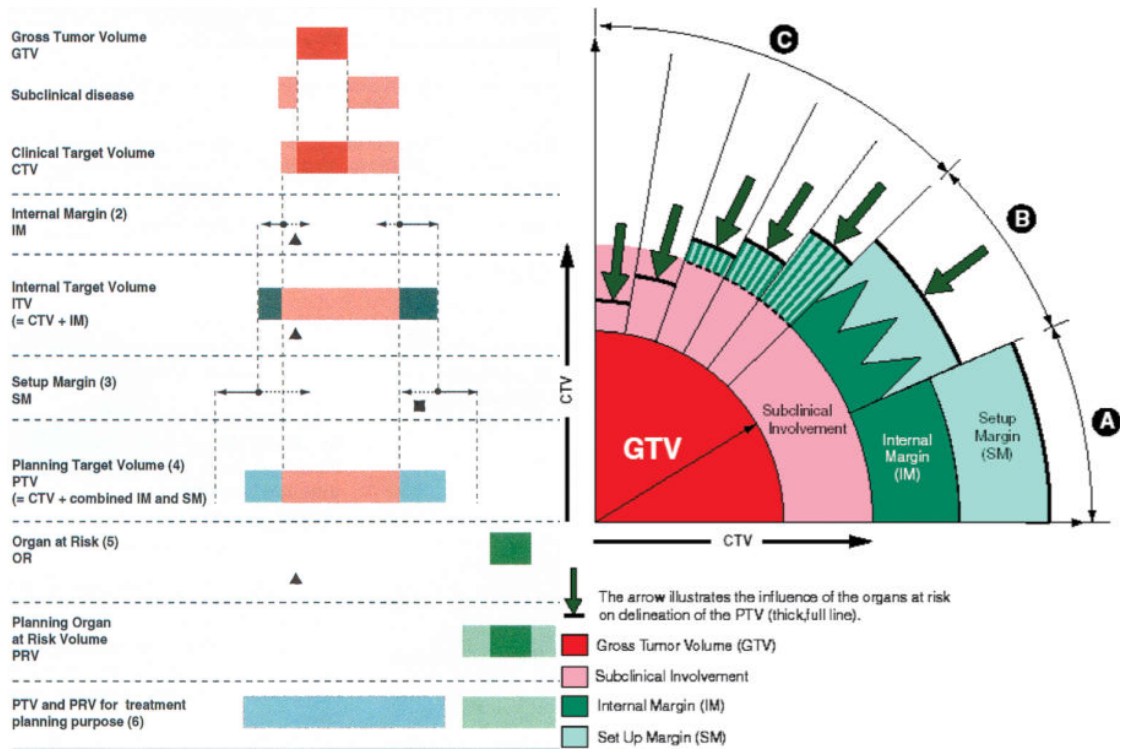


Figure 1.9: Graphical representation of the volumes of interest, as defined in ICRU Reports No. 50 and No. 62. (Figure from[37])

on extremes of reported motion, thus, not a proper individual representation. Obtaining individualized target volume, introduced as ITV by assessing its motion, with the help of imaging is a better solution. For obtaining ITV, an overlapping volume from fusing scans of extreme motion or positions is generated. Extreme motion, such as maximum inspiration and maximum expiration in a breath-hold technique, or extreme positions, such as the empty or full bladder. However, this leads to overestimation and larger ITV while not even capturing the whole trajectory. 4D CT scan or maximum intensity projection are other alternatives for lung cancer cases. In 4D CT, using delineation solves the problem of trajectories. On the other hand, for lung tumors, the maximum intensity projection (MIP) tool is like a shortcut feature for central tumors far from the mediastinum or chest wall, which creates an image by assigning the maximum brightness to every captured pixel during imaging and offers an accurate alternative to ITV. However, this is achieved only for central lung tumor cases. Accounting for anatomical changes happening over time in PTV is still not established, and requires adaptive RT.

1.2.2 Patient Positioning and Immobilization

With the current trend towards higher overall dose, higher dose per fraction, and smaller volumes, care and attention to patient preparation are of even greater significance. The patient position relative to the gantry (the treatment system) has to be the same as it was for the planning CT. In the fractionated therapy, in every fraction of the treatment, the very same position has to be reproduced. Lasers are in specific areas of the treatment room and simulation room for marking the isocenter of the treatment machine and ensuring straight patient position without any rotation. The treatment couch itself could be the source of uncertainty, and as a result, flexible inserts and foam mattresses should be avoided. The isocenter of the treatment relative to the isocenter of the linac and room has to be checked. The indicators of the crossing points are then checked through images to match the structure that should be centered. Then external markers or fixation devices are added to the patient for the later repositioning of the subject. Fixation devices allow the correct positioning of the different anatomical parts of the patient and the immobilization of the patient during the delivery of the radiation. Therefore, proper immobilization demands less frequent imaging. Inter-, as well as intra-fraction variations, are also reduced.

Immobilization should be easily reproducible, rigid for maximum stability, and at the same time, with least patient discomfort and causing least dose perturbation. Also, it could be internal such as endorectal balloon helping with dose reduction of the rectal wall in prostate cancer treatment. Adding more fixation devices does not necessarily lead to a better result, especially in the thorax, abdomen, and pelvis areas. It should be tested and verified for any benefit of use.^[1] Different fixation devices are needed, based on the treated site, the extent of the tumor, positioning, and other factors to ensure the position remained as similar as possible. Comparison of uncertainty from different immobilization devices, for various anatomical sites is found in *Accuracy Requirements and Uncertainties in Radiotherapy* [5]. Examples of such site-specific devices are listed here: [42]

- Simple sand/bolus bags for general support
- External arm supports, bodyboards, alpha cradle, and knee rest for breast and pelvis treatments
- Thermoplastic casts/polycarbonate mold for head and neck, and pelvic treatments
- Vacuum bags with reproducible arm position and abdominal compression (compression plate, bodyfix, pneumatic compression) to reduce diaphragmatic motion for breast, thorax, and upper abdomen treatments
- Thermochemical polystyrene devices (headrests and knee supports) for head and neck, and pelvic treatments
- Stereotactic frames for the brain and spine treatments

Daily patient setup verification is done differently depending on the treatment. External marks on patient skin or immobilization devices used as reference points. However, because the skin marks can fade or shift, it is not reliable in all cases. In head and neck treatment, the acquisition of positional information requires identifiable points like bony landmarks with accurate localization on multiple images. Those landmarks should be inside or close to the target volume. In many cases, such landmarks are not available, for example, in the treatment of prostate cancer. To create artificial landmarks, many radiotherapies procedures make use of implanted radio-opaque markers. The downside to this method is the lack of information about anatomical structures close to the target volume, which may include organs at risk. Also, it is an invasive intervention.

For greater accuracy, several fixed landmarks (anatomical or fiducial) are defined. These landmarks are easy to observe on images taken before each fraction. Fiducial Markers serve as surrogates to soft-tissue targets when they are hard to visualize, and their alignment cannot be related to bony anatomy. Because these fiducials can be tracked in real-time to obtain 3D coordinates of the target for subsequent corrections. These images are then compared with a reference image to enable the treatment position or beam parameters to be adjusted. The invasive methods like implanting fiducial markers or placing electromagnetic transponders in or close to the tumor have disadvantages and involve some difficulties, such as possible complications from the marker and transponders insertion. On the other hand, non-invasive methods can, for instance, work with surface markers and then try to calculate the tumor motion from surface or surrogate markers' motion using breathing motion models. However, they can also suffer from the inadequate correlation of organ movement or aperiodic motion. Another method is to track the motion only by real-time imaging and then using 2D-3D registration throughout the whole irradiation process. Intensity-based 2D-3D image registration is an attractive approach for target motion monitoring by the kV imaging equipment, which is available inside the treatment room without being dependent on implanted fiducial or external surrogates.

Unless imaging the entire treatment volume continuously, respiratory surrogates are used to infer tumor motion. Internal markers implanted in the tumor offer the most accurate information regarding target position during treatment; however, the benefits of accuracy need to be weighed against the cost and invasive procedure of implanting markers in tumors as well as against possible marker migration. When external markers used as a respiratory surrogate, their relationship with the internal target needs to be established; for example, by sampling the target position fluoroscopically for brief periods at several intervals.

IGRT and its methods and means allow to reduce the treatment margins and to escalate the dose delivered to the tumor. One aspect of IGRT is inter-fraction verification and alignment of the tumor position. A further application is the intra-fraction use of X-ray kV- or MV-imaging during treatment enabling adjustment of the beam to the tumor mo-

tion to take intra-fraction physiological organ motion into account. The goal of IGRT is to react even on movements because of the heartbeat or breathing. It is especially relevant when the affected tissue or organ is exposed to heavy motion, such as pulmonary tumors that can move up to several centimeters. The patient is moved based on the mismatch of the acquired images compared against the planning-CT image (reference image) so that the PTV is in the isocenter of the treatment beam. The delivery of the radiation field is moved in such a way to follow the PTV. For assessment, these images of the patient need to be acquired in situ and register to a 4D (or 3D) data set acquired during simulation. These real-time imaging methods are called *four-dimensional radiotherapy* (4D RT).

1.2.3 Respiratory Motion Management

Inner body motions such as respiration, heartbeat, swallowing, bowel movement could lead to the displacement of structures in the body. Among those, respiratory motion is an involuntary process coordinated by diaphragm movement and intercostal muscles. This movement could result in displacement of structures, including tumors, in the thorax, upper abdomen, and even pelvis area. Hence, respiratory motion management is a significant factor to account for in the treatment of lung tumors.

Rate and depth of respiration is versatile, and displacement could be patient-specific. Especially for the patient with lung cancer, different irregularities could be observed. Consequently, depending on the tumor location, tumor displacement could also show a different pattern of motion. Breathing pattern measurements distinguished in different postures, such as upright, prone, supine, lateral decubitus. Breathing type refers to the chest or abdomen involvement, with an increased circumference in those areas, and depth of respiration such as shallow, normal, deep, define the change in the lung volume. These are among other factors that need to be documented for the characterization of breathing patterns. Systematic changes could also lead to shifts in the respiratory baseline. Moreover, these patterns can vary in magnitude, period, and regularity during imaging, and treatment sessions and sometimes variations within and between respiratory cycles exist. Using methods like audio-visual feedback can improve respiration reproducibility. Different possible patient breathing patterns are illustrated in figure [1.10](#).

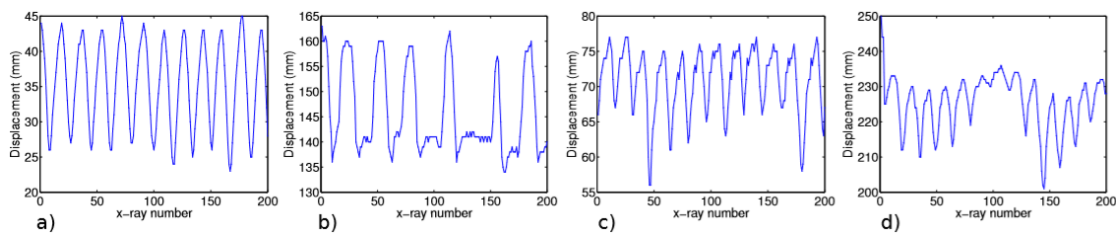


Figure 1.10: Examples of different breathing pattern: (a) smooth regular breathing, (b) irregularities where the patient held the breath, (c) significant changes in amplitude, and (d) changes in the baseline. (Figure from [22])

The extent of motion varies based on its location, relation to bone mediastinum and diaphragm, plus respiration type. On the other hand, the motion is present in all three axes but predominantly in the craniocaudal direction, up to several centimeters. Based on the summary of AAPM report 91 on Lung and tumor-motion data, the extent of motion varies from 1-4cm, and in the case of deep breathing could increase up to 8cm.[32]. Unfixed tumors in the lower lobes show more craniocaudal (CC) movement, while anterior tumors show greater anteroposterior movement.[34] Tumors fixed to the chest, and central tumors show less motion compared to unfixed peripheral tumors. The range of motion of tumors in a different part of the lung depicted in figure 1.11. Another phenomenon shown in figure 1.11 is that some motion happens elliptically, following a different path during inspiration and expiration. This phenomenon is called hysteresis and is present in almost 50% of the cases.

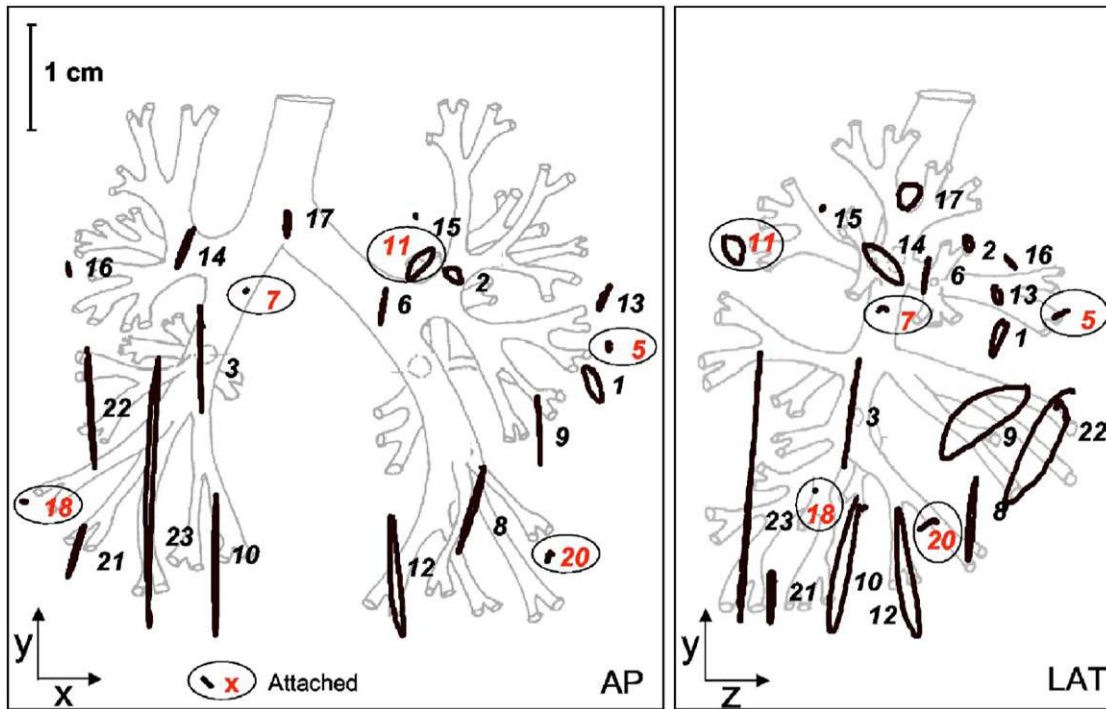


Figure 1.11: Twenty-one tumors and their trajectories in the coronal (right) and sagittal plane (left). The circled tumors are attached to the bony structures. (Figure from [48])

The respiratory pattern might change between the imaging and treatment planning stages. Delivery in the presence of such intra-fraction organ motion causes blurring of the static dose distribution over the motion path, and finally, a deviation between the intended and delivered dose distributions. It is necessary to identify the trajectory and range of motion with the help of imaging. At the same time, in the presence of such a motion during the imaging phase, planning CT will cause distortion and motion artifacts which could lead to inaccurate target delineation. The respiration phase, motion amplitude, plus CT features such as slice thickness and pitch could influence the motion artifact. The following imaging techniques are available, to include the entire range of tumor motion for respiration at the CT acquisition:

- **Slow CT scan:** Trajectories of motion during a respiration cycle covered in each couch position. Averaging the slices leads to loss of resolution and blurring, which could result in the wrong delineation.
- **Breath-hold scan:** Fusing scans from a particular phase of inspiration and expiration while the patient holds his breath creates ITV. It relies on the patient's ability to hold breath reproducibly.

- **4D CT:** Either images of the whole respiratory cycle or a particular part of the cycle are taken and later sorted based on their phase of respiration. An external signal such as reflective markers coupled with optical cameras used for determining the respiration phase. This recording establishes a correlation between tumor position and motion with external markers and surrounding organs. Breathing-training techniques are needed because 4D CT relies on breathing pattern. The inconvenience of 4D CT is the need for more delineation, longer scan time, and higher doses.

Imaging at treatment session helps to detect tumor positions directly or helps verify the relationship between respiration signals and tumor motion and therefore is needed. Another alternative is the use of spirometers and external markers to reduce the need for real-time visualization. The optical system, infrared-reflective markers, and belt with pressure sensors are some other methods of monitoring the respiratory signal. However, the detected motion is not always in a stationary correlation with tumor motion. Especially patients with chronic obstructive pulmonary disease have shown paradoxical movement. Therefore, this relationship should be established for each patient with the help of imaging and controlled to remain the same during treatment. Also, appropriate margin formalisms alongside the respiratory motion should be developed to calculate proper PTVs for the various respiratory motion management strategies. Patient-specific tumor-motion measurement should be included in the margin calculation and generation of ITV because without such motion management techniques, the whole range of motion is considered for defining the margins.

AAPM Task Group 76 (Keall et al. [32]) recommend using respiratory management techniques for motion ranges above 5-mm in any direction, although, in cases of significant healthy tissue sparing or specific procedures like stereotactic RT, this motion limit could be even lower. Managing intra-fraction motion results in smaller margins. As a result, reducing the volume of treatment helps sparing OAR and healthy tissue. Several techniques are available to achieve this by management of intra-fraction motions:

- **Motion restriction Methods**

Applying compression techniques (mechanical or pneumatic) on the upper abdominal wall reduces the range of motion, especially the diaphragm motion. Abdominal compression is also used with a stereotactic body frame to limit diaphragm motion and force shallow breathing. The forced Shallow-Breathing method uses abdomen pressure to such an extent that only normal breathing is allowed. Obese patients, as well as plate position reproducibility are the challenges of this method.

- **Breath-Hold Techniques**

Breath-hold helps to deliver the beam at a particular part of the respiration cycle. Consequently resulting in smaller margins, and tumor motion reduction. Different breath-hold techniques exist, which could be voluntary or assisted, to maintain a static lung volume and tumor position. Also, it could be with or without a

respiratory monitoring system; the latter heavily depends on patient breath-hold ability. Audio-visual coaching, as well as proper training of the patient could help to achieve better results. Most reproducible positions are at deep inhale or deep exhale. Also, the potential dosimetric advantages of increasing the lung volume result in using deep inhale as the preferred point for breath-hold. If the breath is held at the end of inspiration, it is referred to as the deep inspiration breath-hold technique (DIBH). DIBH ensures reduced tumor motion and internal anatomy in a way that often protects critical normal tissues. Active breathing control is an assisted method using a spirometer to suspend the airflow at a predefined phase and volume, which is commonly 75% of maximum inspiratory capacity. The method selection is dependent on careful selection and the ability of the patient to reproduce the cycle.

- **Respiratory Gated Techniques**

The respiratory gating technique focuses on a particular section of the breathing cycle (or gate) for imaging and treatment delivery when the target volume is within a preset tolerance around its planned position. The scan could be triggered, based on the phase or amplitude of the respiratory motion. Phase-based gating could be prospective or retrospective. In prospective gating, solely the scans of the preset phase window are obtained. While in retrospective gating, the whole cycle is recorded and sorted later. For respiratory monitoring, various companies offer solutions with an external respiration signal using infrared reflective markers on the patient's body surface or acquiring x-ray projection images to determine internal anatomy positions. Other techniques to record and gate respiratory movements are a belt around the body and 3D video surveillance of the patient's surface. External breathing signal such as in real-time position management system (RPM) using a reflective marker box on the chest or internal fiducial markers such as in real-time radiotherapy system (RTRT) using gold markers and floor/ceiling mounted fluoroscopic camera used for reading breathing signal and coordinating the beam-on and off time. This reduces margin to a great extent but at the cost of more frequent imaging and longer treatment time. Another challenge is the surrogates are not always a true representative of the tumor motion.









- **Real-Time Tumor-Tracking Methods**

Tracking refers to the real-time measurement of six degrees of freedom of several rigid bodies. In tracking methods, the motion is followed instead of being frozen at a specific phase. First, the tumor position needs to be known. And this is achieved by fluoroscopic images acquired during treatment or by tracking the implanted fiducial markers or monitoring the patient's surface, which correlates with the tumor motion. When the tumor position is known, the delay between tumor motion detection and beam adaptation needs to be minimized, meaning less than half a second. Subsequent tumor motion should be predicted from the patient respiratory signal to reduce the lag between tumor motion and linac response. This prediction method is applied for both tracking and gating methods. As a result, one needs

to be aware of the breathing phase because, as mentioned earlier, that inspiration and expiration could follow different trajectories due to hysteresis. Another way is to use optical tracking of chest wall motion with periodic imaging verification as imaging itself could increase the lag. The beam position is adapted to track the tumor by adjustment of MLCs or moving the linac head/arm or even the treatment couch. Shorter treatment time in comparison with gating and higher imaging dose are features of the tracking method.

An overview of respiratory status, the timing of beam-on, time-efficiency, and general size of the internal margin according to the presented methods is shown in table 1.1. It shows that tracking, as well as breath-hold, is more successful in terms of reducing the margins. Also, it is important to note, gating and tracking systems involve more quality assurance checks.

Table 1.1: Comparison of different methods of respiratory motion control. Red is used to show when the beam is on. (Table from[3])

Method of RMC	Respiratory status	Timing of beam-on	Time-efficiency	Internal margin
Suppress			good	large
Breath-hold			bad	small
Gating			bad	medium
Tracking			good	small

1.3 Motivation: Lung Cancer IGRT

Lung cancer is one of the leading cancer type worldwide and the most common cause of cancer death, particularly amongst men, with less than 15% five-year relative survival rate. Cigarette smoking is by far the most important risk factor. [52] Lung cancer is defined histologically in four main groups; squamous cell carcinoma, adenocarcinoma, large cell carcinoma, and small cell carcinoma. The first three are classified as non-small cell lung cancer, accounting for about 85% of lung cancers. It is necessary to differentiate between small cell lung cancer (SCLC) and non-small cell lung cancer (NSCLC) because each needs a different treatment and prognosis corresponding to its biological behavior.[29] Treatment for lung cancer is often multi-modal and, it depends on whether the tumor is a small cell or non-small cell, as well as the stage and molecular characteristics of cancer. Lung cancer staging assesses the extent to which a lung cancer has

spread from its initial source following the internationally used TNM system. A detailed description of the stage classification can be found in the Detterbeck et al. [15].

The most common treatment options consist of local treatment such as surgery and radiotherapy and systemic treatment such as chemotherapy and targeted therapies. Other developments in treating lung cancer are immunotherapy, gene therapy, thermal ablation. Radiotherapy and chemotherapy are often used in combination (radio-chemotherapy) or with surgery. The treatment sequencing is called *neoadjuvant* (administration of therapeutic agents before a main treatment), *concomitant* (treatment that is given together with the main treatment), and *adjuvant* (treatment that is given after the primary, main or initial treatment). Radiotherapy is an active part of the mentioned treatment sequences. For early-stage thoracic cancer SBRT is the main choice of treatment, whereas for advanced ones, conventionally fractionated radiotherapy is preferred. The standard and emerging treatments for each stage can be found in Lemjabbar-Alaoui et al. [39]. In thoracic radiotherapy, the uncertainties could arise from incorrect target definition, internal motion such as cardiac and gastrointestinal motion but most importantly respiratory motion, setup error, and finally errors result of changing anatomy. PET-CT planning could help to overcome CT scan limitation to achieve better target definition as it can differentiate unaffected nodes as well as tumors from collapses, however, incorporating motion management in PET-CT is not feasible.

Respiratory motion is the main contributor to the uncertainties in the treatment of lung tumors. These intra-fraction tumor motions can cause tumor displacement of up to 5cm. As a result, knowing the tumor motion's behavior relative to respiration is important. Lung tumors have shown higher craniocaudal (CC) motion. Also, the motion amplitude varies based on the tumor location; with central tumors, tumors attached to the chest wall, and superior tumor showing less motion in distinction to peripheral tumors in the lower lobe and anterior tumors. Another point in figure 1.11 signifies that inspiration and expiration trajectories differ, which is referred to as hysteresis. Another factor shown in figure 1.10, which must be considered is that the breathing motion pattern is not the same in different individuals.

The continuous tumor and diaphragm movement, in free fast breathing conditions, next to CT movement lead to motion artifacts in planning CT, distorted tumor shape and size definition. As described earlier, using slow mode scan, breath-hold techniques or respiration correlated CT reduce motion artifacts on the CT, provide a better assessment of the individual respiratory motion. Due to considerable variation between patient and tumor motion residing in different parts of the lung, ITV should be derived from individual information instead of population-based data. Deriving individualized ITV margins either by MIP or combining respiratory-correlated scans or breath-hold scans is needed to derive more accurate PTV margins.

Thoracic treatments could benefit from some of the introduced motion management strategies to avoid large PTV margins. In free-breathing techniques, the treatment delivery is throughout the breathing cycle with a large PTV margin or during a specific window of the breathing cycle, monitored by an external signal. Using gating techniques with some pre-treatment inter-fraction verification is widely practiced in lung cancers. Using reduced PTV margins combined with tumor tracking during the entire breathing cycle is another approach mainly for SBRT cases. The respiratory cycle and tumor motion within the cycle need to be determined for linac to track the motion accordingly. Implanted markers or radioopaque markers are employed for verification of the process. On the other hand, limited breathing approaches use abdominal compression or breath-hold techniques. Physical abdominal compression helps with overall motion control, and in particular, helps in lower lobe tumors, more influenced by diaphragm motion. Breath-hold techniques lead to smaller ITV and PTV and more sparing of the lung.

In addition to respiratory motion, setup errors are another uncertainty contributor that should be corrected to obtain correct PTV margins. A proper reproducible patient positioning reduces variation to a large extent. Laying both arms above the head permits a great choice of beam access and is usually not accompanied by many external immobilization devices for thoracic treatments. After positioning and immobilization, pre-treatment 2D and 3D imaging technologies for verification could help to identify such uncertainties. Some available technologies were introduced earlier in this chapter. Gantry-mounted or floor/ceiling-based imaging modalities are used to achieve fiducial-based 2D images for patient setup. The limitation is that this setup uses more stable anatomical parts such as bones, spine, clavicles instead of tumors for matching. Instead, using in-room 3D gantry-mounted imaging modalities provides information on soft-tissues and changing anatomy. Especially in lung tumors, regression of tumor and nodes, consolidation or opening of a collapsed segment, or similar changes are typical during treatment. These changes might lead to smaller GTV and changes in the position and motion pattern of the tumor. However, due to microscopic residuals, reducing CTV is not the safest option. When large variation exists, replanning and dose recalculation might be needed as such changes are not included in PTV calculation. This problem emphasizes the need for 3D imaging and the identification of such changes.

So far, both inter and intra-fraction uncertainties were addressed. Robotic couch and in-room imaging technologies help to overcome inter-fraction uncertainties. Intra-fraction motion management strategies use fluoroscopic imaging to track fiducial markers or electromagnetic transponders implanted nearby the tumor. This approach is invasive, requires implantation, and some tumors are not accessible for fiducial implantation. Plus, follow-up imaging with magnetic resonance imaging will not be possible anymore. Non-invasive methods benefit from the correlation of surface landmarks with internal tumor motion or the correlation of surface surrogate motion with respiratory motion models. The problem is that the surface markers do not always predict the tumor motion, and

as shown in figure 1.10, irregular breathing patterns exist. In case of lack of sufficient correlation or irregular breathing patterns, these approaches reach their limit. Even available markerless offline tracking with 4D CT assumes a regular breathing pattern. Intensity-based 2D-3D registration could provide a solution by estimating all six degrees of freedom in rigid body motion to derive an accurate motion model.[21]

One accurate approach is real-time tumor motion monitoring using fluoroscopic images from imaging systems mounted on linac. Using image guidance is inevitable for the reduction of margins which in turn leads to sparing more of the remaining healthy lung tissue which might be crucial for some patients. This imaging allows patient positioning while acquiring orthogonal projections of the tumor during the treatment. Intensity-based 2D-3D registration of acquired images with planning CT offers a real-time approach with high accuracy. Intensity-based 2D-3D registration can overcome some of the limitations that other techniques are facing. For example, it is accurate, non-invasive, independent of irregular motion patterns with no need for patient collaboration during the acquisition. These advantages are at the cost of additional dose contributions to the integral patient dose because of the kV imaging. However, when using EPID images, the exited treatment beam is recorded with no additional dose to the patient. The result of registration is then used to gate linac or shift the couch position. The limitation of this approach is that when using only one set of the projection image, the motion along the imaging beam is not resolved.

Different modalities and x-ray images from different energies have been the topic of interest for many researchers. Künzler et al. [35] used MV images of lung tumor for 2D-3D registration. Because of the limitation of MV images in providing contrast for soft tissues, registration and setup verification based on the bony structure was not helpful because the tumor moved relative to the surroundings, and focusing radiation on the tumor was challenging. In another study by Gendrin et al. [24], only kV images were used to capture motion in 5 degrees of freedom with fixed translation along the anteroposterior (AP) axis. One issue was that translation and rotation were not independent. Despite that translation along the anteroposterior (AP) axis was fixed, the rotation around LR and CC axes could still induce translation in the AP axis, as the center of rotation was not located at the center of the tumor. Also, with only the kV image set, the motion along the beam axis was not resolved, which was the main limitation of intensity-based registration. However, Furtado et al. [17] used two image sets and evaluated the registration accuracy when using only 1-kV, kV-MV, and 2-kV image sets. Two kV images resulted in the most accurate registration at the cost of more dose to the patient, whereas kV-MV image pairs were also proven to improve results efficiently, with no further dose from MV images.

As a result, orthogonal kV-MV image pair was suggested for the registration procedure by Furtado et al. [21] to resolve the motion along the AP axis. This approach also resulted in motion extraction with a reduced average error [20, 21]. In earlier studies, only angles close to AP/PA were studied and resulted in successful image registration,

whereas registration for lateral projection was less satisfactory. Another feasibility study de Cillia [14] tested different gantry angles for registration along the CC axis using the kV-MV image pair. However, motion along the AP axis and more arbitrary gantry angles needed to be investigated, which is the focus of this thesis. Such intra-fraction 2D-3D registration is not only limited to SBRT treatment but used for VMAT as well. In Furtado et al. [19], intra-fraction kV images at AP/PA direction were used for motion management at specific arcs with tumor visibility. It was shown that VMAT treatment accompanied with tumor tracking and gated linac could benefit from PTV reduction as well as dose monitoring.

The image data sets used in this study were taken during SBRT treatment of patients suffering from NSCLC. After several steps of image processing, breathing motion signal extraction, an in-house developed 2D-3D registration software was used for image registration. This software registered the tumor motion based on the combination of two orthogonal sets of planar X-ray images recorded (almost) simultaneously. The 2D images were compared to DRRs, generated from the planning CT, subsequently using a merit function to obtain the tumor displacement. This thesis focus on the evaluation of the registration results, using one set of kV images in the CC direction in 5DOF, as well as using the kV-MV image pair in both CC and AP direction in 6DOF. Then the registration results were compared respectively with the annotated diaphragm motion in CC and extracted MV motion for AP direction, used as a ground truth. The aim was to investigate whether using paired kV-MV images in 2D-3D registration could improve the registration result any further. The registration of image-paired used in previous studies was mainly focused on the kV-images along or close to the AP axis as the tumor and its surrounding structures are not equally visible in all directions. Therefore, it is tried to examine the usability of this approach for arbitrary gantry angles used in SBRT.

2 Image Registration - Theoretical Background

Image registration means geometrically aligning images taken under different conditions such as different angles, different times, or different modalities. It has a wide range of applications in radiotherapy, such as segmentation, combining information of multiple imaging modalities, response assessment, patient positioning in IGRT, and adaptive treatment planning.[10] Connecting imaging device and physical space of the patient in radiotherapy is achieved by registering fixed extrinsic frames or markers on the patient during scanning and operation, registration of intrinsic markers to pre-operative images as well as linking intra-operative and pre-operative images. Then the image registration algorithms require a geometric transformation, a registration metric, and an optimizer to find the best transformation to align the so-called moving image to the stationary image. Every registration algorithm tries to optimize the transformation parameters to maximize or minimize the similarity measure used to compare the two images, as shown in figure 2.1. This measure is called the merit or cost function.

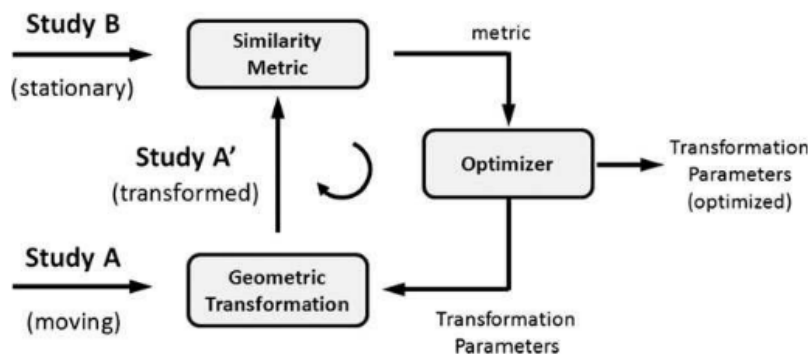


Figure 2.1: Basic process of the image registration algorithm. (Figure from [10])

Based on the number of parameters used, the registration could be rigid, affine, and non-rigid. Rigid registration is appropriate when the imaged object is itself rigid such as bones. The deformable nature of soft tissue requires extra parameters to quantify its structural changes. In rigid registration, transformation preserves the distance between all points in the image and allows for only, *translation and rotation*. If the transformation allows for *scaling and shearing*, it is called affine registration. More complex deformation

with more parameters is referred to as a non-rigid registration or deformable registration. Rigid registration can be used as the initial step for performing non-rigid registration, followed by a search for a vector field that takes every pixel of the moving image to the most similar pixel of the stationary image to compensate for the non-rigid anatomical changes. There are different approaches for different anatomical regions, but almost all algorithms use a model to describe the deformation and, as a result, will have limitations. An overview of methods for performing non-rigid registration with main components of a deformation model, a matching criterion, and an optimization method was published in Sotiras et al. [49]. Despite all available approaches, non-rigid registration requires time-consuming calculation which makes it unsuitable for clinical application. In earlier relevant studies, the tumor tissue has shown a rigid behavior; therefore, rigid registration applies to the scope of this thesis. However, if the tumor shows a deformation, then a non-rigid registration is needed to account for the deformation.

2.1 Classification of Image Registration Methods

There are different applications and types of registration. Maintz and Viergever [40] presented nine criteria to classify various image registration methods, which are summarized in table 2.1:

Table 2.1: Summary of registration classification

Classification of registration						
Dimensionality	Spatial dimensions (2D-2D, 2D-3D, 3D-3D)	Time series with spatial dimensions (2D-2D, 2D-3D, 3D-3D)				
Nature of registration basis	Extrinsic (invasive, non-invasive frames, fiducials)	Intrinsic (anatomical, geometrical landmark, segmentation with rigid, deformable model, and reduced, full image content voxel property)	Non-image based (calibrated coordinate systems)			
Nature of transformation	Rigid	Affine (maps parallel lines onto parallel lines)	Projective (maps lines onto lines)	Curved, Elastic (maps lines onto curves)		
Domain of transformation	Local (subsection of image)	Global (entire image)				
Interaction	Interactive (with and without initialization supplied)	Semi-automatic (user initialization or user steering, or both)	Automatic			
Optimization procedure	Parameters computed		Parameters searched for			
Modalities involved	Monomodal	Multimodal	Modality to model (statistical, anatomical, geometrical model)	Patient to modality (intra-operative application)		
Subject	Intrasubject	Intersubject	Atlas			
Object	Head	Thorax	Abdomen	Pelvis and perineum	Limbs	Spine and vertebrae

The highlighted cells in table 2.1 represent the registration implemented in this study. This study is centered on the registration of 3D planning CT to 2D intra-operative X-ray images of lung tumors of the same patient. Thus, it is an intra-subject multimodal 2D-3D registration of thorax images. The registration is easier between x-ray and DRR, compared to other modalities such as MR. It is because they both share the same physical properties. Registration is estimated by optimizing the similarity measure calculated between a DRR and an X-ray image. Different similarity measures are used to measure the correspondence between DRRs and X-ray images with local intensity changes producing a better result than global intensity measures. Registration is performed with 6 DOF; with three of them corresponding to translations and the other three to rotations. Without point pairs and by using whole-image-content, the registration parameters have to be searched for, iteratively, by minimizing the distance between the corresponding feature sets. FIRE, the 2D-3D registration software used in this thesis, is semi-automatic as it is essential that the user provides some initial guess to the algorithm and validate the results of registration.

The *nature of registration basis* is one of the classifications mentioned in the earlier table 2.1. Furthermore, the 2D-3D registration algorithm can be categorized as feature-based, intensity-based, and gradient-based using projection, back-projection, and reconstruction to bring the image information into spatial correspondence. This is elaborated and summarized in figure 2.2. In feature-based approaches, the sum of spatial distances between corresponding features, extracted from pre- and intra-operative images or models, are minimized to find the best match. These features could be extrinsic, such as implanted fiducial markers, or external objects attached to the patient. Implanted fiducial markers are known as the gold standard due to their high accuracy with the disadvantage of being invasive and dependent on accessibility to the tumor location. As a result, there is a shift from extrinsic features to intrinsic features such as distinctive points on anatomical structures, surface, and modeling of anatomical structures. These are less invasive and less accurate alternatives, with features being projections from models or back projections of virtual x-rays from 2D images. Most feature-based registration requires segmentation and user interaction as part of the process, which is the major drawback of these approaches.

An alternative approach uses intensity information of the pixels and voxels of the image instead, where no segmentation is required anymore. Intensity-based approaches take advantage of a similarity measure for comparison and are the basis for most clinical registration approaches. However, the gradient-intensity approach uses 2D, 3D gradient vectors of the images for comparison. Intensity gradient is faster and has the advantage of registering images of different modalities; while using the intensity information, which is more accurate. If the intensity information of pixel and voxel is used, 2D-3D registration becomes a transform, mapping two coordinate systems by comparing virtual x-ray projection rendered from CT to actual x-rays. There are two ways to compare 2D and 3D images; we can reconstruct 3D images from a set of 2D images and then apply a 3D-3D

registration method, or we can compute 2D information projected from 3D images and perform a 2D-2D registration. Reconstruction-based methods are for 3D-3D registration, which is slower, case-specific and required many interventional images for reconstruction. With a low number of images, the projection-based 2D-2D approach is mostly preferred and used because the quality of the 3D images reconstructed from 2D images is poor. On the other hand, projection based 2D-2D registration requires DRR calculation, which can be time-consuming. This problem could be overcome with a faster DRR generation technique or limiting the DRR to the ROI. Another problem is that its application is limited to images from the same image modalities, plus projection of 3D data to 2D data could result in information loss.[41]

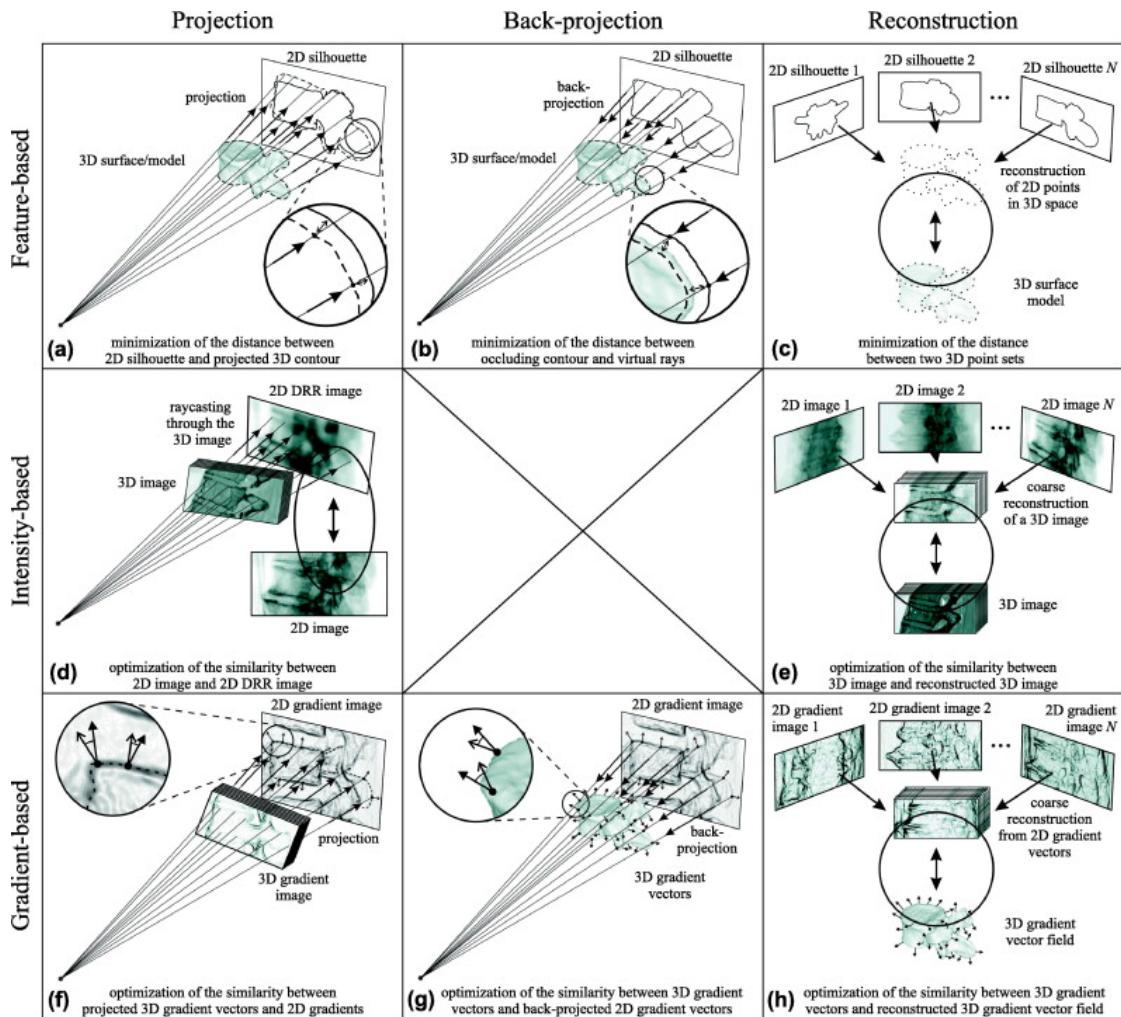


Figure 2.2: 2D-3D registration methods according to the nature of the registration basis and strategy to achieve spatial correspondence. (Figure from [41])

2.2 2D - 3D Intensity-based Registration

The intensity-based approach using projection is the focus of this study. It consists of the following steps, explained in details:

- Generation of DRRs
- The choice of similarity measure to compare the DRRs and actual X-rays
- The choice of the optimization method to maximize or minimize the value of similarity measure by iteratively changing the translational and rotational parameters of the DRR rendering until a termination criterium is reached.

2.2.1 DRR

DRR is a simulated X-ray image derived from simulating the attenuation of virtual X-rays. Iterative production of DRRs is the first step in the intensity-based 2D-3D registration. Its quality and the time efficiency of the production of DRRs have a great impact on the registration. *Direct volume rendering* techniques lead to a direct transfer of 3D data into 2D without any polygon representation, making these techniques suitable for Medical imaging. Popular direct volume rendering algorithms are ray casting, splatting, and shear warp rendering.

Ray casting is the conventional and most popular approach. The algorithm works by virtually “throwing” the voxels onto the image plane, analogous to the production of radiographic films. Rays from a virtual X-ray source pass through a CT volume, which is considered the patient model. Then it ends up on a virtual film. Inside these volumes, the samples are taken at specific intervals and composed later to compute the final pixel. The Hounsfield units associated with the crossed CT voxels provide the estimation of the ray attenuation. Ray casting is an image space algorithm and works on every pixel of the target image. As a result, all the volumes, even empty ones, require the same amount of time. On the other hand, sampling at certain intervals could result in skipping the thin structures. There are many optimization techniques available to overcome these problems. This technique is computationally expensive, but it offers good quality. Therefore used as a reference to evaluate other DRR rendering algorithms.

Splat rendering is an object base approach that computes the contribution of every voxel of the volume to the final image by projecting every voxel into the image plane. The projected voxel splat on a few pixels, which is referred to as voxel footprint. Different rendering styles could be used, depending on which voxel footprints are used in the image construction. Plus, the footprint size influences the performance. Its advantage over the ray casting method is faster DRR generation if an appropriate voxel threshold is chosen. However, aliasing artifacts reducing the image quality is a disadvantage of this method.

2.2.2 Merit Function

The selection of a proper similarity measure is an important aspect for a successful 2D-3D registration. In registration tasks, the best way to map one image onto another is a matter of definition. Therefore the result of a registration always depends on the chosen similarity measure. In intensity-based methods, the similarity measure is calculated using a pixel-wise comparison compared with feature-based methods in which distance is calculated. We have different merit measure according to the used modalities involved in the registration :

Intramodality registration

Algorithms that register images of the same modality by optimizing a voxel similarity measure. Because of the similarity of the intensities, the subtraction (Sum of Squared Differences), correlation and ratio techniques (Ratio image uniformity) can provide good registration results.

Intermodality registration

The relationship between the intensities should be taken into consideration when using images of different modalities. Mutual information(MI) and rank correlation(RC) are examples of this type of registration.

In an ideal case, the similarity measure should have a broad capture range and converge at an optimum for the aligned images without falling at the local optima. Some of the the most frequently used merits for DRR-based registrations are global intensity correspondence such as normalized cross-correlation, mean square difference, mutual information, versus local intensity changes such as gradient correlation, gradient difference, and pattern intensity. In this thesis, only intensity-based merit functions for intermodality registration are considered, therefore some of the tested merits for 2D-3D registration are briefly presented here:

- **Sum of Squared Differences (SSD)**

It uses the square of the difference between all pixels as a measure of similarity. It is, therefore, highly sensitive to the intensity differences among the images and only works when images have similar gray values but differ in spatial orientation.

$$M_{SSD} = \frac{\sum(I_{Base} - I_{Match})^2}{N} \quad (2.1)$$

with N being the number of voxels and I as the intensity. Using the sum of absolute differences (SAD) rather than SSD can reduce the effect of outlier voxels.

$$M_{SAD} = \frac{\sum(I_{Base} - I_{Match})}{N} \quad (2.2)$$

- **Cross-Correlation**

Cross-correlation assumes a linear relationship between the intensity values of images, which makes it only suitable for intra-modal imaging. It compares the pixel

at every position for measuring the similarity.

$$M_{CC} = \frac{\sum_{ij}(I_{ijBase} - \bar{I}_{Base})(I_{ijMatch} - \bar{I}_{Match})}{\sqrt{\sum_{ij}(I_{ijBase} - \bar{I}_{Base})^2 \sum_{ij}(I_{ijMatch} - \bar{I}_{Match})^2}} \quad (2.3)$$

M_{CC} being the cross-correlation, I the pixel intensity, and i, j the pixel coordinate, and \bar{I} is the mean intensity value of the image. Because cross-correlation is sensitive to voxel value changes a normalized version is introduced to overcome this problem. Also, preprocessing, such as low pass filtering and edge detection, helps to overcome the linear intensity problem between images.

- **Correlation Ratio**

The correlation Ratio takes advantage of the functional dependence of the compared images. A function that maps each image intensity to the other image intensity and measures this functional relationship could be used as a similarity measure.

$$M_{CR} = 1 - \frac{1}{\sigma_I^2} \sum_j p_j \sigma_{I|j}^2 \quad (2.4)$$

with σ_I^2 being the variance and $\sigma_{I|j}^2$ being the conditional variance.

- **Pattern Intensity**

Pattern Intensity uses the structure of the image for comparison. An image sub-volume that contains a rigid structure visible on both images is used for registration. The DRR from the sub-volume is then computed and subtracted from the reference image. Then the amount of disorder in the resulting image after subtraction is processed as follow:

$$M_{PI} = \sum_{i,j} \sum_{(i-k)^2+(j-l)^2 \leq r^2} \frac{\sigma^2}{\sigma^2 + (I_{sub}(i,j) - I_{sub}(k,l))^2} \quad (2.5)$$

with P being the pattern intensity metric, i, j as pixel coordinate, r defining the area to search for structure, k, l being the coordinate of the designated area, σ as a sensitivity measure for structure, and I_{sub} being the fluoroscopic image minus the DRR of the segmented rigid structure. Moreover, it is also applicable to the entire image without the need for pre-segmentation.[44] The alignment of images before subtraction results in a smoother subtracted image. However, this merit has a narrow capture range and only works for registration close to the final results.

- **Mutual Information**

Mutual information assumes a statistical dependence between the compared images. It measures the amount of information each image contains about the other, and the registration task become, reducing the amount of information in the combined image. We can consider that the pixel values histograms will be the equivalent to the probability distribution function for each image. Joint distribution is the

joined histogram of the images, which describes the correlation of intensities of the two compared images.

$$MI(I_{Base}, I_{Match}) = \sum_{I_{Base}} \sum_{I_{Match}} p(I_{Base}, I_{Match}) \log \frac{p(I_{Base}, I_{Match})}{p(I_{Base})p(I_{Match})} \quad (2.6)$$

$MI(I_{Base}, I_{Match})$ is the mutual information, $p(I_{Base})$ and $p(I_{Match})$ are the marginal probability density functions, and $p(I_{Base}, I_{Match})$ is the joint distribution. It is assumed that the dependence between the distribution of gray values of the correctly aligned images is maximal. Misregistration will result in a decrease in the measure. Its advantage is the transition from pixel gray-values to PDF so that multi-modal matching is possible by an appropriate definition of the probability. [7]. A problem of mutual information is that it compares local intensities and does not account for the surrounding pixels. Incorporating the dependence of the gray values of neighboring voxels, which is called *spatial information*, would improve registration. Many variations of it have been proposed and studied. Different methods are summarized by Pluim et al. [46].

- **Stochastic Rank Correlation(RC)**

It is a merit function based on spearman's rank correlation, proposed by Birkfellner et al. [8].

$$M_{RC} = 1 - \frac{6 \sum_{n=1}^N \Delta \rho_n^2}{N(N^2 - 1)} \quad (2.7)$$

with N being the number of pixel and $\Delta \rho_n^2$ being the squared rank difference $\Delta \rho_n^2 = (\rho_{Base} - \rho_{Match})$. This merit function in comparison with cross-correlation, does not require a linear relationship between the two images and is more robust to high-intensity artifacts. However, because of the sorting operation involved in this approach, the main drawback is the higher run time. This higher run time can be reduced by using a static random mask that selects a small percentage of image content. Birkfellner et al. [8] has shown that by sparse sampling, meaning using 3-5% of image data for the calculation of merit function, same result, and same computational effort as cross-correlation can be yield. Figl et al. [16] showed that the sorting step could be omitted, and if significant differences in the histogram content for the DRR and the x-ray image is present, the rank correlation could yield the most accurate result in comparison with cross-correlation, correlation Ratio, and Mutual information.

2.2.3 Optimization

The optimization goal is to find the best set of transformation parameters to obtain the best image alignment given by the merit function. The merit function gradient guides the optimization process to find an optimum value. This search continues until a termination criterium, such as the number of iteration or a merit function threshold, is met. The choice of optimization influences the registration results significantly. Because

of the presence of local optima, it is not clear if the founded optima corresponds to the global minimum (or maximum). There are global optimizers methods that try to search for the global maximum or minimum. Since these methods are slow, and can not guarantee a global result, the local optimizers are used instead. However, at the cost of getting trapped in local optima. Both the local and the global optimizers are dependent on starting parameters, step width, and termination criterium. Some different types of optimization algorithms are briefly described below:[50]

- **Geometric Algorithms** such as downhill simplex:

It is a local optimizer that operates on the merit function and has the advantage of not requiring any derivation calculation. It uses a triangular shape or simplex; polytope of $N + 1$ vertices with N as the dimension number. It describes the correlation between sample points and is used for choosing the next sample position during the search. Simplex finds its way downhill by changing its shape. Each iteration of downhill simplex consists of sorting, operation implementation, and replacement of the former worst point. The worst vertices are replaced by better positions through different operations, as shown in figure 2.3.

Reflection

The worst sample is reflected at the center of gravity of the remaining samples.

Expansion

It is the extension of reflection, meaning that the segment between the center of gravity and the new point enlarge so that the new point is farther.

Contraction

If the contracted point value is better than the worst point value, it allows the simplex to change direction. It is the used when the reflected point can not improve the situation.

Full Contraction

It allows simplex to follow curved valleys into the direction of optimum and is used when contraction is not possible.

- **Gradient-based algorithms** such as the conjugate gradient method:

Gradient-based algorithms are time-consuming local optimizers operating on the gradient of the merit function to find the optimum. In the steepest descent method, the user chooses the initial position, and until a minimum is found and chosen for the next iteration position, the direction of the gradient is followed. The problem with this method is that the initial guess needs to be in the direction of the global minimum, plus, orthogonal direction change in every iteration. The conjugate gradient is the improved version of the steepest descent algorithm. The improvement in the conjugate gradient method is yield by choosing the new direction as a conjugate to the previous one relevant to the function to minimize. Regardless of the improvement, both methods are still time-consuming because of the iteration number and the need for function evaluation for the gradient calculation.

Other different gradient-based methods only differ in the way the search direction

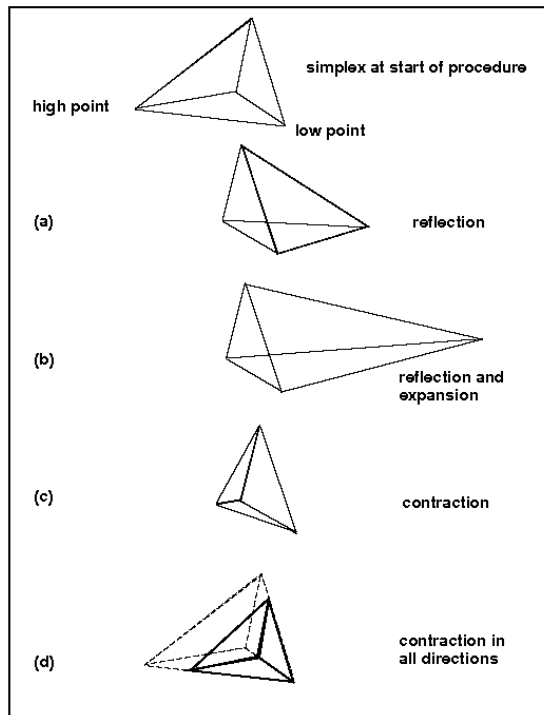


Figure 2.3: possible outcomes for a step in the downhill simplex method. (Figure from [47])

is selected. Powell method, least-square method, as well as Quasi-Newton method, are among those. Powell conjugate direction is a popular method with no need for calculating the function derivatives, but it still suffers from local optima. This method transforms the multi-dimensional minimization problem into a sequence of the one-dimensional minimization problem. It minimizes a quadratic function in a finite number of steps using the idea that adjusting search directions improves convergence. A new parameter guess is determined by a sequence of line searches in each iteration, starting from the previous parameter guess. The new parameter guess can therefore be written as a linear combination of all search vectors. Afterward, one of the search directions gets replaced in favor of the new search direction. Iteration continues until convergence for quadratic functions is reached.

- **Probabilistic Algorithms** such as simulated annealing:
 This algorithm is an example of a global optimizer, and it is not generally used in image registration. It is based on the Monte Carlo algorithm, which uses random steps that allows a worse solution to avoid local optima. The defined probability for providing this condition decreases over time and allows the algorithm to converge to an optimum.

2.3 Evaluation of Registration Result

No registration software could be accepted as a clinical tool without validation. We need to differentiate between verification and validation of registration software. Verification is the process by which the registration software is checked to do what it is specified to do whereas in validation certain accuracy in performance is expected. Estimation of precision and accuracy of the registration results is a substantial step. *Precision* refers to the typical systematic error, while *accuracy* needs a gold standard. The most common strategy for validation is to compare the system against a gold standard, or any system with high accuracy. Gold standards are based on computer simulations (typically by acquiring one image and generating a second with a known geometrical transformation, phantom images), cadavers, or patient images. Patient images is preferred for validation however, it suffers from the difficulty of establishing the true transformation between acquired images as opposed to simulated images. In the non-rigid registration, there is no gold standard available. In general, for clinical application, even for rigid registration, a gold standard is not always available. Instead, different validation metrics are proposed in Christensen et al. [12] to evaluate the performance of the registration. There is an emerging need for public databases and validation protocols. Phantom study, and simulation, as well as using the results of other accurate methods for cross-validation, are among the current standard solutions.

Qualitative measures such as visual checks could especially be helpful for the evaluation of registration results in clinical practice. The most frequently used qualitative techniques are Split-screen and checkerboard displays, Image overlay displays, difference image displays, and Contour/structure mapping displays described in figure 2.4. [10] To quantitatively evaluate the registration, some measures introduced in Brock et al. [10]; such as target registration error (TRE), mean distance to agreement, dice similarity, and the Jacobian determinant. These measures and their tolerance for standard treatment is listed in table 2.2. Among those, target registration error (TRE) is most widely used. TRE is the distance between pre-defined locations (such as fiducials, surface points, or arbitrary chosen points) and the target position obtained by registration. The maximum TRE should be below the clinically tolerable error. Furthermore, checking for consistency helps to evaluate the stability of the registration by comparing the transformation obtained from the registration of two images (A and B) in both direction; registration of A-B versus registration of B-A.

There is no gold standard available for this work. However, the pulmonary tumors correlate to the diaphragm motion of the patient if its position is not far from it. Therefore, the annotated diaphragm motion is acting as ground truth for the CC direction, and the extracted motion from perpendicular MV images serves as ground truth for the AP direction. Plotting registration results with their corresponding extracted motion provides a visual inspection. Moreover, the correlation coefficient is used as the numeric metric to validate the correlation between the registration result and the extracted motion.

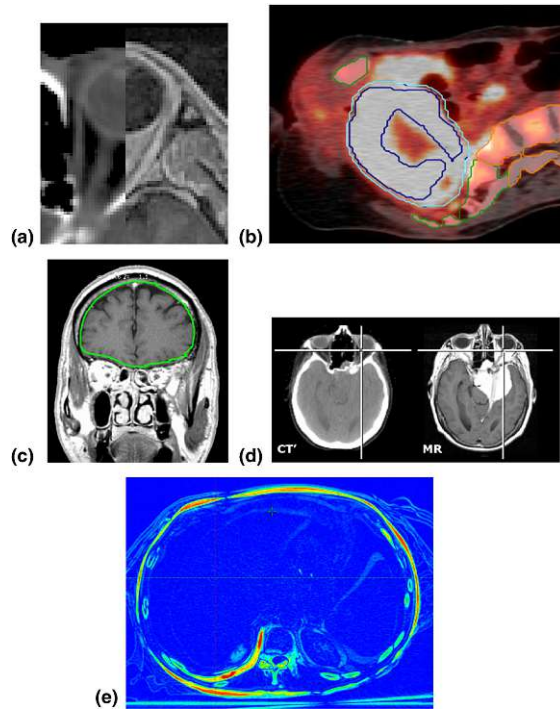


Figure 2.4: Examples of qualitative measures for evaluation of registration results: (a) Visual validation using split-screen displays of MR and reformatted CT. (b) Region of interest delineation overlaid on a fused PET-CT. (c) Visual geometry validation of overlaid CT brain structure over MR images. (d) Side-by-side display with the linked cursor. (e) Difference image showing good registration in blue and more uncertainty in the bone and surface with yellow, green, red color. (Figure from [10])

Table 2.2: Quantitative metrics to evaluate image registration. (Table from[10])

Technique	Evaluation metric	Tolerance
Target registration error (TRE)	Point-based accuracy metric using implanted or naturally occurring landmarks visualized on a pair of images	Maximum voxel dimension (~2–3 mm)
Mean distance to agreement (MDA)	Mean surface distance between 2 contours on registered images	Within the contouring uncertainty of the structure or maximum voxel dimension (~2–3 mm)
Dice similarity coefficient (DSC)	Volumetric overlap of 2 contours on registered images	Within the contouring uncertainty of the structure (~0.80–0.90 ³)
Jacobian determinant	Volume expansion or contraction resulting from a deformable image registration	No negative values, values deviating from 1 as expected from clinical scenario (0–1 for structures expected to reduce in volume, greater than 1 for structures expected to expand in volume)
Consistency	Independence of an algorithm to the direction of the registration (image A to image B or image B to image A)	Maximum voxel dimension (~2–3 mm)

3 NSCLC Patient Study - Material and Methods

3.1 Patient Data

A subset of 5 patients out of available data from 20 patients suffering from NSCLC was selected for this study. These patients were undergoing SBRT at the Radiotherapy department of the AKH Vienna. Typical total doses delivered to the tumor reach from 45 to 80 Gy, depending on factors, such as tumor size or fraction scheme. The treatment included three fractions with typically seven gantry angles irradiated per fraction. The patients positioned under the BodyFIX system (Medical Intelligence, Elekta, Germany); which is a fixed vacuum mattress with an abdominal pressure plate for immobilization, treatment, and imaging. Distributed tumor position, and a wide range of gantry angle were kept in mind when choosing the patient subset.

The tumor position significantly influences the evaluation of the registration results. Therefore, the patient tumor position illustrated with the help of CTV or ITV, when available in green and PTV in magenta, as shown in figure 3.1. For each patient, a gantry angle close to 90° was chosen to have a better illustration with an exception for patient 12, that only a lateral angle near 270° was available.

- (a) **Patient 2_** Gantry Angle 98° , with a lateral, cranial, posterior tumor.
- (b) **Patient 5_** Gantry Angle 80° , with a lateral, anterior tumor.
- (c) **Patient 6_** Gantry Angle 110° , with a lateral, caudal, posterior tumor.
- (d) **Patient 9_** Gantry Angle 80° , with a medial, caudal, anterior tumor.
- (e) **Patient 12_** Gantry Angle 280° , with a caudal, centrally located tumor.

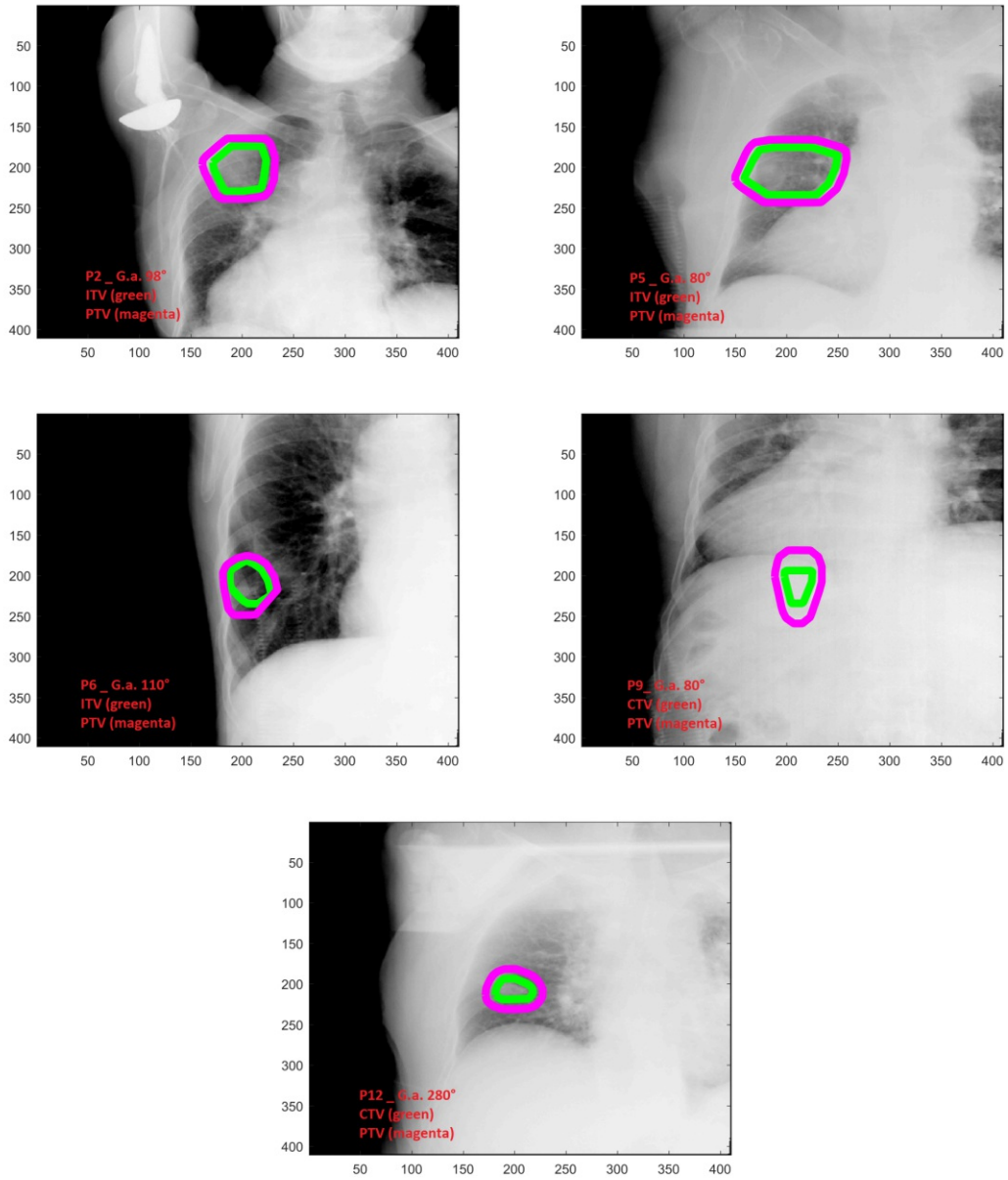


Figure 3.1: Tumor position in the studied patients

As the first step, a pre-treatment CT scan was performed for every patient with Siemens Somatom Plus 4 Volume Zoom (Siemens AG, Erlangen, Germany) at 120 kVp and 156 mAs with an interslice resolution of $0.97 \times 0.97 \text{mm}^2$ and 4mm slice thickness. For each fraction, a CBCT scan was performed for a daily setup with CBCT system XVI from Elekta Synergy LINAC (Elekta Oncology Systems Ltd, Crawley, UK). This LINAC

system, used for the treatment, provides X-rays of maximal energies of 6, 10, and 18 MV with both MV and kV imaging modalities. Each fraction lasts about 30-85s when both kV- and MV-fluoroscopic images were captured as the basis for the later performed registrations. The MV images obtained from the MV imaging device (iViewGTTM) or the so-called EPID system. It is mounted opposite to the treatment head for the acquisition of planar MV images utilizing the treatment beam as well as providing the possibility of in-room tomography and fluoroscopy. The MV images were acquired at a frequency of 2.1 Hz throughout the entire treatment delivery, with no increased delivered dose. The kV imaging modality called XVI (X-ray Volume Imaging) is mounted on a retractable robotic arm, orthogonal to the treatment beam used for acquiring projection images for radiography, fluoroscopy, and CBCT. The kV image acquisition had to start manually. Up to 200 kV images acquired at a frequency of 5.4 Hz.[14] The alignment of CBCT to X-ray images was trivial since both were from the same device and at the same patient position.

3.2 Soft- and Hardware

In this study, 3D-3D, and 2d-3D image registration, was implemented with the following softwares:

- **Analyze**

Analyze (AnalyzeDirect, Inc., Overland Parks, KS, USA) is a commercial software package developed by the Biomedical Imaging Resource (BIR) at Mayo Clinic for multi-dimensional and multi-modality image processing. Analyze 7.5 format, the file format for medical volume data, store the medical images in two files; .hdr as the header with additional image information and .img file, which contains the numerical information. However, in a newer modified format called AVW, the header, and the image information are stored in one file.

- **Fast Image Registration (FIRE)**

FIRE is a free open source software suite used for research in IGRT. It is developed as a project *Real-time 2d-3D image registration in radiation oncology* at Medical University of Vienna by Furtado et al. [18] FIRE allows performing an intensity-based 2D-3D registration for intra-fraction tumor tracking with a frequency of about 5 Hz. 5Hz is chosen since the kV imaging device on LINAC at AKH is 5Hz, or else, FIRE is capable of image registration in 6 degrees of freedom with a frame rate up to 11 Hz. The software allows the combination of different techniques for DRR calculation, choice of merit function, and optimizer. Both splat rendering and ray casting, as well as the five introduced similarity metrics - mutual information, cross correlation, rank correlation, pattern intensity, correlation ratio - and the introduced optimizers - Simplex, Powell, and Conjugated Gradient- are implemented in the software. First the initial guess, image intensity, and region of interest(ROI) for each image is set and then the software allows for single registrations, as well as image sequence registration.

All the steps to prepare the x-rays images and masks for image registration and motion signal extraction, as well as plotting and result evaluation were implemented with in-house built scripts in Matlab version R2013a. All steps were performed on a personal computer equipped with an Intel Core i5 4 core CPU of 3.4 GHz each and an NVIDIA GeForce GTX 780 graphics card and 8 GB RAM.

3.3 Workflow

For each patient data, the following steps were followed :

3.3.1 Data Preprocessing

First, CT and CBCT image files, generated on the imaging devices, were stored in a folder containing the different reconstructed slides. Then the structures such as PTV, CTV, ITV and body contours were delineated by a physician from the planning CT. Then, these structures were extracted in terms of vertices from DICOM-RT data to be used later for building the masks on 2D images. The segmented body contours were used later to mask the volume data and were saved in NifTI (Neuroimaging Informatics Technology Initiative) format, which was a medical volume data format used by Analyze 7.5.

The 2D images were interpolated to an isotropic pixel size of $1mm^2$ and needed to be organized and converted from .his (Kv images) and .jpg (MV images) format to .pgm (Portable Gray Map) which was a simple image file format used by FIRE. Also, the contrast of the x-ray images was improved by intensity scaling and windowing because the raw image data offered hardly any visible contrast. *imadjust* in Matlab was used, which saturates 1% of the data at low and high intensities, to improve contrast.

3.3.2 3D-3D Registration

The pre-treatment CT and the daily CBCT were aligned with a 3D-3D registration, to compensate for the daily setup variations. For this reason, a 3D-3D registration was performed in Analyze. First, both volumes were converted to the same intensities and interpolated to an isotropic voxel size of $1mm^3$. $1mm^3$ was chosen to increase the performance of the registration algorithm due to the smaller data size. The body contour mask from the previous step helped to remove the extra pixels around the CT volume. The CBCT was then padded with zeros to match the CT volume. Then the cleared CT and the padded CBCT were registered with CBCT as the *base volume* and CT as the *match volume*. The CT was the one matched in the 3D-3D registration as the image quality of the planning CT was superior to the image quality of the CBCT. The registration interface between the CT and CBCT with the manual registration matrix on the lower right corner is illustrated in figure 3.2. Different visualization tools could be used to visually inspect the effects of changing the registration matrix on the *fused volume*. After applying the registration matrix, the 3D transfer matrix, as well as the final fused volume were saved for later use.

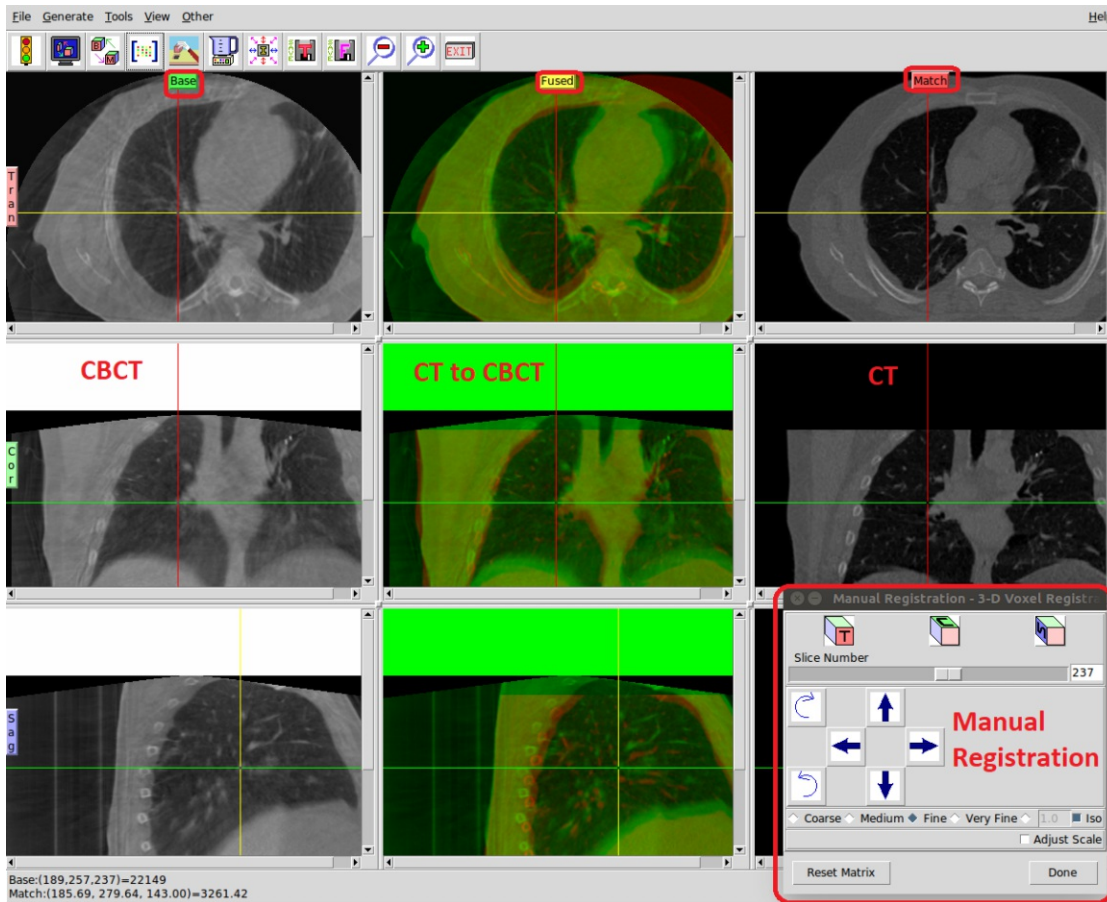


Figure 3.2: Registration interface in Analyze shown for patient 20, Fr.2

3.3.3 Mask Generation

The registration was applied on a ROI centered around the PTV, where the assumption of a rigid transformation was valid. Using ROI with the help of masks was necessary to reduce the rendering time for DRR generation, plus focusing the registration on the PTV instead of other structures such as bones or soft-tissue. Then the extracted PTV, CTV, and other vertices of different structures of pre-treatment CT volume were projected onto the kV images by taking the earlier obtained transform matrix into account. The masks were obtained for every gantry angle and every fraction of the kV images. In figure 3.3, extracted structures such as CTV, PTV, ITV with different margins as well as lungs, myelon, and the esophagus was delineated.

The *roipoly* function in Matlab was used for defining the ROI in MV images. With *roipoly*, the tumor margins on the MV images were annotated manually, as shown in figure 3.4. It returns the mask as a binary image, setting pixels inside the ROI to 1 and

pixels outside the ROI to 0. The pixel density, additionally, the size of both kV and MV images, could be changed before the delineation of the masks.

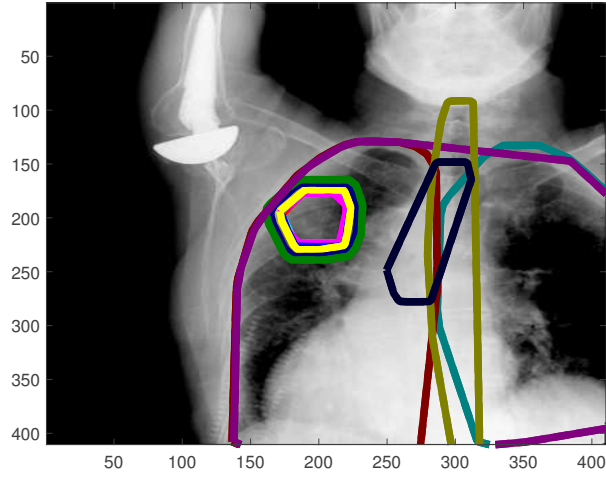


Figure 3.3: Examples of delineated structures on a kV image for patient 2, Fr.2, g.a. 98°

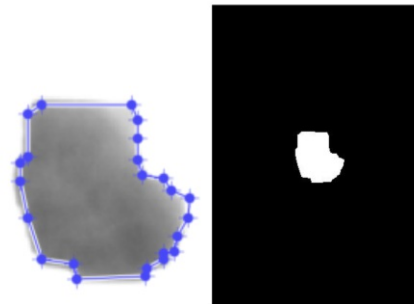


Figure 3.4: Annotation with "roipoly" in Matlab (left), the final saved MV mask (right) shown for patient 2, Fr.2, g.a. 98°

3.3.4 Motion Extraction

As mentioned earlier, kV and MV image acquisition were at different frame rates and did not start simultaneously. For this reason, the diaphragm motion and MV motion signals were required to establish the time correlation between the image sequences. These signals also served as ground truth for the verification of the registration results later. The following approaches were used in detecting shifts in image sequences of this study:

- **Cross Correlation**

One approach was to use cross correlation to calculate the shift between two images. If the two signals used for correlation represent the information of the images, the maximum of the correlation function indicates the shift between the structures seen on the images. Normalized cross correlation of an image such as f and a template such as t is defined as

$$\gamma(u, v) = \frac{\sum_{x,y} [f(x, y) - \bar{f}_{u,v}] [t(x - u, y - v) - \bar{t}]}{\sqrt{\sum_{x,y} [f(x, y) - \bar{f}_{u,v}]^2 \sum_{x,y} [t(x - u, y - v) - \bar{t}]^2}} \quad (3.1)$$

Where \bar{t} is the mean of template and $\bar{f}_{u,v}$ is the mean of $f(x,y)$ in the region under the template. [58]

- **Hough Transform**

Another approach for motion annotation used edge detection followed by a Hough transform searching for circles. Hough transformation is an algorithm to detect geometric objects such as circles or lines. After performing edge detection, hough transform searched for circles representing the circle shape of the diaphragm. Based on edge detection and Hough transformation performed on each image, it was possible to determine the shift of a structure between two consecutive images and this was used for diaphragm motion extraction on kV images.

- **Manual Annotation**

The user could also pick up a point on the diaphragm on one of the images and manually follow and annotate the motion in each image. This was used for diaphragm motion extraction on kV images when edge detection and Hough transform failed to provide a satisfactory result.

For this task, as illustrated in figure 3.5, edge detection plus Hough transform on searching for circles was used to detect the diaphragm motion on kV images. After the adjustment of intensities with the scroll bar on top, an ROI was selected on one of the kV images, then a distance point was chosen within the ROI and on the diaphragm. Changing the Edge threshold and binary threshold could enhance the performance of edge detection and Hough transform. With an appropriate threshold chosen, the green circle did match the diaphragm shape. Using the scroll bar at the bottom, the reliability of the transform could get checked on the other sequences of the images of the same

gantry angle. When the Hough transform matched the diaphragm motion in the whole image sequence, then the detected motion along the CC axis was saved, pressing the *Auto* button. The problem was that the diaphragm was not always in the form of a definable circle in all images; so in many cases Hough transform in combination with edge detection was not working accurately. For such inaccurate cases, a manual annotation for extraction of motion along CC was preferred by choosing the *manual* button and following a point on the diaphragm visually.

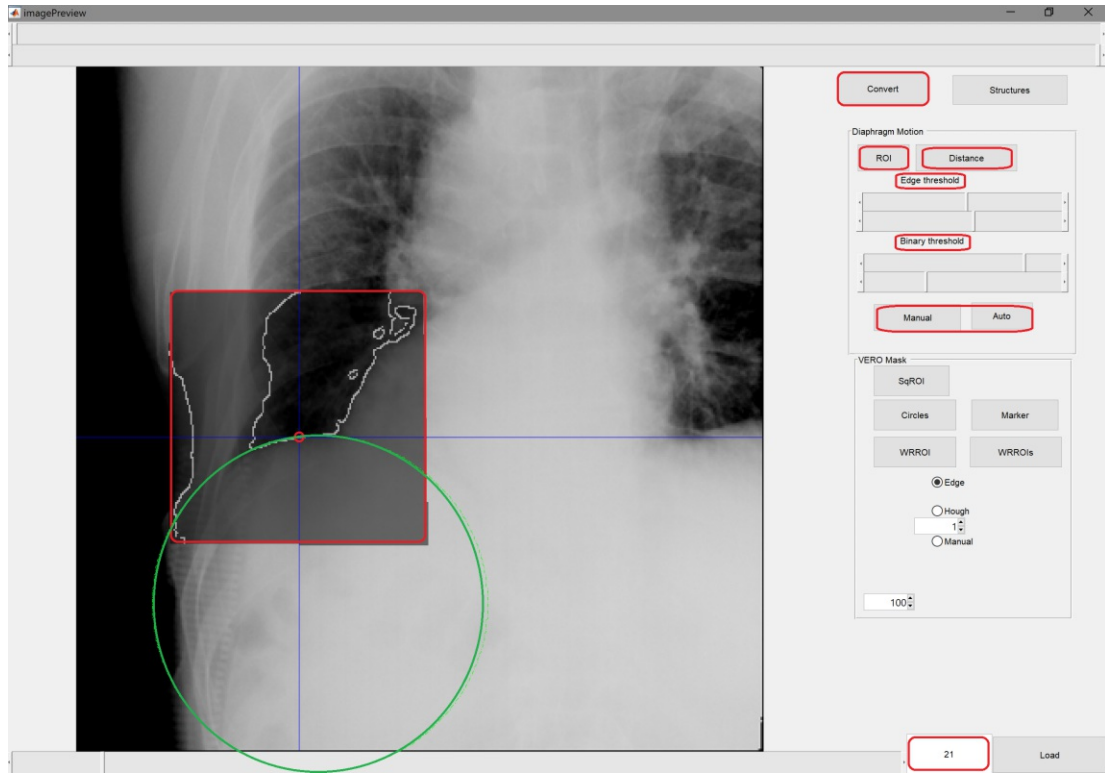


Figure 3.5: Image processing method to extract the diaphragm motion, with a defined region of interest, where the white dots resulted from edge detection and the green dots from a Hough transform for circles shown for P1, Fr.1, g.a. 100°

Both kV and MV image sets shared one axis corresponding to the CC axis of the patient. Motion extraction along x and y-axis was feasible for the kV image set by following the diaphragm motion. Diaphragm displacement along the y-axis on the kV image sequence was a sinusoidal movement correlated with pulmonary tumor motion. These displacements were later served as a reference and were compared with the 2D-3D registration result along the CC axis for the kV image set. However, by only using the kV image set, the z motion signal could not be extracted, and for this reason, using the MV image set helped to extract MV motion along the x and y, with x corresponding to the z axis of the kV image set.

For MV images hardly containing any explicit structure, it was hard to implement a proper manual annotation or a Hough transform. Instead, a rectangular ROI was selected from one of the MV images. Then, the normalized cross-correlation of the MV image and the selected template was calculated with the help of *normxcorr2* function. The result was displacement along the x and y-axis corresponding to the AP and CC axis of the patient. This process usually involved complications and needed many repetitions to obtain a good result. For apparent intensity changes and small motion amplitudes, the cross-correlation did not work correctly, and the result was a very noisy extracted motion. The extracted motion along the CC axis, in both kV and MV image sets, was used in the next step finding the corresponding kV sequence as well as the corresponding breathing motion. The corresponding breathing motion served as a reference and was compared with the 2D-3D registration result of the CC axis for kV-MV image pairs. Also, the extracted MV motion along x-axis served as a reference and was compared with the 2D-3D registration result of the AP axis for kV-MV image pairs. figure 3.6 shows the results of diaphragm annotated motion from kV image sequence as well as motion extraction in x and y-axis of an MV image sequence.

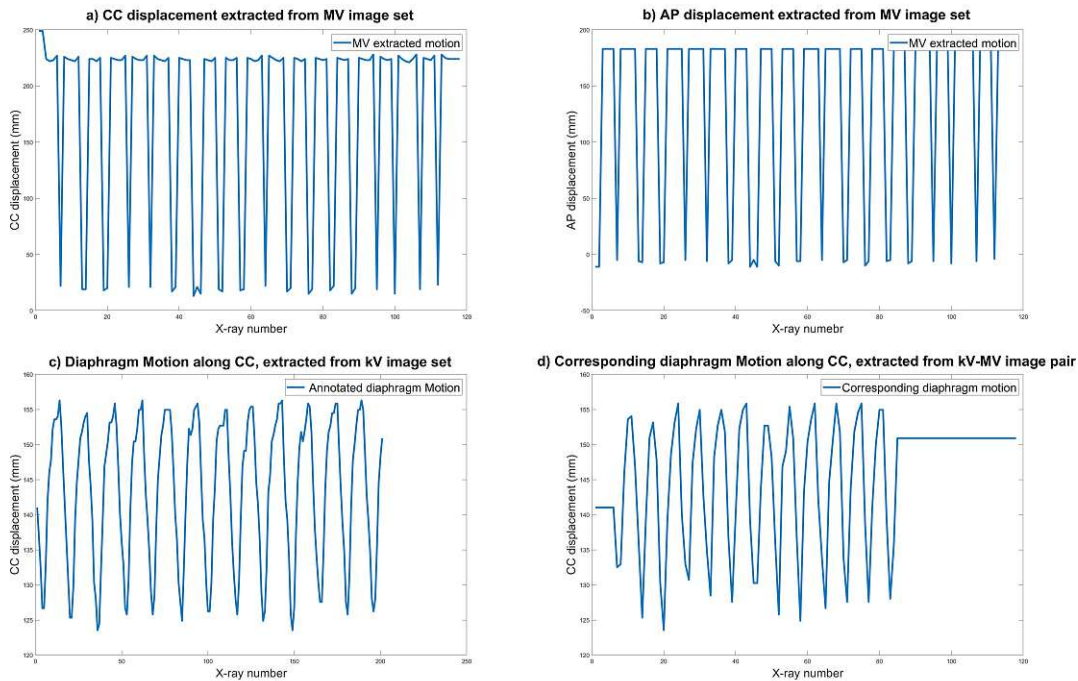


Figure 3.6: Example of motion extraction is shown, for patient 6, Fr.1, g.a. 170°,
a) Extracted motion along CC axis from MV images, b) Extracted motion along AP axis from MV images, c) Diaphragm motion along CC axis extracted from kV images, d) Corresponding diaphragm motion along CC axis for kV-MV image pair

3.3.5 kV - MV Correlation

Ideally, KV and MV images need to be acquired simultaneously. However, as mentioned earlier in this chapter, these were taken at different frame rates resulting in non-synchronized image pairs. Also, the acquisition started manually, which led to a delay in the acquisition start. Therefore, a correlation of the kV-MV pairs was needed to align the gathered image sets in time. This correlation would not be needed if the images were acquired at the same time.

To correlate kV-MV images, the results of the diaphragm motion extraction from kV images were used to find the time in which the two motion signals correlated the best. The images were acquired with different frequencies (kV at $5.47Hz$, MV at $2.16Hz$, a constant ratio of $\sim 2,52$). MV image set had fewer x-ray images but was acquired in a longer duration compared to kV images. As a result, the signal of the MV-set was interpolated based on the sample rate difference and then downsampled. The cross-correlation of the two signals was maximum at a lag equal to the delay. So the delay was calculated by finding the maximum point of the cross correlation function between the signals. Then knowing the delay, aligned kV images were calculated, and then each MV-image was paired with the kV-image with the least lag to it. These steps were done sequentially with the help of *interp*, *downsample*, and *xcorr* functions in Matlab. As shown in figure 3.7, interpolated EPID in red with lower frequency last longer than the kV images in blue. Moreover, the timing of aligned kV and MV images, as well as corresponding image pairs is shown. In most cases, the number of MV images, for which corresponding kV images were acquired was around 70. The other remaining MV images were paired with the same last corresponding kV image, meaning that the kV images stood still after that time. Therefore the relevant period of the batch registration, where both images showed movements, was considered separately because the registration was also performed on the remaining MV images.

Performing the cross correlation provided corresponding kV-images, used later in 2d-3D registration of kV-MV image pair, as well the new corresponding diaphragm motion from corresponding kV images used as a reference for registration result of kV-MV image pair. As shown in figure 3.7, the kV-MV pair sequence were used to visually check if the kV-MV images were correctly aligned for the whole set of the image pair. In cases where kV and MV image sequences could not be aligned, performing the 2D-3D registration would be unnecessary, and leading to the wrong results.

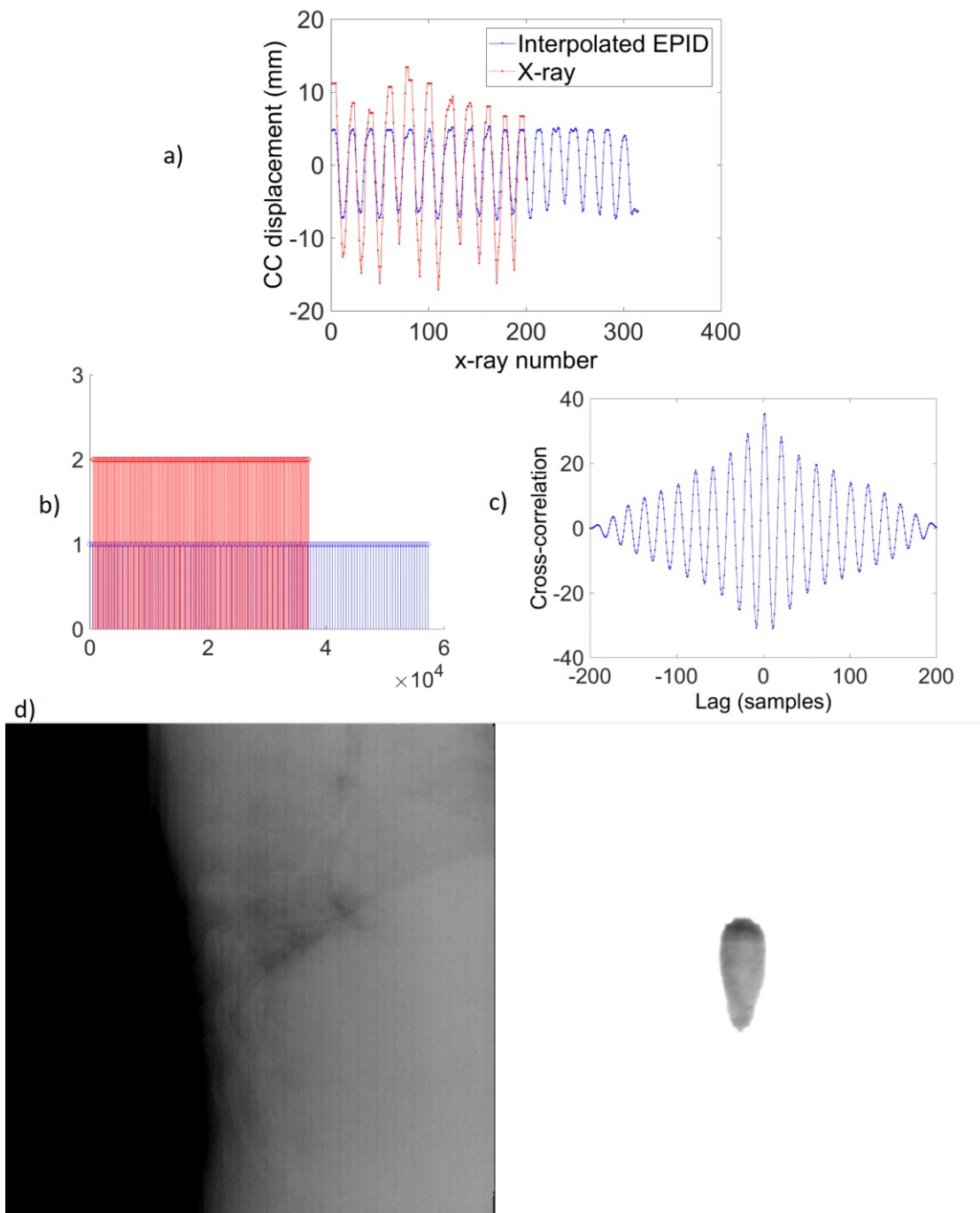


Figure 3.7: The process of kV-MV image pair alignment shown for patient 9, Fr.3, g.a. 170°: a) plot of kV and interpolated MV motion signals, b) timing display of aligned kV versus MV images, c) cross correlation between the two signals, d) example of a kV-MV image pair

3.4 2D - 3D Registration

The aim of the 2D-3D registration with FIRE was to find the volumetric transformation T from one X-ray image to the subsequent that describes the translational and rotational tumor shift the best. FIRE had three tabs to be adjusted. The *configuration tab*, as shown in figure 3.8, where the initial configuration such as Rendering, Merit function, and Optimizers were selected. In this evaluation, the five introduced computationally efficient merit functions were available: mutual information, cross Correlation, correlation ratio, rank correlation, and pattern intensity. As for the optimizer, Simplex, Conjugated gradient, and Powell were available for different DOF. After trying all different merits, it was clear that *mutual information* and *cross-correlation* performed better for this study, with cross-correlation outperforming mutual information and more suitable for noisier results. As a result, cast Rendering for DRR generation, and mutual information, as well as cross-correlation were chosen as merit functions. For optimizers, *Powel 5DOF* for the kV image set and *Powel* for kV-MV image pairs were selected.

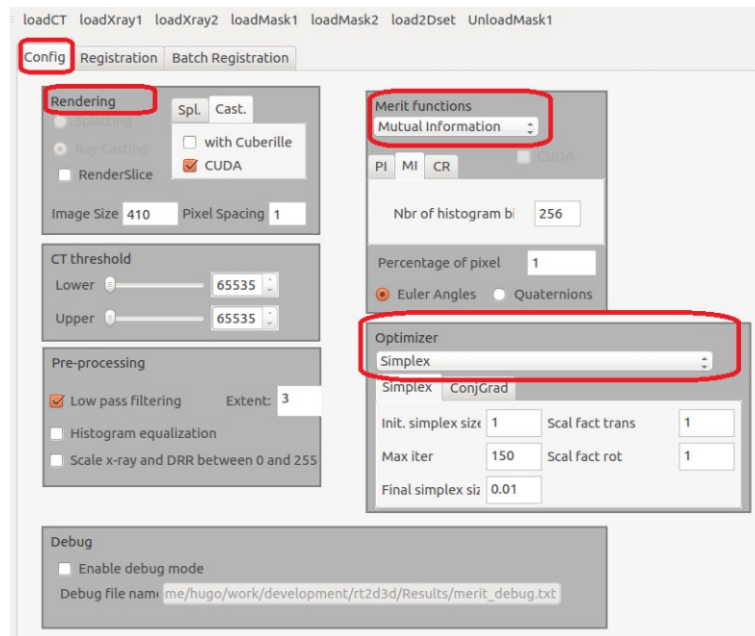


Figure 3.8: FIRE - Configuration tab

In the *registration tab*, there were three main sections to upload the data. As shown in figure 3.9, the first upper and lower section dedicated to DRR showing the same DRR from different angles, the second upper and lower section used for uploading 2D images, and the registration result shown in the upper and lower part of the third section with its parameters at the right bottom part in the provided space for the registration result. The CT volume registered to the daily CBCT was loaded in the upper left section of

the screen. Then one of the significant kV images for the kV set or a corresponding kV images for the kV-MV pair set loaded in the upper-middle section. When the registration involved only the kV images, the lower section would remain empty. Otherwise, this lower middle section contained the matching MV image. Then in the lower-left section of the program, the corresponding CT projection for the MV image was shown. The 3D and 2D images were captured with different energies of the same linac, which resulted in different image intensities. The next step was to adjust the contrast and brightness values of the upper and lower CT projections so that these values match the corresponding ROI in the 2D images to make the process of comparing and finding an initial guess easier. These adjustments were delivered by controllers on the upper left parts of the screen, known as *intensity divider* and *windowing*, resulting in high and low limit values. Everything else beyond this limit is set to black and white.

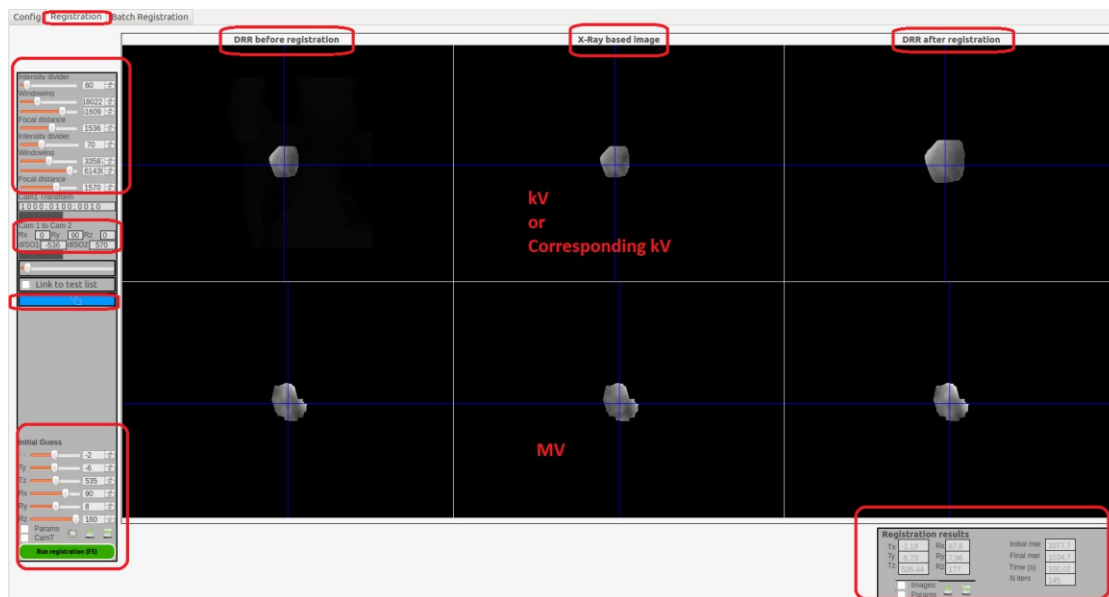


Figure 3.9: FIRE - Registration tab shown for kV images with applied PTV masks for patient 9, Fr.1, g.a. 98°

The focal distance was fixed and set to 1536 mm for kV and 1570 mm for MV set according to the geometry of the treatment LINAC. The geometrical relationship between XVI and EPID was taken into account in the *Set matrix* section. The blue bar showed the number of x-ray images in the displayed image sequence. It was possible to switch between the sequence of images, only keeping in mind that the chosen kV and MV should match. Next, the PTV masks loaded onto the X-ray images delineating the ROI for the registration. The DRRs were only rendered for the ROIs to reduce the computation time. Another advantage of using ROI in place of the whole image was ignoring any significant soft-tissue deformation between the 2D and 3D images, which

could deteriorate registration results or deliver the registration result for something else than the tumor.

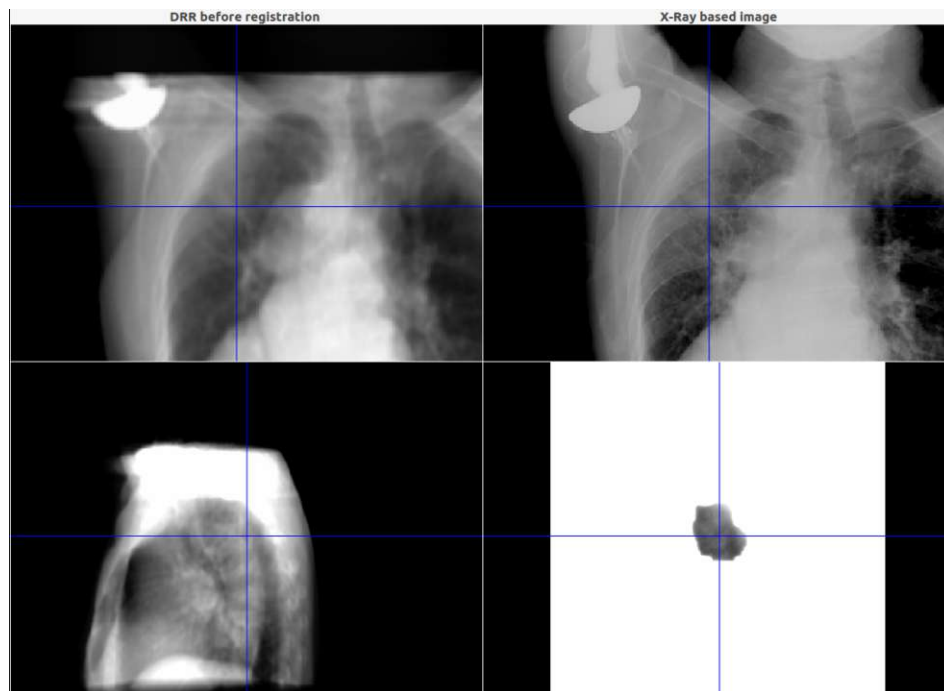


Figure 3.10: FIRE - Registration for corresponding image pair before mask application for patient 9, Fr.1, g.a. 98°

After the upload of volume, images, and PTV masks, the initial guess (IG) had to be defined and entered in the initial guess section on the bottom left side of the window. The initial guess was a guess made manually by the operator of the program to find good initial values for $T = (tx, ty, tz, \omega x, \omega y, \omega z)$ based on one of the uploaded images from the image sequence, with tx, ty, tz being the translation parameters and $\omega x, \omega y, \omega z$ as rotation parameters. Some fixed start values were set according to the geometry of the treatment facility: tz set to 536 mm, which represented the distance of the detector panel of the kV system to the axis of rotation, $\omega x = 90^\circ$, $\omega y =$ as the actual gantry angle between $[0|180^\circ]$ and $\omega z = 180^\circ$. For kV images, tx, ty, tz represented the LR, CC, AP, respectively, while for MV images orthogonal to kV images, tx, ty, tz represented AP, CC, LR, respectively. As a result, when only using one set of kV images, the registration was done with 5DOF as only tx and ty needed adjustment for the relevant gantry angle by comparing the selected kV image with the DRR while tz was constant and set to 536 mm. However, when using both kV and MV image pairs, the registration was done with 6DOF, meaning that tz corresponded to the motion along the LR axis of the orthogonal MV images that should have been adjusted and taken into account. As shown in figure 3.10,

when it was hard to see the tumor in the ROI, the initial guess was chosen without the masks in place and improved later after the masks were uploaded.

As it can be seen in figure 3.11, after the user set the initial parameter, with the *Run Registration* field on the left bottom of the screen, a DRR is rendered with iteratively corrected parameters and then compared to the reference x-ray image until reaching an optimum similarity. The sum is the combined merit value for a particular transformation T and the value that is optimized. Then, the DRRs shifted by the found values of T , could be seen in the two right upper and lower sections. Sometimes the merit value reached a local minimum for an initial guess that was wrong, but it was still possible to visually check and compare the registration result on each image with the real 2D image. The adjusted windowing parameters and the selected initial guess of the whole sequence were saved for later use.

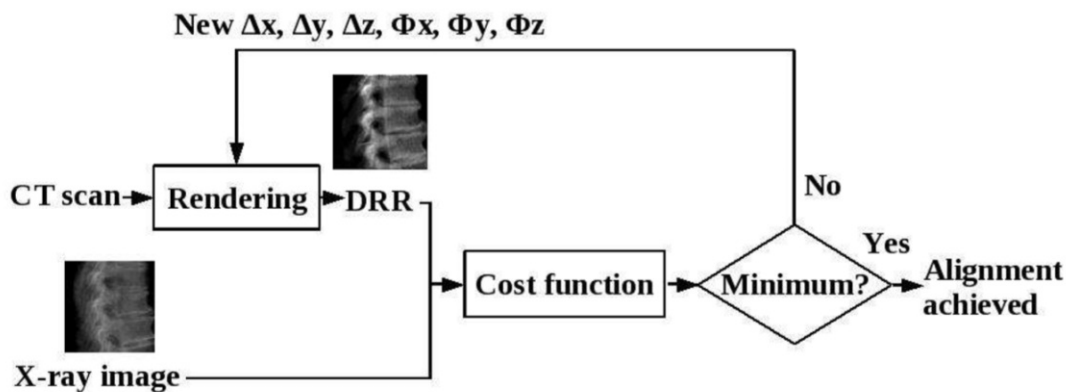


Figure 3.11: Workflow of registration in FIRE. (Figure from [50])

In the tab “Batch Registration” shown in figure 3.12, the registration applied on the whole image sets, and hence, the motion was extracted for the entire duration of kV image acquisition. First the data such as the volume, 2D image sequences, IG, Windowing, and masks were uploaded as separate files, followed by importing the parameters from the previous screen. Before running the test, the paths, file names, and settings entered in the respective fields were selected, with the option of saving the whole configuration for later use.

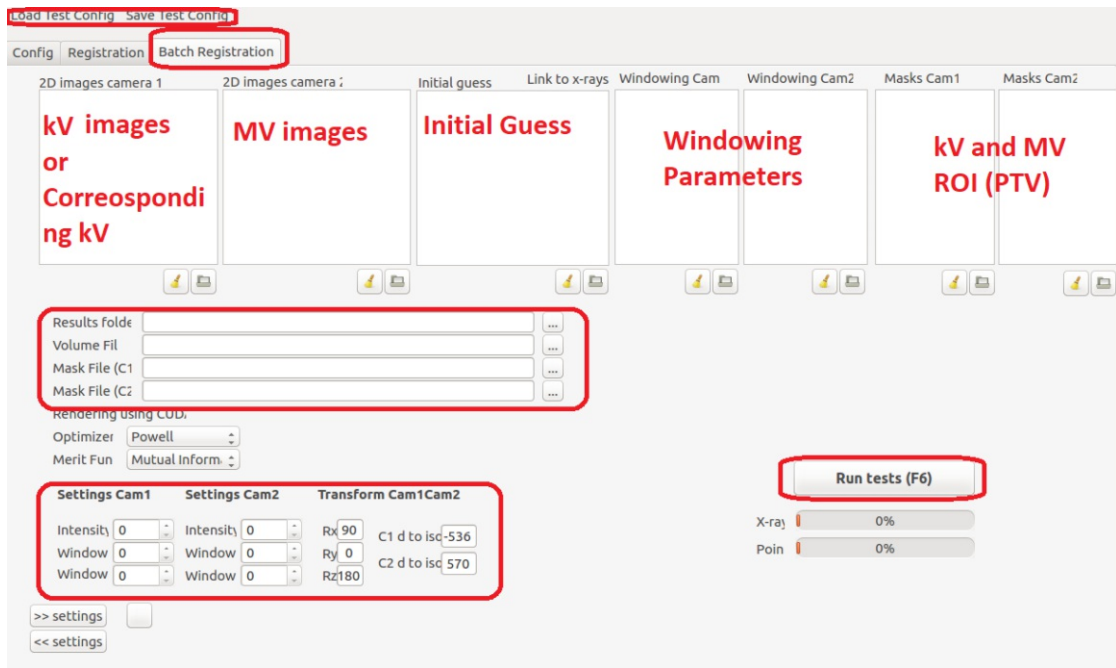


Figure 3.12: FIRE - Batch Registration tab

3.5 Registration Result

The results of the full batch registration were saved to a target folder and represented the actual tumor dislocation from the LINAC isocenter in millimeters and the rotations around the isocenter. After running the registration, FIRE creates three text files *Results*, *Results-logfile*, *Result-times*, as well as the initial DRR image.

- *Result-times* was a vector containing all the registration timing
- *Results-logfile* contained all the configuration, adjustments, and settings
- *Results* represent the actual tumor dislocation with the following values:
Sequence number, T_x , T_y , T_z , ω_x , ω_y , ω_z , Iterations, Rounded registration time, Initial merit, Final merit.

The translational and rotational parameters of registration result with 5DOF and 6DOF for patient 6, Fr.1, g.a. 140° is shown in figure 3.13. Additional MV images resulted in better results for the mutual CC axis while also retrieving motion along the AP axis. With an additional MV image set, the motion along the LR axis and the rotational parameters improved and was not influenced by random errors as earlier.

One of the challenges in this patient study was the lack of a gold standard for motion extraction such as implanted gold markers in the tumor, to compare the registration

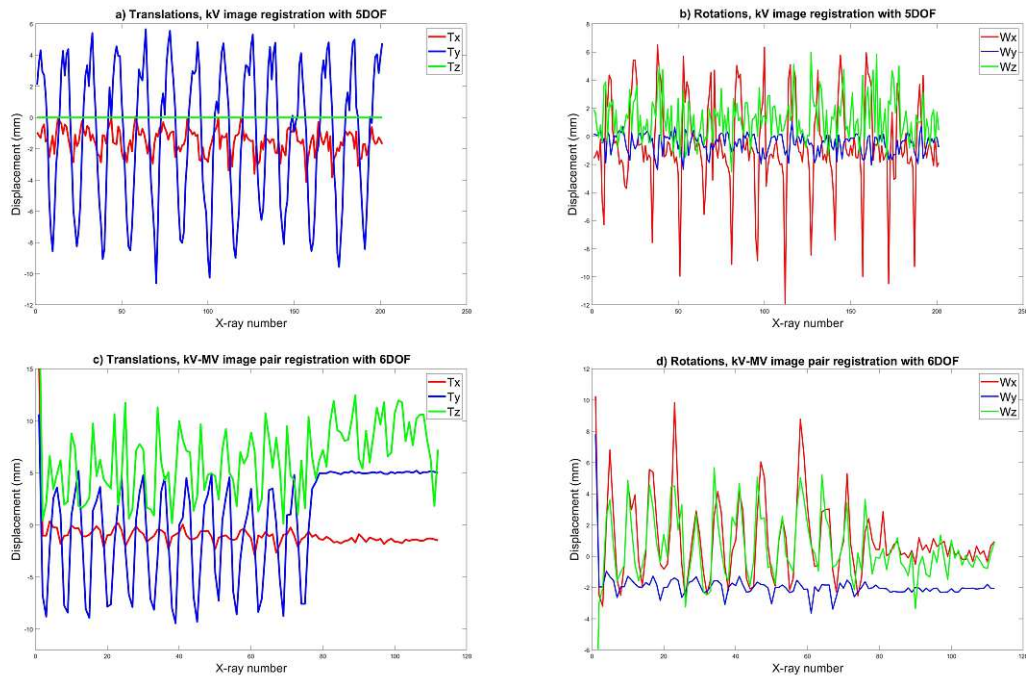


Figure 3.13: Translational and rotational parameters of registration result with 5DOF and 6DOF is shown patient 6, Fr.1, g.a.140°:

- a) translational parameters of 5DOF registration when using kV image set,
- b) rotational parameters of 5DOF registration when using kV image set,
- c) translational parameters of 6DOF registration when using kV-MV image pair,
- d) rotational parameters of 6DOF registration when using kV-MV image pair

results. Moreover, fiducial markers could make it possible to validate rotational parameters, but this study was only limited to the evaluation of translational parameters. However the use of body frame and fixing devices in SBRT limited the rotation of the patients. Because of the lack of gold standard, the motion of surrogate structure was used for validation of the registration result. It is assumed, the tumor motion was correlated to the annotated diaphragm motion, with diaphragm motion being a sinusoidal curve representing the breathing motion. However, this was not true for irregular breathing motion and needed to be checked. A good example was shown in a feasibility patient study [14], with a patient with a tumor motion being in inverse phase to the diaphragm motion.

3.5.1 Qualitative Evaluation of Results

To evaluate the result visually, the registration result and breathing motion were imported to Matlab. All the plotted signals were initially re-scaled by subtraction of their

mean value. Also, the amplitude of the registration result was changed so that it matches the extracted motion amplitude to provide better visualization. The real amplitude values of displacements, are given in tables available in the *Result* chapter. Also, a reversion along the Tz axis because of different motion directions was necessary for better visualization. In summary, for each studied patient, two sets of plots were presented for each fraction with all its gantry angles, which could be found in *Appendix*:

1. The aligned kV-MV image pairs and their lags in cross correlation, plotted to check if the proper correlation between kV-MV exists.
2. The diaphragm motion in CC axis from kV images were plotted against translation along Ty axis from registration results in 5DOF (Left column). The corresponding diaphragm motion in CC axis from kV-MV image pairs were plotted against translation along Ty axis from registration results in 6DOF (Middle column). The extracted motion in RL axis from MV images was plotted against reversed translation along Tz axis from registration results in 6DOF (Right column).

3.5.2 Quantitative Evaluation of Results

To numerically evaluate if the extracted motion signals and registration results match, different possibilities exist. The signals could be brought to the Fourier domain or just compared in the time domain with a correlation coefficient or Root Mean Square Error (RMSE). For this study, *corrcoef* function in Matlab was chosen to obtain the Pearson correlation coefficient, $[R, P] = \text{corrcoef}()$

R and P are both 2-by-2 symmetric matrix with ρ (pearson correlation coefficient) and P-Value is the off-diagonal element of the R and P matrix, respectively. ρ values could range from -1 to 1 , with -1 representing a direct, negative correlation, 0 showing no correlation, and 1 representing a direct, positive correlation.

$$\rho(A, B) = \frac{1}{N-1} \sum_{i=1}^N \left(\frac{\bar{A}_i - \mu_A}{\sigma_A} \right) \left(\frac{B_i - \mu_B}{\sigma_B} \right) \quad (3.2)$$

Where μ_A and σ_A are the mean and standard deviation of A and respectively the same for B . On the other hand, P values range from 0 to 1 , where the values close to 0 correspond to a significant correlation in R and a low probability of observing the null hypothesis. The null hypothesis assumes no relationship between the tested signals. For P-values smaller than the significance level (with 0.05 as the default), the corresponding correlation in R is considered significant.[2]

4 Results

The ρ - correlation coefficients and the corresponding P-values for each plot comparison, as well as the displacement amplitudes for the registration results and extracted motions after the mean subtraction, are presented in this chapter. The first three MV images encompassed no relevant structure and hence, were excluded. For a meaningful comparison of correlation coefficient, as well as the plots of a specific gantry angle, the same number of x-ray images were chosen. This image sequence was chosen based on the available number of kV-MV image pairs and taken into account for all plots, correlation coefficient calculation, and displacement amplitude calculation. For a visual inspection, all the plots could be found in *Appendix*.

Table 4.2: Patient 5 Summary of Results

Magenta_ Displacement amplitude, ρ -Correlation Coefficient, and P-Values for registration result and diaphragm motion along Ty in 5DOF using kV images
 Blue_ Displacement amplitude, ρ -Correlation Coefficient, and P-Values for registration result and extracted motion along Ty in 6DOF using kV-MV image pairs
 Green_ Displacement amplitude, ρ -Correlation Coefficient, and P-Values for registration result and extracted motion along Tz in 6DOF using kV-MV image pairs

		12°		40°		80°		120°		150°		180°		205°			
		ρ -value	P-Value	Registration-amplitude(mm)	Motion-amplitude(mm)	ρ -value	P-Value	Registration-amplitude(mm)	Motion-amplitude(mm)	ρ -value	P-Value	Registration-amplitude(mm)	Motion-amplitude(mm)	ρ -value	P-Value	Registration-amplitude(mm)	Motion-amplitude(mm)
kV (CC)	Fr-1	0.67	0.00	2	14	0.95	0.00	4	26	0.58	0.00	2	15	0.70	0.00	2	17
	Fr-2	0.41	0.02	3	21	0.57	0.00	2	18	0.41	0.00	1	13	0.70	0.00	2	35
	Fr-3	0.84	0.00	4	15	0.87	0.00	2	13	0.67	0.00	2	9	0.80	0.00	2	35
KV-MV (CC)	Fr-1	0.78	0.00	1	17	0.85	0.00	3	20	0.41	0.00	2	15	0.87	0.00	2	17
	Fr-2	0.56	0.00	3	21	0.74	0.00	2	20	0.44	0.00	2	13	0.80	0.00	2	40
	Fr-3	0.74	0.00	2	17	0.83	0.00	2	15	0.59	0.00	2	11	0.86	0.00	2	33
KV-MV (AP)	Fr-1	-0.17	0.34	1	2	-0.69	0.00	3	2	-0.58	0.00	2	2	-0.83	0.00	1	1
	Fr-2	-0.24	0.18	8	1	-0.92	0.00	4	3	-0.71	0.00	4	2	-0.81	0.00	1	1
	Fr-3	-0.66	0.00	1	3	-0.86	0.00	3	3	-0.80	0.00	2	3	-0.84	0.00	2	1
kV (CC)	Fr-1	0.70	0.00	1	17	0.70	0.00	2	15	0.58	0.00	2	15	0.70	0.00	2	17
	Fr-2	-0.27	0.03	2	13	0.41	0.00	1	13	0.41	0.00	1	13	0.70	0.00	2	35
	Fr-3	0.44	0.00	2	11	0.67	0.00	2	9	0.67	0.00	2	9	0.80	0.00	2	35
KV-MV (CC)	Fr-1	0.72	0.00	2	17	0.41	0.00	2	15	0.41	0.00	2	15	0.87	0.00	2	17
	Fr-2	0.13	0.28	2	14	0.44	0.00	2	13	0.44	0.00	2	13	0.80	0.00	2	40
	Fr-3	0.68	0.00	2	13	0.59	0.00	2	11	0.59	0.00	2	11	0.86	0.00	2	33
KV-MV (AP)	Fr-1	-0.85	0.00	6	3	-0.58	0.00	2	2	-0.58	0.00	2	2	-0.83	0.00	1	1
	Fr-2	-0.92	0.00	6	4	-0.71	0.00	4	2	-0.71	0.00	4	2	-0.81	0.00	1	1
	Fr-3	-0.86	0.00	7	5	-0.80	0.00	2	3	-0.80	0.00	2	3	-0.84	0.00	2	1
kV (CC)	Fr-1	0.83	0.00	2	17	0.83	0.00	2	17	0.70	0.00	2	17	0.70	0.00	2	17
	Fr-2	0.70	0.00	3	13	0.70	0.00	2	13	0.70	0.00	2	13	0.70	0.00	2	13
	Fr-3	0.77	0.00	3	17	0.77	0.00	3	17	0.77	0.00	3	17	0.77	0.00	3	17
KV-MV (CC)	Fr-1	0.77	0.00	3	17	0.77	0.00	3	17	0.77	0.00	3	17	0.77	0.00	3	17
	Fr-2	0.82	0.00	4	16	0.82	0.00	4	16	0.82	0.00	4	16	0.82	0.00	4	16
	Fr-3	0.50	0.00	7	2	0.50	0.00	7	2	0.50	0.00	7	2	0.50	0.00	7	2
KV-MV (AP)	Fr-1	-0.50	0.00	7	2	-0.50	0.00	7	2	-0.50	0.00	7	2	-0.50	0.00	7	2
	Fr-2	-0.62	0.00	7	3	-0.62	0.00	7	3	-0.62	0.00	7	3	-0.62	0.00	7	3
	Fr-3	-0.62	0.00	7	3	-0.62	0.00	7	3	-0.62	0.00	7	3	-0.62	0.00	7	3
kV (CC)	Fr-1	0.66	0.00	2	15	0.66	0.00	2	15	0.66	0.00	2	15	0.66	0.00	2	15
	Fr-2	-0.35	0.05	7	13	-0.35	0.05	7	13	-0.35	0.05	7	13	-0.35	0.05	7	13
	Fr-3	0.91	0.00	3	13	0.91	0.00	3	13	0.91	0.00	3	13	0.91	0.00	3	13
KV-MV (CC)	Fr-1	0.75	0.00	2	17	0.75	0.00	2	17	0.75	0.00	2	17	0.75	0.00	2	17
	Fr-2	0.59	0.00	1	13	0.59	0.00	1	13	0.59	0.00	1	13	0.59	0.00	1	13
	Fr-3	0.37	0.04	2	13	0.37	0.04	2	13	0.37	0.04	2	13	0.37	0.04	2	13
KV-MV (AP)	Fr-1	-0.46	0.01	1	2	-0.46	0.01	1	2	-0.46	0.01	1	2	-0.46	0.01	1	2
	Fr-2	-0.81	0.00	2	3	-0.81	0.00	2	3	-0.81	0.00	2	3	-0.81	0.00	2	3
	Fr-3	-0.66	0.00	2	2	-0.66	0.00	2	2	-0.66	0.00	2	2	-0.66	0.00	2	2

Table 4.4: Patient 9 Summary of Results

Magenta_ Displacement amplitude, ρ -Correlation Coefficient, and P-Values for registration result and diaphragm motion along Ty in 5DOF using kV images
 Blue_ Displacement amplitude, ρ -Correlation Coefficient, and P-Values for registration result and extracted motion along Ty in 6DOF using kV-MV image pairs
 Green_ Displacement amplitude, ρ -Correlation Coefficient, and P-Values for registration result and extracted motion along Tz in 6DOF using kV-MV image pairs

35°			80°		
kV (CC)	Registration-amplitude(mm)	Motion-amplitude(mm)	kV (CC)	Registration-amplitude(mm)	Motion-amplitude(mm)
Fr-1	0.79	17	Fr-1	0.59	17
Fr-2	0.55	16	Fr-2	-0.20	13
Fr-3	0.70	15	Fr-3	0.35	11
KV-MV (CC)			KV-MV (CC)		
Fr-1	0.72	21	Fr-1	0.57	17
Fr-2	0.62	20	Fr-2	0.81	19
Fr-3	0.74	15	Fr-3	0.82	15
KV-MV (AP)			KV-MV (AP)		
Fr-1	0.07	2	Fr-1	-0.52	1
Fr-2	-0.50	10	Fr-2	-0.73	1
Fr-3	0.11	7	Fr-3	-0.33	1
110°			140°		
kV (CC)	Registration-amplitude(mm)	Motion-amplitude(mm)	kV (CC)	Registration-amplitude(mm)	Motion-amplitude(mm)
Fr-1	0.58	16	Fr-1	0.98	18
Fr-2	0.56	14	Fr-2	0.90	13
Fr-3	0.63	16	Fr-3	0.82	27
KV-MV (CC)			KV-MV (CC)		
Fr-1	0.93	22	Fr-1	0.89	18
Fr-2	0.97	16	Fr-2	0.94	18
Fr-3	0.88	18	Fr-3	0.88	25
KV-MV (AP)			KV-MV (AP)		
Fr-1	-0.69	5	Fr-1	-0.53	2
Fr-2	-0.52	6	Fr-2	-0.65	3
Fr-3	-0.47	4	Fr-3	-0.15	2
170°			200°		
kV (CC)	Registration-amplitude(mm)	Motion-amplitude(mm)	kV (CC)	Registration-amplitude(mm)	Motion-amplitude(mm)
Fr-1	0.40	27	Fr-1	0.86	24
Fr-2	0.75	31	Fr-2	0.83	22
Fr-3	0.79	30	Fr-3	0.60	26
KV-MV (CC)			KV-MV (CC)		
Fr-1	0.69	30	Fr-1	0.60	26
Fr-2	0.72	37	Fr-2	0.60	26
Fr-3	0.79	30	Fr-3	-0.27	4
KV-MV (AP)			KV-MV (AP)		
Fr-1	-0.62	3	Fr-1	-0.18	3
Fr-2	-0.33	2	Fr-2	0.02	4
Fr-3	-0.38	6	Fr-3	0.14	3
230°					
kV (CC)	Registration-amplitude(mm)	Motion-amplitude(mm)	kV (CC)	Registration-amplitude(mm)	Motion-amplitude(mm)
Fr-1	0.94	18	Fr-1	0.86	24
Fr-2	0.85	21	Fr-2	0.83	22
Fr-3	0.82	22	Fr-3	0.60	26
KV-MV (CC)			KV-MV (CC)		
Fr-1	0.82	22	Fr-1	0.60	26
Fr-2	0.66	21	Fr-2	-0.27	4
Fr-3	-0.47	2	Fr-3	0.14	3
KV-MV (AP)			KV-MV (AP)		
Fr-1	-0.80	5	Fr-1	0.02	4
Fr-2			Fr-2		
Fr-3			Fr-3		

Table 4.5: Patient 12 Summary of Results

Blue _ Displacement amplitude, ρ -Correlation Coefficient, and P-Values for registration result and diaphragm motion along T_y in 5DOF using kV images
Magenta _ Displacement amplitude, ρ -Correlation Coefficient, and P-Values for registration result and extracted motion along T_y in 6DOF using kV-MV image pairs
Green _ Displacement amplitude, ρ -Correlation Coefficient, and P-Values for registration result and extracted motion along T_z in 6DOF using kV-MV image pairs

5°		40°		205°		240°		280°		310°		340°			
kV (CC)	P-Value	Registration-amplitude(mm)	Motion-amplitude(mm)	kV (CC)	P-Value	Registration-amplitude(mm)	Motion-amplitude(mm)	kV (CC)	P-Value	Registration-amplitude(mm)	Motion-amplitude(mm)	kV (CC)	P-Value	Registration-amplitude(mm)	Motion-amplitude(mm)
Fr-1	0.47	0.00	26	14	Fr-1	0.64	0.00	3	13	Fr-1	0.89	0.00	7	24	Diaphragm
Fr-2	0.32	0.00	13	21	Fr-2	0.64	0.00	3	23	Fr-2	0.81	0.00	8	24	Diaphragm
Fr-3	0.68	0.00	12	19	Fr-3	0.58	0.00	2	20	Fr-3	0.77	0.00	7	25	Diaphragm
KV-MV (CC)		KV-MV (CC)		KV-MV (CC)		KV-MV (CC)		KV-MV (CC)		KV-MV (CC)		KV-MV (CC)		KV-MV (CC)	
Fr-1	0.65	0.00	5	16	Fr-1	0.83	0.00	9	22	Fr-1	0.91	0.00	7	24	Tumor(CC)
Fr-2	0.80	0.00	4	22	Fr-2	0.73	0.00	4	25	Fr-2	0.86	0.00	4	24	Tumor(CC)
Fr-3	0.69	0.00	6	20	Fr-3	0.70	0.00	5	19	Fr-3	0.86	0.00	3	24	Tumor(CC)
KV-MV (AP)		KV-MV (AP)		KV-MV (AP)		KV-MV (AP)		KV-MV (AP)		KV-MV (AP)		KV-MV (AP)		KV-MV (AP)	
Fr-1	-0.47	0.00	15	2	Fr-1	-0.72	0.00	23	3	Fr-1	-0.59	0.00	7	3	Tumor(AP)
Fr-2	-0.17	0.00	15	1	Fr-2	-0.61	0.00	22	12	Fr-2	-0.76	0.00	8	3	Tumor(AP)
Fr-3	-0.64	0.00	8	6	Fr-3	-0.53	0.00	22	11	Fr-3	-0.62	0.00	10	27	Tumor(AP)
205°		280°		310°		340°									
kV (CC)	P-Value	Registration-amplitude(mm)	Motion-amplitude(mm)	kV (CC)	P-Value	Registration-amplitude(mm)	Motion-amplitude(mm)	kV (CC)	P-Value	Registration-amplitude(mm)	Motion-amplitude(mm)	kV (CC)	P-Value	Registration-amplitude(mm)	Motion-amplitude(mm)
Fr-1	0.68	0.00	7	21	Fr-1	0.92	0.00	4	16	Fr-1	-0.79	0.00	10	18	Diaphragm
Fr-2	0.64	0.00	3	23	Fr-2	0.94	0.00	4	17	Fr-2	0.59	0.00	6	14	Diaphragm
Fr-3	0.58	0.00	2	20	Fr-3	0.91	0.00	4	20	Fr-3	0.72	0.00	14	25	Diaphragm
KV-MV (CC)		KV-MV (CC)		KV-MV (CC)		KV-MV (CC)		KV-MV (CC)		KV-MV (CC)		KV-MV (CC)		KV-MV (CC)	
Fr-1	0.83	0.00	9	22	Fr-1	0.78	0.00	6	17	Fr-1	0.61	0.00	8	19	Tumor(CC)
Fr-2	0.73	0.00	4	25	Fr-2	0.83	0.00	4	18	Fr-2	0.54	0.00	4	15	Tumor(CC)
Fr-3	0.70	0.00	5	19	Fr-3	0.93	0.00	5	20	Fr-3	0.52	0.00	6	23	Tumor(CC)
KV-MV (AP)		KV-MV (AP)		KV-MV (AP)		KV-MV (AP)		KV-MV (AP)		KV-MV (AP)		KV-MV (AP)		KV-MV (AP)	
Fr-1	-0.22	0.05	30	2	Fr-1	-0.22	0.05	30	2	Fr-1	-0.23	0.05	21	5	Tumor(AP)
Fr-2	-0.59	0.00	9	6	Fr-2	-0.59	0.00	9	6	Fr-2	-0.15	0.21	10	3	Tumor(AP)
Fr-3	-0.06	0.62	8	26	Fr-3	-0.06	0.62	8	26	Fr-3	-0.20	0.10	14	3	Tumor(AP)
340°															
kV (CC)	P-Value	Registration-amplitude(mm)	Motion-amplitude(mm)	kV (CC)	P-Value	Registration-amplitude(mm)	Motion-amplitude(mm)	kV (CC)	P-Value	Registration-amplitude(mm)	Motion-amplitude(mm)	kV (CC)	P-Value	Registration-amplitude(mm)	Motion-amplitude(mm)
Fr-1	0.31	0.01	6	14	Fr-1	0.31	0.01	6	14	Fr-1	0.31	0.01	6	14	Diaphragm
Fr-2	0.53	0.00	15	21	Fr-2	0.53	0.00	15	21	Fr-2	0.53	0.00	15	21	Diaphragm
Fr-3	0.45	0.00	7	28	Fr-3	0.45	0.00	7	28	Fr-3	0.45	0.00	7	28	Diaphragm
KV-MV (CC)		KV-MV (CC)		KV-MV (CC)		KV-MV (CC)		KV-MV (CC)		KV-MV (CC)		KV-MV (CC)		KV-MV (CC)	
Fr-1	0.84	0.00	7	17	Fr-1	0.84	0.00	7	17	Fr-1	0.84	0.00	7	17	Tumor(CC)
Fr-2	0.86	0.00	6	26	Fr-2	0.86	0.00	6	26	Fr-2	0.86	0.00	6	26	Tumor(CC)
Fr-3	0.89	0.00	3	28	Fr-3	0.89	0.00	3	28	Fr-3	0.89	0.00	3	28	Tumor(CC)
KV-MV (AP)		KV-MV (AP)		KV-MV (AP)		KV-MV (AP)		KV-MV (AP)		KV-MV (AP)		KV-MV (AP)		KV-MV (AP)	
Fr-1	-0.61	0.00	6	3	Fr-1	-0.61	0.00	6	3	Fr-1	-0.61	0.00	6	3	Tumor(AP)
Fr-2	-0.62	0.00	8	6	Fr-2	-0.62	0.00	8	6	Fr-2	-0.62	0.00	8	6	Tumor(AP)
Fr-3	-0.81	0.00	5	4	Fr-3	-0.81	0.00	5	4	Fr-3	-0.81	0.00	5	4	Tumor(AP)

5 Discussion

Respiratory motion or even heart beat can cause displacement in pulmonary tumor. These intra-fractional tumor motion can cause tumor displacement of up to 5cm. Common practices for lung cancer include use of fiducial markers, external surrogate markers, transponders, modelling and correlation with external motion. In the first chapter different motion management systems and their limitation were discussed. Most accurate available motion management systems need implantation, patient interaction and are dependent on breathing motion pattern. Another approach is real-time tumor motion monitoring using fluoroscopic images acquired with imaging systems mounted on LINAC, allowing patient positioning as well as acquiring orthogonal projections of the tumor during the course of treatment. Additionally, EPID imaging system provide projections of the tumor using the treatment beam with no additional dose to the patient. Intensity-base 2D-3D registration of acquired images with planning CT, offer a real-time approach with a high accuracy. The result of registration could be used to gate LINAC or shift the couch position. This results in reduction of PTV and consequently dose reduction and sparing of healthy tissue.

In this study, the impact of using kV-MV image pair was investigated thoroughly for different gantry angles as well as different motion axis. The same result for the same gantry angle, treated in multiple fractions, was expected. However, a large quantity of influencing parameters resulted in unexpected deviations that violated this assumption. Imaging factors such as intensity configuration, number and quality of x-ray images per fraction, proper correlation of kV-MV image pair, and registration parameters such as choice of the initial guess for registration are among these factors. Other inter and intra-fraction deviations such as difference in tumor displacement amplitude, irregularities in breathing motion, inner changes in anatomical position, or even possible tumor shrinkage are other examples that could lead to a different result for the same gantry angle treated in multiple fractions. Patient 5, Fr.2, g.a.80° was an example of this case. Despite good tumor visibility on the kV and MV images, the registration did not work for motion along CC direction using either kV image set or kV-MV image set. The intensity of the kV images for the mentioned fraction were significantly lower than the other fractions. The underlying reason could be the chosen intensity window for kV images and a poor correlation between the kV-MV image pair at the beginning of the x-ray sequence. Visual check of MV image set showed small tumor displacement with motion along AP axis as the dominant motion direction with higher amplitude of displacement than motion along CC axis. The visual check explained a better correlation coefficient for AP motion than the CC direction for all fractions. Another possible cause for variation of results from

different treatment fractions is that the 3D-3D registration of pre-treatment CT and CBCT was performed only for one fraction. According to the treatment routine, daily CBCT needed for each treatment fraction and as a result, pre-treatment CT could have been registered to CBCT of each fraction separately, resulting in a more precise volume for DRR generation. However, the volumes per treatment session, investigated in this study, did not drift more than a few millimeters.

To interpret the results, first, it was checked if the calculated correlation coefficients corresponded to our visual inspection of the plots. Then by reviewing the values of the correlation coefficient, the gantry angles with correlation coefficients lower than 0.5 in more than one fraction, were investigated. Only a few gantry angles had a low correlation coefficient for registration results along the CC axis using only kV images, such as patient 2, Fr.2 and 3, g.a.58°. After visual inspection of kV images, it was clear that kV images lacked tumor visibility in that specific gantry angle. All other similar cases of unsatisfactory registration in 5DOF had a lack of tumor visibility in common. For registration results along the CC axis in 6DOF using the kV-MV image pair, all the registration results were successful for at least two fractions of treatment. The only exception was patient 5, g.a.120°, with correlation coefficients around 0.5 even though the tumor was visible in both kV and MV image sets. After trying multiple initial guesses and different intensity windows, the registration result was still not improved. A possible reason for that could be the small range of motion displacement and the existence of a high intensity structure with more motion in the background of the MV image, as seen in figure 5.1. The DRR was intensity scaled to achieve a less highlighted contrast, or else other anatomical structures, instead of the tumor motion, were followed. The existence of structures with very high or low intensity in the ROI, such as this example, could result in failed registration or motion monitoring of different structures than the tumor. Particularly, when the motion of the followed structure and the tumor are not correlated, this could be an issue. The reason for this assumption is that, in earlier phantom studies, using FIRE for registration, with the ribs within the ROI, the rib's motion was followed instead.[33] A possibility of segmentation and removal of specific structures laying within the ROI, might be a solution for such cases.

Tumor characteristic

In earlier studies only specific gantry angles were investigated. [20, 21] In this study, the patient data with a large range of gantry angles chosen to investigate at which angles the registration could work. The registration was successful for 2-7 of gantry angle per fraction with a better success for registration along CC axis. Patient 2, g.a. 160° with data available for only two fractions is the only gantry angle with failed registration for all fractions, with correlation coefficients below 0.5. However, it is a predictable result as the tumor was not visible in either kV images or kV-MV image pairs. For the other investigated gantry angles, some tumor visibility was in place for at least one set of x-ray images, demonstrating that the registration outcome for different gantry angles is

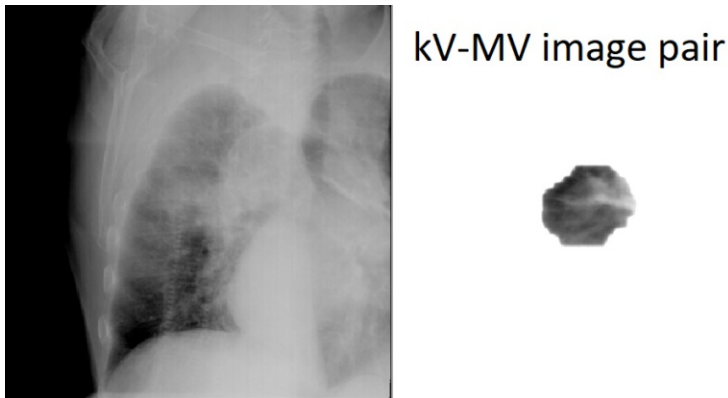


Figure 5.1: kV-MV image pair for patient 5, Fr.2, g.a.120°

heavily dependent on the tumor position. As a result, it might be possible to define a particular range of gantry angles with expected successful registration results with respect to the tumor position. In another patient study for image-pair registration in 6DOF [14], registration along the CC axis failed for 60° and 150° for a patient, while in this study, kV-MV image pair registration along the CC axis works nicely for the same angles for Patient 2, 58°, and Patient 5, 150°. The reason is that the tumor for Patient 2 and Patient 5 were positioned in a cranial, lateral part of the lung, providing distinct tumor visibility, while for the patient in the other study, the tumor was located in an almost medial, caudal position and often covered by other tissues. Another example is 270° with failed registration for a patient with a caudal lateral tumor position versus patient 12, 280° with a successful registration for an almost central-positioned tumor.

After checking the tumor motion trajectory in the MV image set, it was clear that tumor motion followed a diagonal line in most cases with more vivid displacement along the CC axis. In patient 5, the CC displacement was small, with a pronounced mediolateral motion. Hysteresis observed in patient 12 showed an almost elliptical trajectory for the tumor motion at few gantry angles such as 280°, 310°, and 340°. Motion extraction from MV images and correlation of kV-MV image pair was challenging in these cases. Especially, registration result along AP axis was more sensitive to more complicated motion trajectory and failed to provide satisfactory registration result along AP axis when accompanied by a lack of tumor visibility. In this study and based on earlier studies of the same patient data, it is assumed that tumor and structures within the ROI have rigid structure, and no tissue deformation exists in the ROI. As a result, rigid registration was applied. If this does not hold, then a non-rigid registration algorithm is required. However, no noticeable deformation was observed (by the user) except for some soft tissues within the ROI for patient 12, FR.1, g.a. 310°. Because of the overlapping structures, it is not clear for the user; if the observed changes are the deformation within the ROI or the result of a more complex motion trajectory.

Number of x-ray images

The number of registered x-ray images was limited to the number of acquired kV-MV image pairs, which itself was limited to the number of MV images. All the plotting and calculated correlation coefficients were restricted to this number of x-ray sequence so that the registration results with 5DOF were comparable to the registration result with 6DOF without the number of x-ray images influencing the comparison. The first few x-ray images were excluded from the analysis, because the beam was not on yet. Most fractions involved 70 to 80 kV-MV image pair with patient 5 as an exception, with the fewest kV-MV image pair as low as 35 at some gantry angles. Such cases influenced the finding of corresponding kV-MV pairs, and the obtained plots for aligned kV-MV image pair for patient 5 were sub-optimal, so the kV-MV image pair were inspected visually. The correlated motion between two sets of images was acceptable. Nevertheless, the registration results for patient 5 did not significantly differ from other patients. The gantry angles with 35 image pairs, were specifically checked, and almost all registration was successful with a correlation coefficient of about 0.7. This implied that with half number of the current x-ray sequences, then registration could yield the same result, and the number of images did not influence the success or failure of the registration result.

Tomažević [54] suggested that by using more X-ray images, the statistical power of the merit function increase, and additional images help to overcome the effect of possible outliers and artifacts within the image sequence. These will, in turn, result in a lower probability of optimizer converging at local minima, which is the main reason behind failed registration. However, this was suggested as a result of registration with less than ten x-ray images. Even with such low numbers of x-ray images, Tomažević [54] concluded that the number of X-ray images did not influence the accuracy but the registration robustness. In other words, the proportion of successful registration was higher for a higher number of used x-rays, but the results were not necessarily more accurate.

Configuration parameters

The initial intensity window applied for the kV and MV image sequences, and the intensity window applied later in FIRE to the ROI was another important factor. Improper choice of intensity despite good initial value could result in failed registration. The choice of initial guess by the user is another fundamental factor, which is greatly dependent on the tumor visibility within the ROI and needs practice and gained experience, and many try to get an intuitive sense. Especially because the choice of initial guess sometimes resulted in merit values being lower for wrong shifts, which needed to be checked and corrected by the user.

The registration was performed for the ROI, which corresponds to PTV and EPID masks in here, to reduce the computation burden. The additional option of applying a more inclusive ROI plus segmentation and removal of undesired structures within the ROI might help to improve the registration result for some cases. The disadvantage of extending

the ROI for registration is a longer registration time which is not suitable for real-time clinical registration.

Motion extraction

The lack of ground truth, such as implanted gold markers, makes it hard to validate the obtained results. Also, the evaluation of rotational parameters was not possible without fiducial markers, therefore this study was only limited to the evaluation of translational parameters. As mentioned earlier, manual followup of a specific selected point on the diaphragm resulted in the annotated breathing motion. This process made the annotation and especially the displacement amplitude operator subjective. In some cases, such as patient 5, Fr.1, g.a. 12° , the registration results for the kV image set followed the breathing motion signal with some lag. This lag was the result of the manual annotation and is improvable with a better annotation approach. Other than that, the breathing motions did not always show a regular pattern, as shown in figure 5.2. Changes in amplitude and baseline were visible in many breathing motion signals. This was especially noticeable for patient 5 with different irregularities within the same fraction of treatment, which also highlights the importance and need for real-time tumor monitoring during treatment.

The extracted MV motion signal was used to find the kV-MV image pairs and their corresponding breathing motion signal. Considering the lack of anatomical structure, it was not possible to pick up a point and annotate the motion manually. The chosen ROI for the cross correlation had a large impact on the extracted signal, and each trial led to an almost different extracted signal that needed to be checked. Also, sometimes a different choice of ROI for each axis resulted in a better motion extraction for that specific axis. Another problem was that in some cases, the extracted motion for the same MV image set resulted in the same motion extraction signal but with an opposite phase. This was reflected in the form of a positive and negative value for the corresponding correlation coefficients.

For registration results along the AP axis using the kV-MV image pair, the resulted correlation coefficients were in general smaller than for the correlation coefficients obtained from displacements along the CC axis. One reason was that the CC axis is mostly the dominant motion axis,^[24] however, in patient 5 sometimes AP axis act as the dominant motion direction. It is also important to note that, the tumor in patient 5 was closer to the lung apex than the diaphragm. Another possible reason is that motion extraction on kV images following the diaphragm motion resulted in a more regular breathing motion signal while extracting motion from MV images, was not straightforward. For patient 9, g.a. 200° , and patient 12, g.a. 310° , the registration failed to follow the AP displacement. After a visual inspection, it was clear that MV images for the mentioned angles lacked tumor visibility. However, for the displacement along the CC axis, the available information from the kV image set helped to improve the correlation coefficients up to

0.6. Registration result along the AP axis in 6DOF using kV-MV image pair, were less successful in patient 9, and patient 12, while on the contrary, the registration along CC axis was more satisfactory compared to other patients. This was expected as tumors in diaphragm proximity show more significant craniocaudal movement.

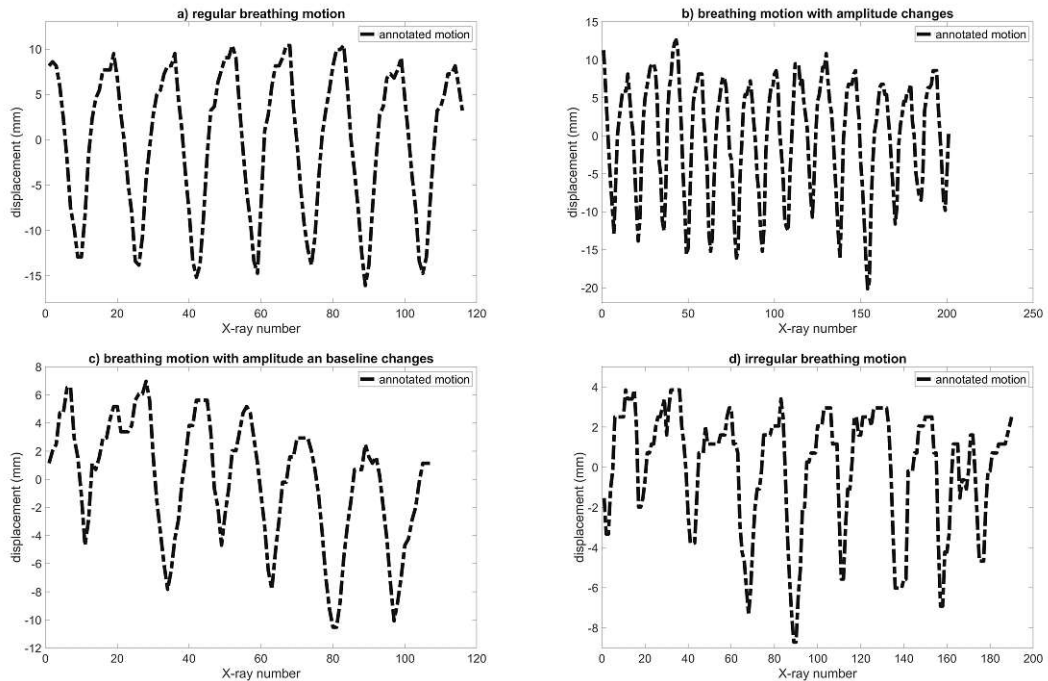


Figure 5.2: Examples of extracted diaphragm motion plotted in dashed black line for the studied patients:

- a) regular breathing motion for patient 6, Fr.1, g.a: 110° , b) regular breathing motion with changes of amplitude for patient 12, Fr.3, g.a: 340° , c) breathing motion with changes in amplitude and baseline for patient 5, Fr.3, g.a: 12° , d) An almost irregular breathing motion with random errors for patient 5, Fr.3, g.a: 80°

A properly aligned kV-MV image pairs were a prerequisite for the success of the registration. Differences of up to 100 ms existed between images. As a result, it is very important that correlating kV and MV image pair process, as shown in figure 3.7, result in accurate corresponding image pair. The lag plots of the image pairs for patient 2 and patient 5 were not as optimal as other patient. The underlying reason for patient 5, was the small amplitude of displacement, and for patient 2, the lack of tumor visibility in some MV image sequences made the process of accurate motion extraction very difficult. Patient 5, Fr.3, g.a. 205° showed the poor result for displacement along the CC axis for registration in 6DOF due to the misaligned image pair. In this case, the MV images showed almost no movement to be extracted by cross-correlation.

Displacement amplitude

The breathing motion could cause tumor displacement up to 5cm. The extent of motion depends on tumor location and relation to bone mediastinum and diaphragm. In this study, the amplitude of investigated breathing motion signals were rounded to its closest integer. The breathing motion amplitude ranged from less than 1mm up to 4cm displacement; with displacement along CC axis having higher amplitude (above 1cm) than displacement along the AP axis, with less than 1cm displacement amplitude. In general, CC is known as the dominant axis of motion for lung tumors, but displacement up to 1.5 cm was observed for the AP axis, acting as the dominant axis of motion. The registration result generally showed lower displacement values for motion along CC axis, mainly below 1.5cm, and higher values of displacement amplitude for motion along AP axis compared to breathing motion signal. Also, the registration results along the CC axis using 5DOF showed slightly higher displacement amplitude compared to the results from registration with 6DOF. The higher amplitude from registration with 5DOF was not often a real representative of the tumor motion but due to random errors. It is important to mention, the choice of merit function for registration influenced the amplitude of displacement. In most cases, registration for the same gantry angle with the same parameters when using cross-correlation as merit function resulted in a lower displacement amplitude compared to mutual information as the merit function. Occasionally the displacement amplitude of the registration result and extracted motion from MV images were correlated with the actual movement seen in the X-ray images but with an exaggerated unrealistic amplitude value. Also, the outlier presence in the sequences, where no tumor visibility was available, influenced the motion amplitude that had to be checked and corrected separately. This issue could be a problem for real-time registration in clinical scenarios.

Patient 9 and patient 12 were expected to show registration results with similar amplitude as breathing motion signals due to their proximity to the diaphragm, but this did not happen. The registration results for patient 2 and patient 5 were less than 1cm irrespective of the direction, whereas the corresponding breathing motions showed higher displacement values within the same range as other studied patients. Consequently, it was observed that the tumor displacement was mostly synced but it was not necessarily in the same range of amplitude as diaphragm motion, even for tumors in the diaphragm proximity. It is expected that registration results work better for larger displacement and our results confirmed this. For tumor motion above 2cm, with tumor visibility in one image set, almost all correlation coefficients were above 0.4. Considering that many configuration parameters could influence the registration result, motion amplitude was not the only factor influencing the correlation coefficients. Reviewing the table summary for each studied patient showed that displacements as low as 1mm for the AP axis, and as low as 9mm could be resolved. For lower motion displacement, the registration results seemed to be more affected by random errors. However, whereas in clinical applications, the importance of tumor motion monitoring would be significant for displacement above 2 cm and for patient with smaller tumor motion displacement, motion monitoring might

not be as compulsive.

Advantage of additional MV image set

Another goal of this study was to evaluate the impact of using an additional MV image set for registration. As mentioned earlier, an advantage of using kV-MV image pair for registration in 6DOF was to resolve motion along the image beam axis, which was not possible in registration with 5DOF. As shown in ??, T_z with a constant flat signal was retrieved only when switching to 6DOF registration with image pairs. The visibility factor of the tumor within the applied PTV and EPID masks was a critical factor for the registration success. As a result, the results were interpreted based on the tumor visibility to evaluate the impact of using an additional MV image set on displacement along the CC axis:

- *Tumor invisible in both orthogonal image sets:*
As mentioned earlier, registration failed when the tumor was distinguishable in neither kV image sequence nor MV image sequence. However, this was rarely the case in the presence of two orthogonal image sets. The main challenge was that sometimes the tumor was fully or partially covered in some image sequences because of the inner anatomical and tissue displacement during treatment, and the ROI on the kV images seemed to be only one continuous white field for the operator, with no contrast. There are examples such as patient 2, g.a.25° and 190°, patient 9, g.a.35°, with the tumor mostly covered and not distinctively visible in both image sets, in which the motion displacement could still successfully get followed. This shows that sometimes it is far from being obvious which data and start parameters could result in a good outcome. The addition of the MV image set, for this cases, has helped to improve the registration result and resulted in better correlation coefficients. Also, the proper choice of intensity window to highlight the tumor visibility was a critical step for registration of these cases.
- *Tumor invisible in kV image set but visible in MV image set*
When the kV image set lacked tumor visibility, the addition of the MV image set was a great help because of the possibility of motion extraction along the mutual CC axis. Patient 12, g.a.205° and 340°, patient 2, g.a.58°, are examples of such cases with improved results for registration in 6DOF. On the contrary, patient 9, g.a.200° and 230° showed better results, for registration in 5DOF versus registration in 6DOF, despite the lack of visibility in the kV image set. As mentioned earlier, this result suggested that registration could work fine even if the ROI on the kV images for the human eye seemed like a continuous white field due to insufficient contrast. Another possible reason for good registration result in 5DOF could be that the registration follows the displacement of another existing pattern or tissue with a distinct contrast within the applied PTV mask. Patient 12, Fr.1, g.a.340° is a good example of this case shown in figure 5.3. The registration result with kV images provides a periodic signal which is not in phase with breathing mo-

tion, whereas additional MV image set offered a registration result synched with breathing motion.

- *Tumor visible in kV image set but invisible in MV image set*

For patient 2 and patient 12 at some gantry angles such as patient 2, g.a.98°, and 130°, the tumor was not visible in MV image sequences. In such cases, when kV images already yield a good result in registration with 5DOF for displacement along the CC axis, the addition of the MV image set did not necessarily improve the result. Displacement along the AP axis could still justify the use of an additional MV image set. However, in such cases, finding a proper configuration and initial guess was not an easy task for the operator and mostly failed to work. It is important to mention that sub-optimal registration in 6DOF could also be the result of improperly aligned kV-MV image pair and not tumor invisibility in MV image data set.

- *Tumor visible in both image sets*

Patient 5 offered examples with tumor visibility in both kV and MV image set, at g.a.80°, 120° and 150°. By reviewing the results for different treatment fractions, it was clear that the addition of MV images resulted in successful motion extraction along the AP axis. Moreover, this helped to improve the failed registration with 5DOF, but on the contrary to what was expected and similar to the previous case, registration with 6DOF did not necessarily outperform the successful optimal registration results with 5DOF. A possible explanation could be that more additional steps and configurations needed for registration with kV-MV image pair. Sub-optimal kV-MV image pair alignment and improper intensity windowing of generated DRR for MV image sequence could result in a less efficient registration compared to registration with the kV image set. A better registration result for the kV-MV image pair was achievable, if the kV and MV image acquisitions were synched.

MV images dominated by Compton scattering and kV images by the photoelectric effect. In general, MV images offer a lower contrast in comparison with kV images. However, the difference in density for lung tissue (around 0.2 gcm^{-3}) and target volume (around 1 gcm^{-3}) still provides an acceptable contrast in MV images. [35] MV images were recorded from the treatment beam, encompassing the tumor with almost no anatomical structure within the image. This contrast made it easier to spot the tumor in MV images at most gantry angles. As a result, in most cases, kV images could benefit from the extra information in the MV image set. As mentioned earlier, after corresponding kV-MV image pairs (at about X-ray number of 70), the extra MV images were paired with the same last corresponding kV images, and the rest of the registration was only the result of the still moving MV images. At this point, it was possible to see a visible change in the registration result. An improvement in the result suggested that an additional MV image set for some patients at specific gantry angles, using only one of the two available image sets could lead to better results. Providing an adjustable weighting factor for the contribution of each image set to the translation matrix in FIRE, leads

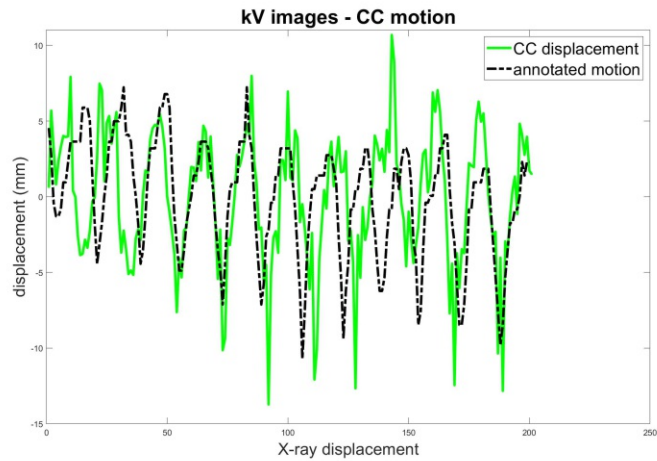


Figure 5.3: CC motion displacement of kV images shown for patient 12, Fr.1, g.a.340°. Despite the fact that Kv images offer no tumor visibility, the registration result (green) shows a motion signal which is not in phase with following the annotated motion (dashed black line).

to an optimal registration results by tackling the issues with assigning lower weighting factor to an image set with less tumor visibility. Especially for the few cases with optimal registration in 5DOF, the addition of the MV image set resulted in a less satisfying registration result along the mutual CC axis. Examples of MV image contribution with high and low weighting factor are suggested in figure 5.4.

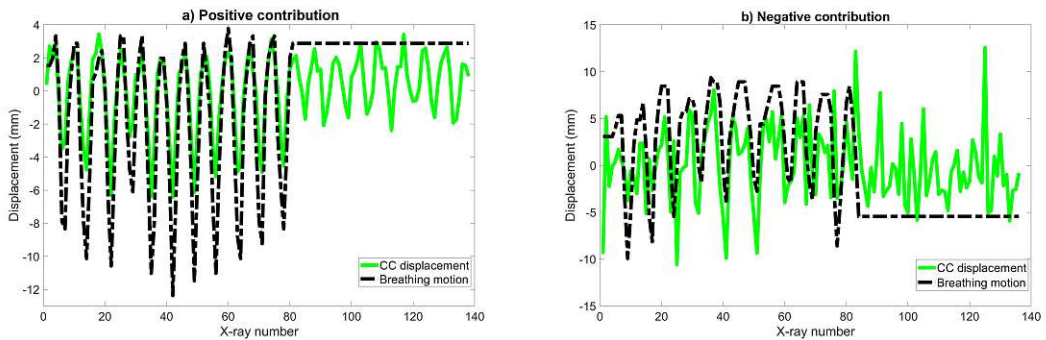


Figure 5.4: Examples of MV image contribution shown with MV motion contribution (green) and breathing motion (black), for registration result with 6DOF; a) Example of high-weight factor of MV contribution for patient 9, Fr.2, g.a.110°, b) Example of a low-weight factor of MV contribution for patient 2, Fr.2, g.a.98°

Choice of merit function

As mentioned earlier, FIRE offers a selection of merit functions and optimization. *Powell* as an optimization algorithm, *mutual information*, and *cross-correlation* were selected as merit functions for this study, as the same configurations of earlier studies. After putting different merit functions into a test, it was clear that the choice of merit function impacts the registration result. The registration results were plotted for both selected merit functions and the those with better performance were chosen and used in the final plots presented in *Appendix* as well as the the correlation coefficient calculation. The merit function chosen for 5DOF registration was not necessarily the same as the one used for 6DOF registration along the CC axis, however, the same merit function used in 6DOF registration along the CC and AP axis. In figure 5.5, registration results from different merit functions were compared for patient 6. Fr1. g.a.110°. The registration results were plotted in real scale but with shifts from the breathing motion to provide better visualization.

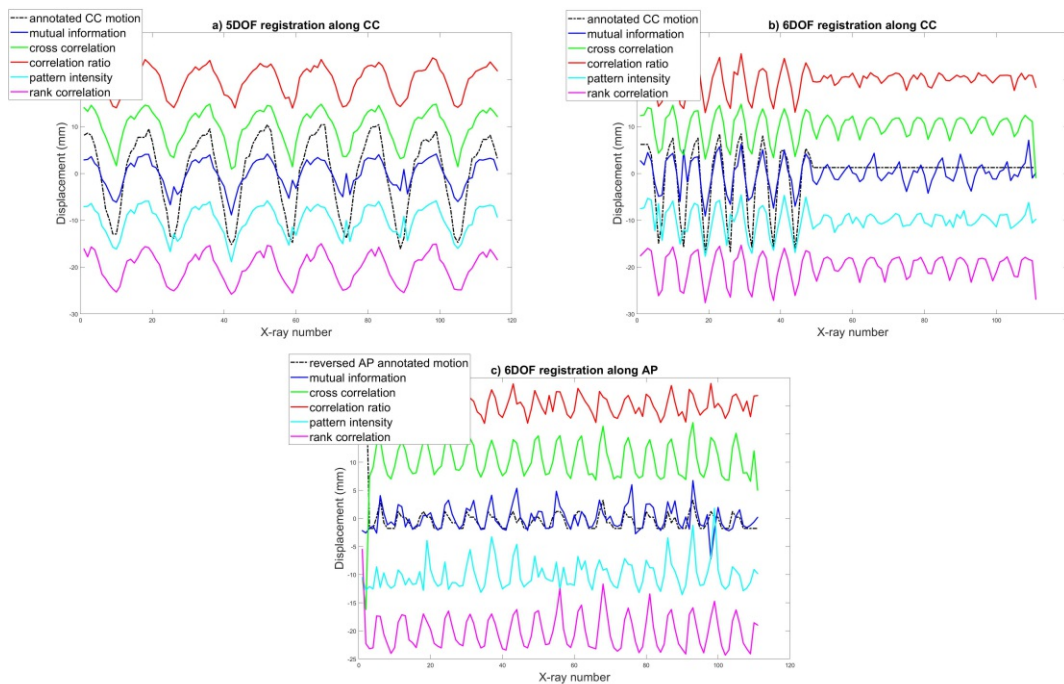


Figure 5.5: Performance of merit function for patient 6, Fr.1, g.a. 110°; The breathing motion is plotted in dashed black line, the result of mutual information in blue, cross-correlation in green, correlation ratio in red, pattern intensity in cyan, and rank correlation in magenta.

- a) 5DOF registration along CC axis,
- b) 6DOF registration along CC axis,
- c) 6DOF registration along AP axis.

In this example, all the tested merit functions resulted in a successful registration with almost the same displacement amplitude. However, during the course of registrations performed for this study, it was observed, the same registration configuration performed with different merit functions could result in registration results with different amplitude of displacement up to centimeters. The plotted results showed that cross-correlation and rank correlation, followed by mutual information, outperformed correlation ratio and pattern intensity. However, these results differ slightly from another comparison of the performance of merit functions in Furtado H [23] with porcine head. In Furtado H [23], mutual information showed a better success rate as well as smaller RMS for 2D-3D registration when using 1-kV, 2-kV, and kV-MV image pair. However, mutual information is outperformed in real patient cases of this study.

Interestingly, registration results along the CC axis, cross-correlation, and rank correlation functioned better for farthest downward displacement, as seen in figure 5.5. After visual inspection of the kV Mv image pair, it was clear that the tumor was covered by some tissues when it was at its lowest position. This means cross-correlation responded the same to different intensity. Cross correlation is known as invariant to global brightness but sensitive to outliers of high intensity, which was not the case in this example.[35]. In practice, it was also clear that cross-correlation was sensitive to extreme high intensity regions existing in ROI. Therefore, choosing cross-correlation and rank correlation as a merit function might help to achieve better results, where the tumor is covered by other internal structures such as diaphragm for lower suited tumors.

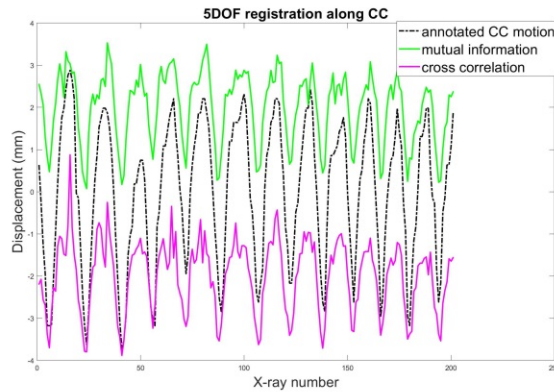


Figure 5.6: Performance of merit function compared for 5DOF registration of patient 20, Fr.1, g.a: 170°; cross-correlation (green) and rank correlation (magenta) are not in real scale and are plotted with offset from the breathing motion (dashed black) for a better visualization.

To further investigate the choice of merit function, cross-correlation and rank correlation were compared for other cases. As shown in figure 5.6, cross-correlation resulted in fewer errors and slightly better registration results. In the performed registrations within this study, the cross-correlation was the first choice of merit function. Cross-correlation often resulted in an improved signal, sometimes with lower displacement amplitude, compared to results obtained with mutual information. Cross-correlation was especially the choice for registration along the AP axis and considering that displacement along the AP axis had smaller amplitude, this could suggest that cross-correlation could outperform other merit functions for cases with smaller displacement amplitude. However, cross correlation was still sensitive to existing changes of intensity within the x-ray image sequence.

6 Conclusion

Intra-fraction tumor motion leads to a large PTV margin to account for the whole range of tumor motion. This large margin results in a higher dose to the healthy tissue and organs at risk. Currently, available motion management techniques are mostly invasive and fail in the presence of aperiodic breathing motion. 2D-3D registration of X-ray images, acquired during treatment, with DRR generated from planning CT is an alternative approach for real-time tumor motion monitoring. Tumor monitoring provides the possibility to choose a smaller PTV margin and instead compensate for tumor motion in real-time during the treatment session. To follow the tumor motion in 6DOF more than one set of projections is needed, otherwise, the motion along the beam axis is not resolved. This study has clearly shown that the displacement along the AP axis could sometimes reach 1.5 cm and become the dominant axis of tumor motion. Modern linac has the possibility of collecting the remaining treatment beam on a retractable detector behind the patient. This orthogonal projection of the tumor was paired and used as a second image set with no additional dose to the patient. The advantages of registration in 6DOF with an additional MV image set were investigated.

It was shown that registration with kV images could benefit from the kV-MV image pair for a better registration along the CC axis, plus this makes it possible to resolve motion along the imaging beam axis. Four up to seven gantry angles per fraction led to successful registration along the CC. Respectively, two to six gantry angles per fraction showed successful registration results along the AP axis. Tumor position, size, the extent of motion, and its trajectory impact the success of registration. Only for cases with optimal registration in 5DOF using kV images, the addition of an MV image set, where no tumor visibility was available, appeared as unnecessary. The most determining factor for the stability of the registration result at specific gantry angles was proven to be the tumor visibility, which was best achieved for uncovered solid tumors with lower intensity surrounding. It was shown that as long as some degree of tumor visibility existed within one of the x-ray image sets, a successful registration at any arbitrary gantry angles for displacement less than 1 cm along the CC axis and even as low as 1 mm along the AP axis was feasible.

There were many configuration parameters involved in the performance of a 2D-3D registration, such as the contrast of acquired x-ray images, existing structure within the selected ROI, choice of initial guess, merit function, and chosen intensity window for ROI. The challenges of motion extraction, alignment of kV-MV image pair, as well as the limitation of using diaphragm motion as a reference signal for validation of registration

results, particularly for tumors situated in the lung apex, were discussed and the need for a better gold standard was highlighted. Also, considering that the choice of initial guess could result in merit values being lower for wrong shifts, the process needs an operator to check the results, or a supplementary factor might be needed to make sure that the initial guess results in a meaningful motion extraction.

To improve the result furthermore; synchronized kV and MV image acquisition, 3D-3D registration of pre-treatment CT to daily CBCT for each fraction, selection of larger ROI and the possibility of segmentation and removal of unwanted structure within the selected ROI for registration, selection of cross-correlation as merit function, improvement in motion extraction approach and a better gold standard were suggested as the next required steps. Last but not least, the addition of a weighting factor for the X-ray image set in the 2D-3D registration software could help to increase the contribution of the image set with better tumor visibility. Overcoming the current limitations result in a robust real-time implementation of the intensity-based 2D-3D registration as a noninvasive tumor tracking technique in the treatment of motion-afflicted tumors.

6.1 Tumor Illustration with MV Projections

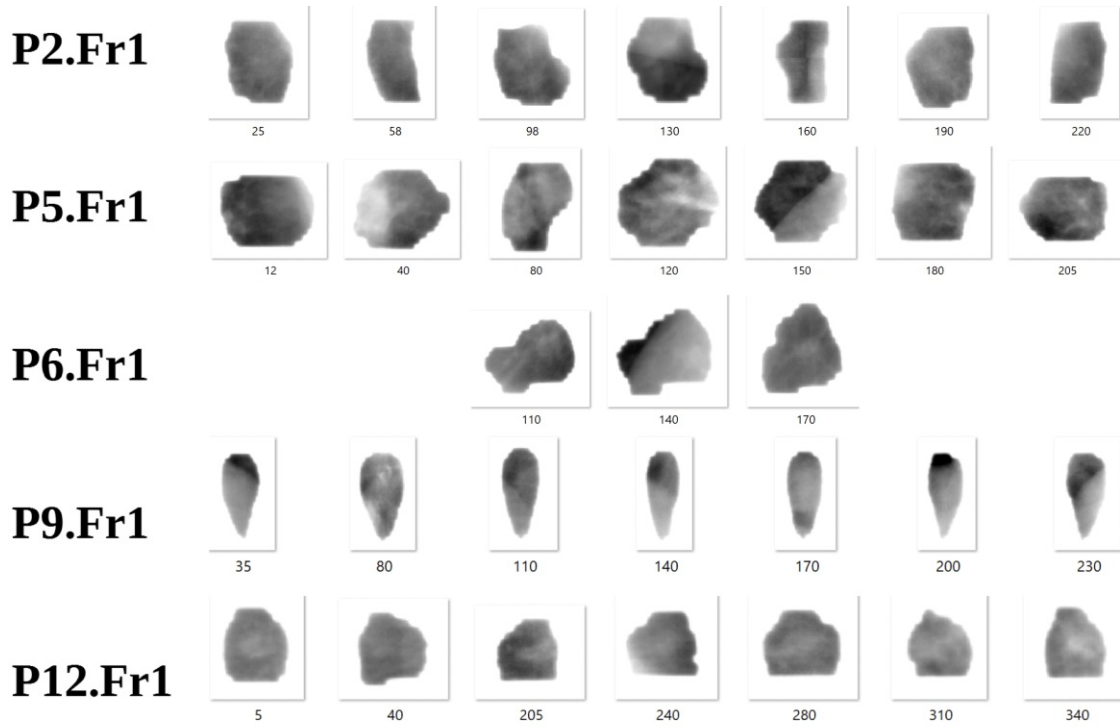


Figure 6.1: The twentieth projection from the MV image set, shown for all gantry angles of the first treatment fraction.

6.2 Patient 2

Patient 2 _ Fr.1, aligned kV-MV image pairs

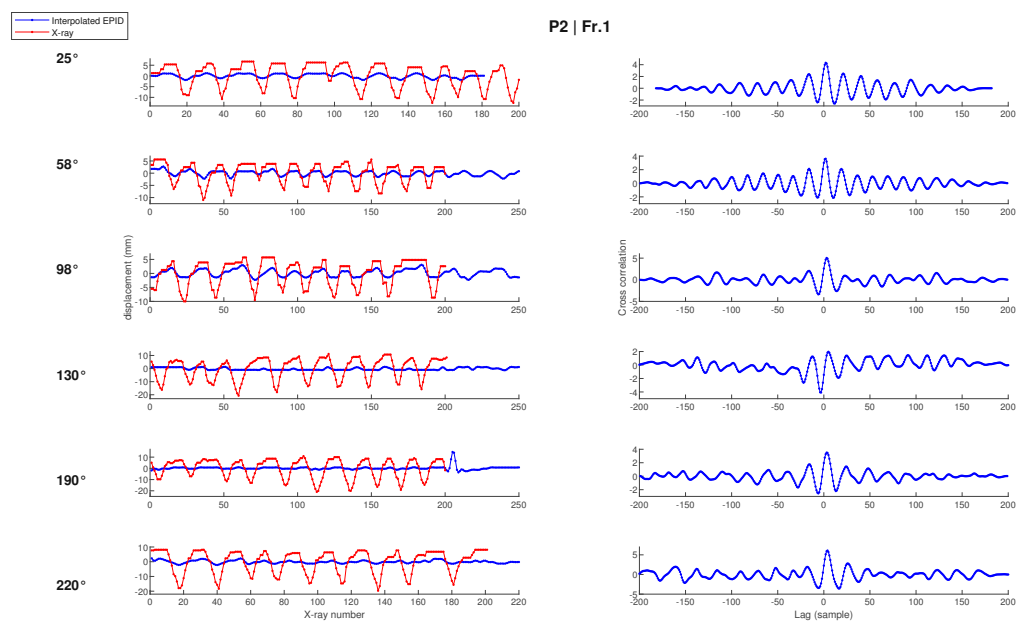


Figure 6.2: Patient 2 _ Fr.1, aligned kV-MV image pairs

The left column shows kV (red) and the interpolated MV (blue) motion signals, the right column shows the correlation between the two signals.

Patient 2 _ Fr.1

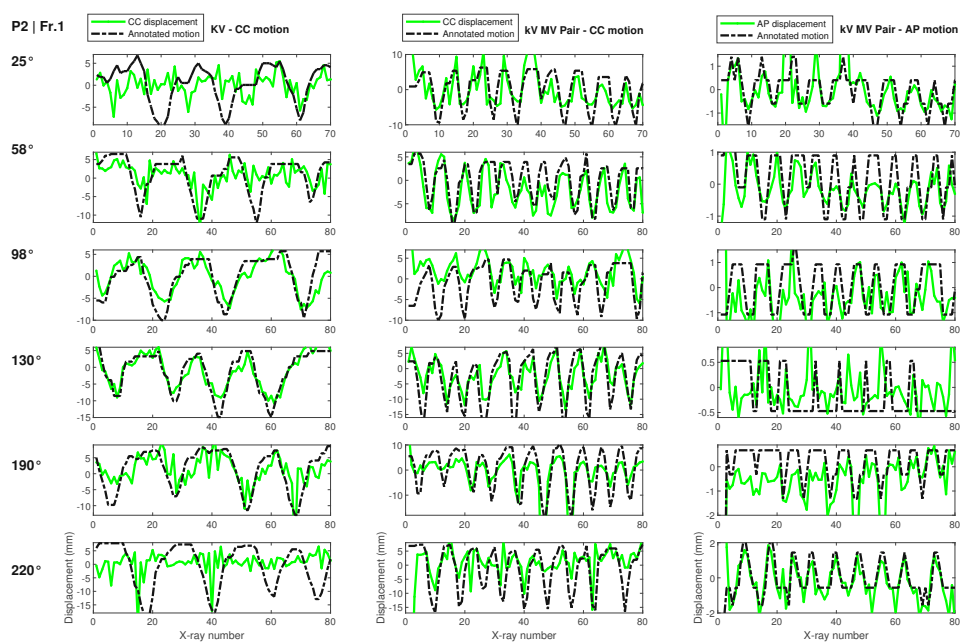


Figure 6.3: Patient 2 _ Fr.1,

The left column shows registration result in 5DOF along Ty axis for kV image set (green) vs. diaphragm motion in CC axis (black).

The middle column shows registration result in 6DOF along Ty axis for kV-MV image pair (green) vs. extracted tumor motion in CC axis (black).

The right column shows registration result in 6DOF along Tz axis for kV-MV image pair (green) vs. extracted tumor motion in AP axis (black).

Patient 2 _ Fr.2, aligned kV-MV image pairs

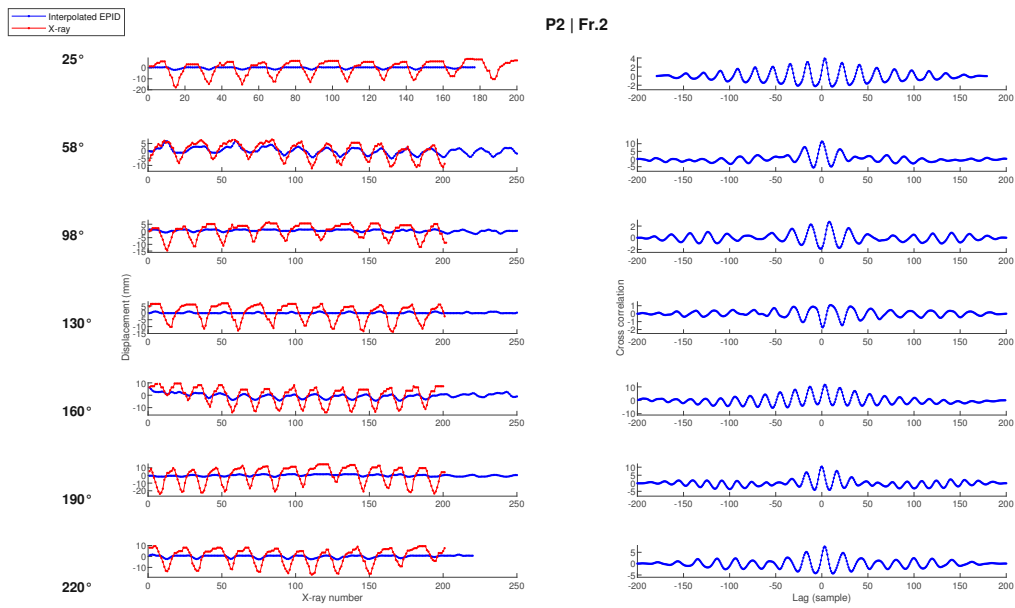


Figure 6.4: P2 _ Fr.2, aligned kV-MV image pairs

The left column shows kV (red) and the interpolated MV (blue) motion signals, the right column shows the correlation between the two signals.

Patient 2 _ Fr.2

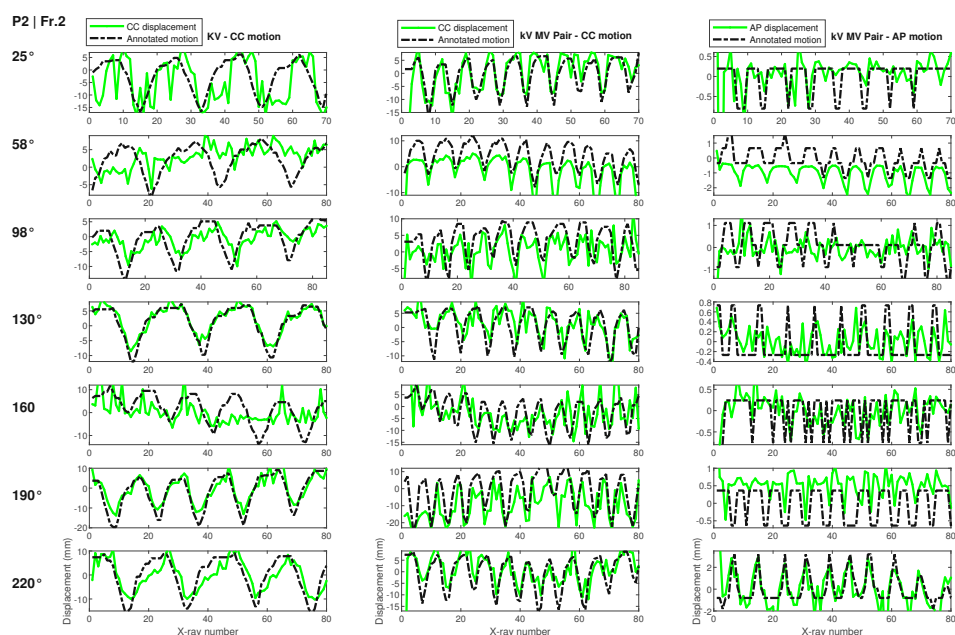


Figure 6.5: Patient 2 _ Fr.2,

The left column shows registration result in 5DOF along Ty axis for kV image set (green) vs. diaphragm motion in CC axis (black).

The middle column shows registration result in 6DOF along Ty axis for kV-MV image pair (green) vs. extracted tumor motion in CC axis (black).

The right column shows registration result in 6DOF along Tz axis for kV-MV image pair (green) vs. extracted tumor motion in AP axis (black).

Patient 2 _ Fr.3, aligned kV-MV image pairs

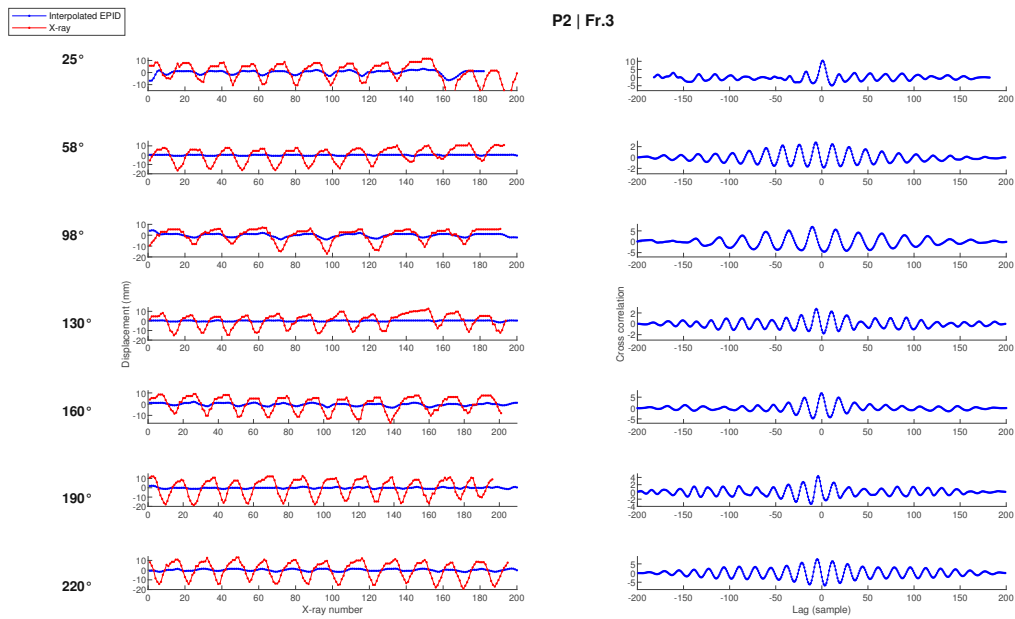


Figure 6.6: Patient 2 _ Fr.3, aligned kV-MV image pairs

The left column shows kV (red) and the interpolated MV (blue) motion signals, the right column shows the correlation between the two signals.

Patient 2 _ Fr.3

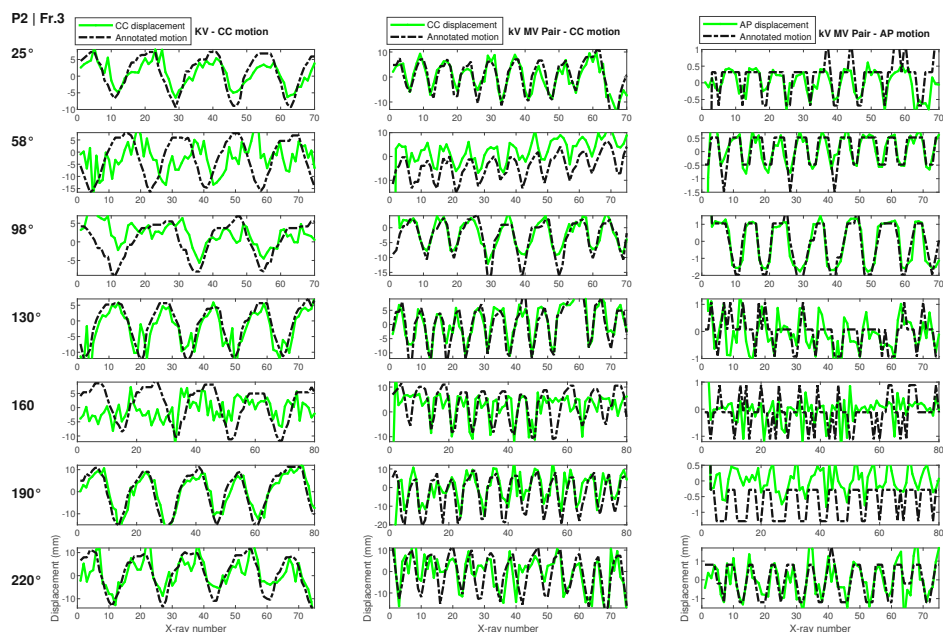


Figure 6.7: Patient 2 _ Fr.3,

The left column shows registration result in 5DOF along Ty axis for kV image set (green) vs. diaphragm motion in CC axis (black).

The middle column shows registration result in 6DOF along Ty axis for kV-MV image pair (green) vs. extracted tumor motion in CC axis (black).

The right column shows registration result in 6DOF along Tz axis for kV-MV image pair (green) vs. extracted tumor motion in AP axis (black).

6.3 Patient 5

Patient 5 _ Fr.1, aligned kV-MV image pairs

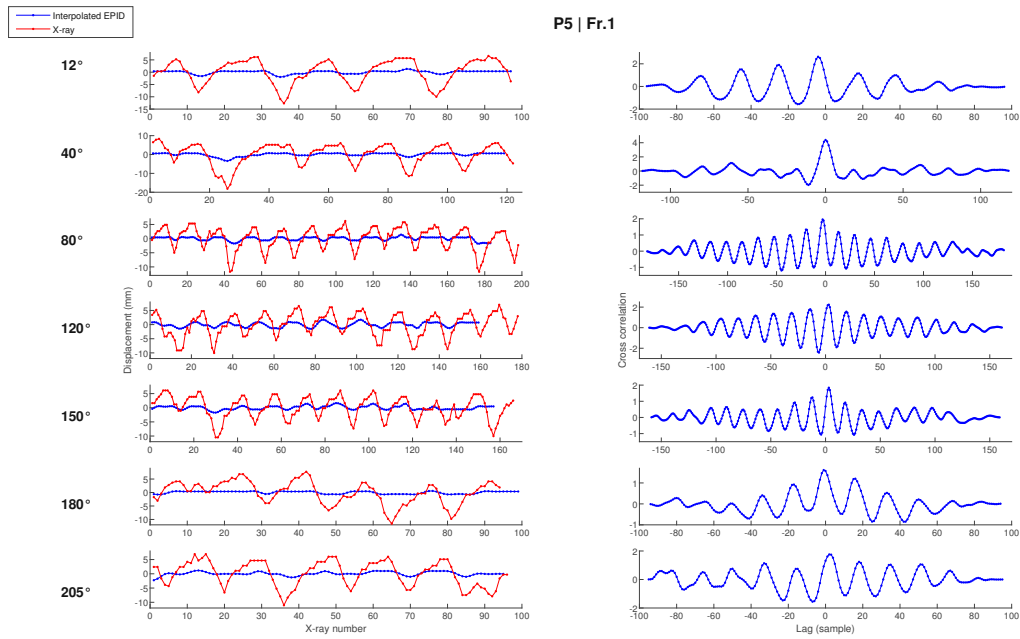


Figure 6.8: Patient 5 _ Fr.1, aligned kV-MV image pairs

The left column shows kV (red) and the interpolated MV (blue) motion signals, the right column shows the correlation between the two signals.

Patient 5 _ Fr.1

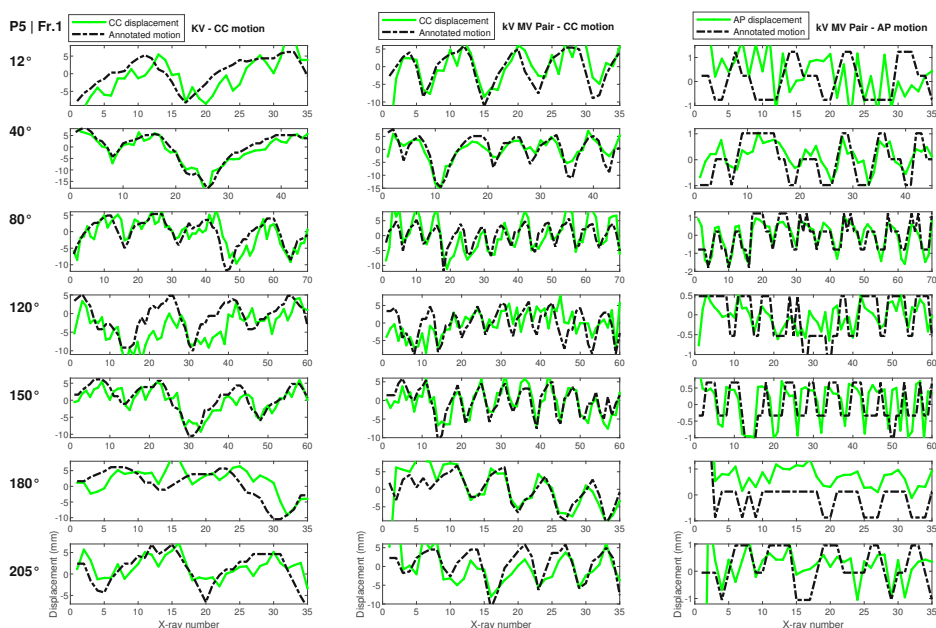


Figure 6.9: Patient 5 _ Fr.1,

The left column shows registration result in 5DOF along Ty axis for kV image set (green) vs. diaphragm motion in CC axis (black).

The middle column shows registration result in 6DOF along Ty axis for kV-MV image pair (green) vs. extracted tumor motion in CC axis (black).

The right column shows registration result in 6DOF along Tz axis for kV-MV image pair (green) vs. extracted tumor motion in AP axis (black).

Patient 5 _ Fr.2, aligned kV-MV image pairs

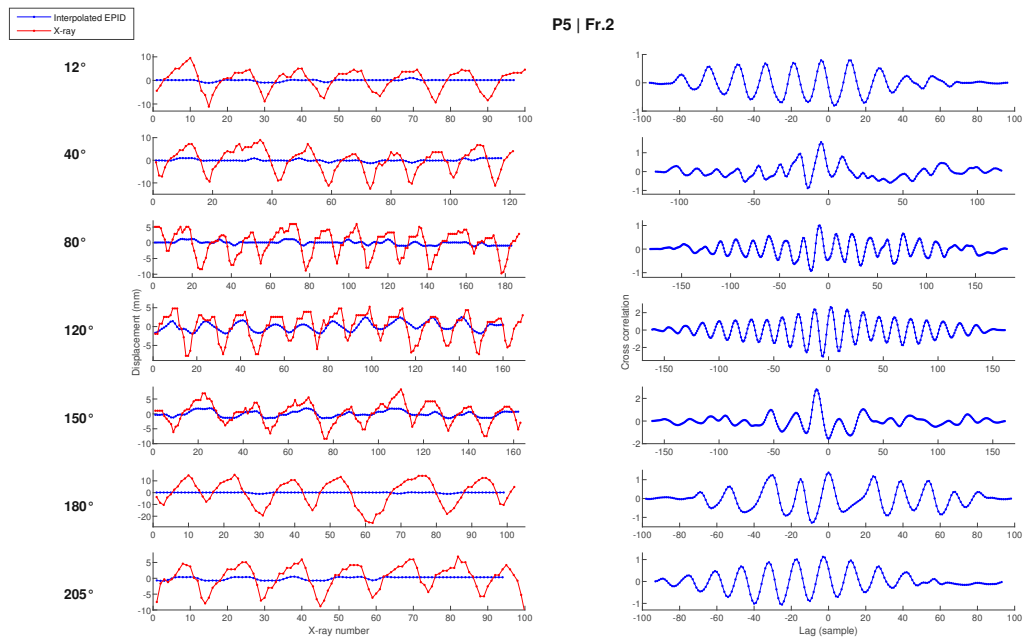


Figure 6.10: Patient 5 _ Fr.2, aligned kV-MV image pairs

The left column shows kV (red) and the interpolated MV (blue) motion signals, the right column shows the correlation between the two signals.

Patient 5 _ Fr.2

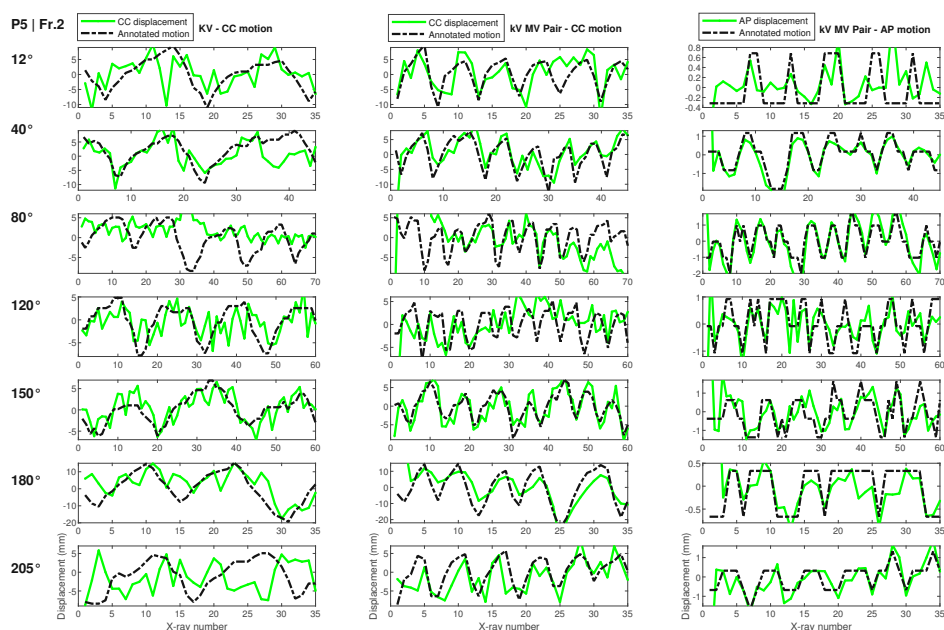


Figure 6.11: Patient 5 _ Fr.2,

The left column shows registration result in 5DOF along T_y axis for kV image set (green) vs. diaphragm motion in CC axis (black).

The middle column shows registration result in 6DOF along T_y axis for kV-MV image pair (green) vs. extracted tumor motion in CC axis (black).

The right column shows registration result in 6DOF along T_z axis for kV-MV image pair (green) vs. extracted tumor motion in AP axis (black).

Patient 5 _ Fr.3, aligned kV-MV image pairs

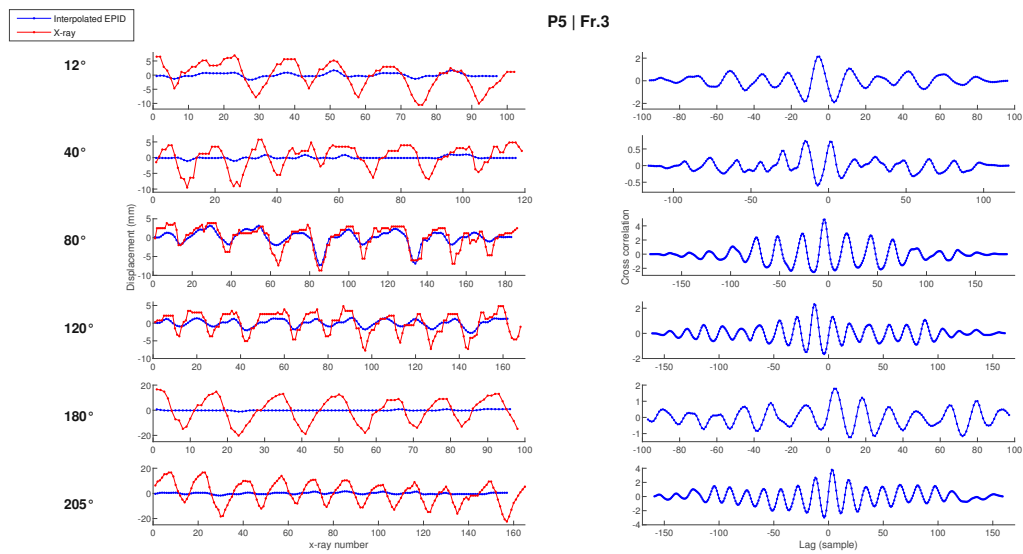


Figure 6.12: Patient 5 _ Fr.3, aligned kV-MV image pairs

The left column shows kV (red) and the interpolated MV (blue) motion signals, the right column shows the correlation between the two signals.

Patient 5 _ Fr.3

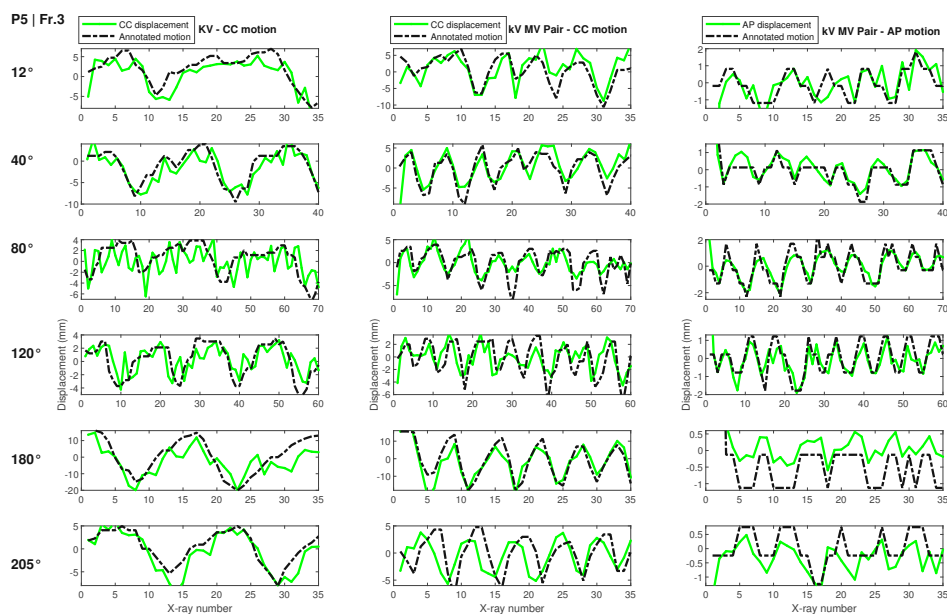


Figure 6.13: Patient 5 _ Fr.3,

The left column shows registration result in 5DOF along Ty axis for kV image set (green) vs. diaphragm motion in CC axis (black).

The middle column shows registration result in 6DOF along Ty axis for kV-MV image pair (green) vs. extracted tumor motion in CC axis (black).

The right column shows registration result in 6DOF along Tz axis for kV-MV image pair (green) vs. extracted tumor motion in AP axis (black).

6.4 Patient 6

Patient 6 _ Fr.1, aligned kV-MV image pairs

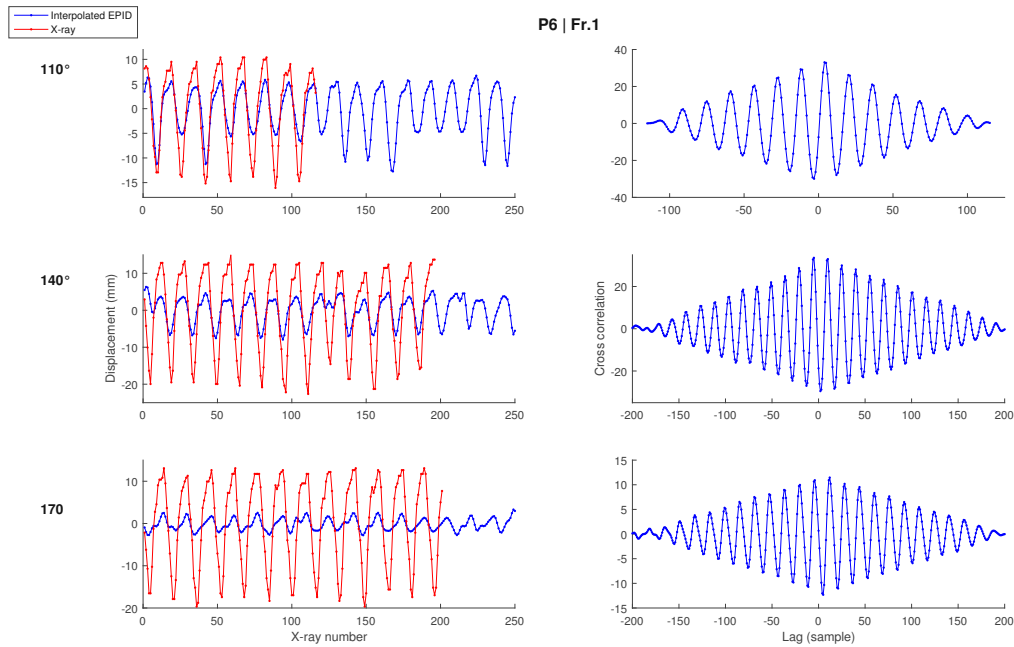


Figure 6.14: Patient 6 _ Fr.1, aligned kV-MV image pairs

The left column shows kV (red) and the interpolated MV (blue) motion signals, the right column shows the correlation between the two signals.

Patient 6 _ Fr.1

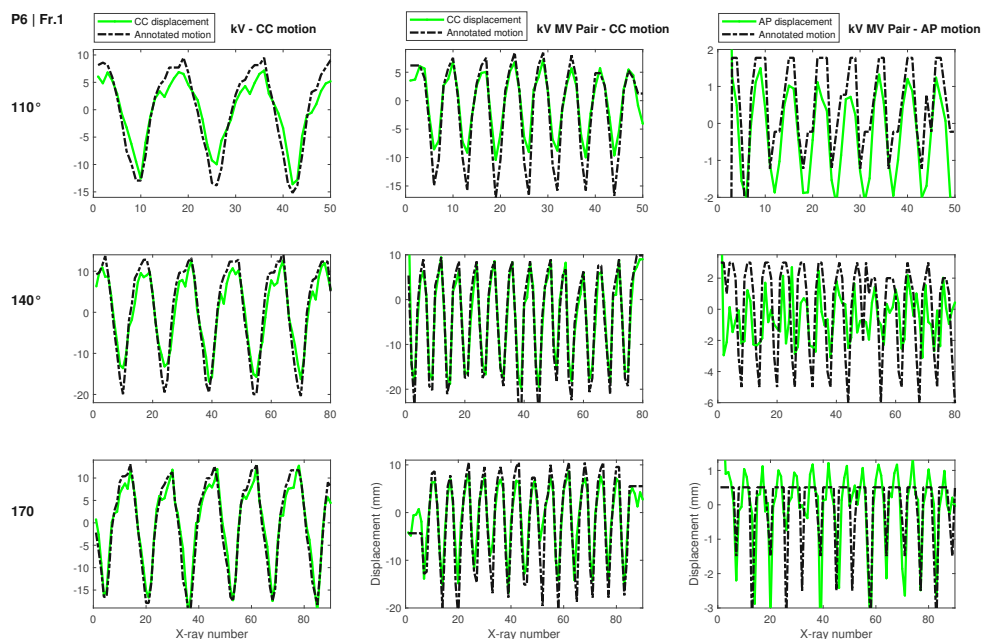


Figure 6.15: Patient 6 _ Fr.1,

The left column shows registration result in 5DOF along Ty axis for kV image set (green) vs. diaphragm motion in CC axis (black).

The middle column shows registration result in 6DOF along Ty axis for kV-MV image pair (green) vs. extracted tumor motion in CC axis (black).

The right column shows registration result in 6DOF along Tz axis for kV-MV image pair (green) vs. extracted tumor motion in AP axis (black).

6.5 Patient 9

Patient 9 _ Fr.1, aligned kV-MV image pairs

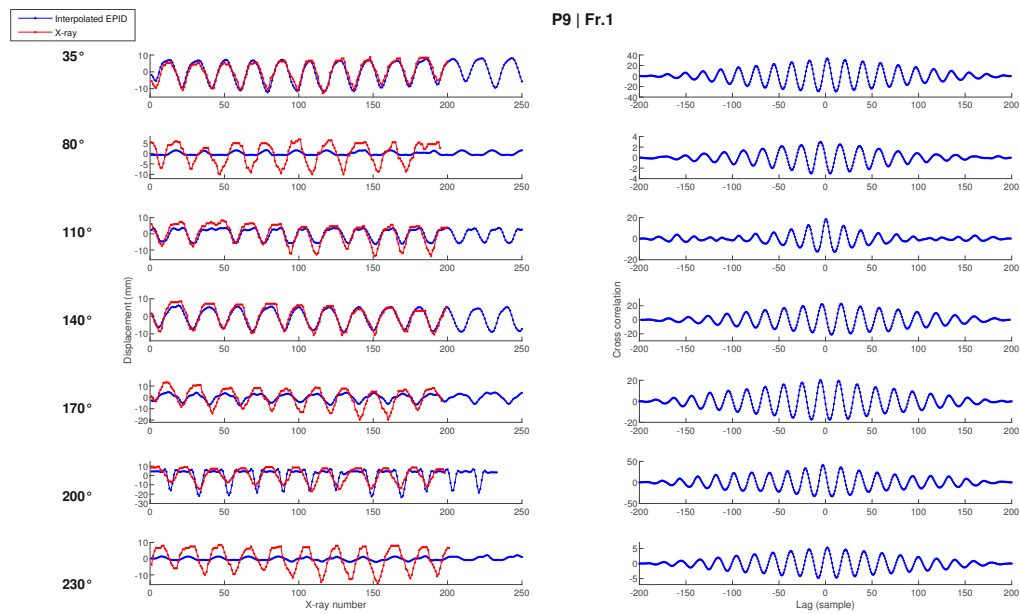


Figure 6.16: Patient 9 _ Fr.1, aligned kV-MV image pairs

The left column shows kV (red) and the interpolated MV (blue) motion signals, the right column shows the correlation between the two signals.

Patient 9 _ Fr.1

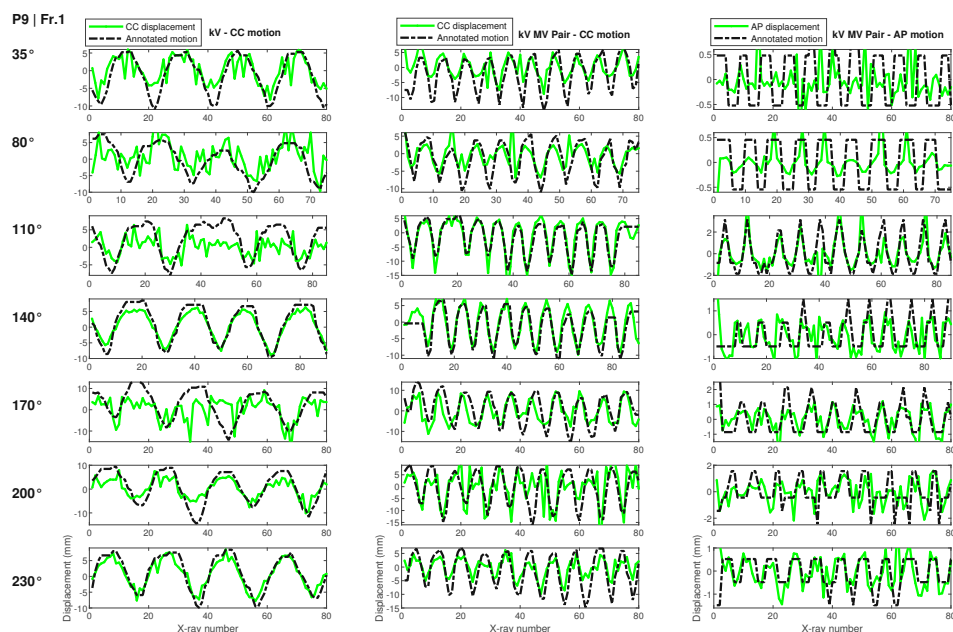


Figure 6.17: Patient 9 _ Fr.1,

The left column shows registration result in 5DOF along Ty axis for kV image set (green) vs. diaphragm motion in CC axis (black).

The middle column shows registration result in 6DOF along Ty axis for kV-MV image pair (green) vs. extracted tumor motion in CC axis (black).

The right column shows registration result in 6DOF along Tz axis for kV-MV image pair (green) vs. extracted tumor motion in AP axis (black).

Patient 9 _ Fr.2, aligned kV-MV image pairs

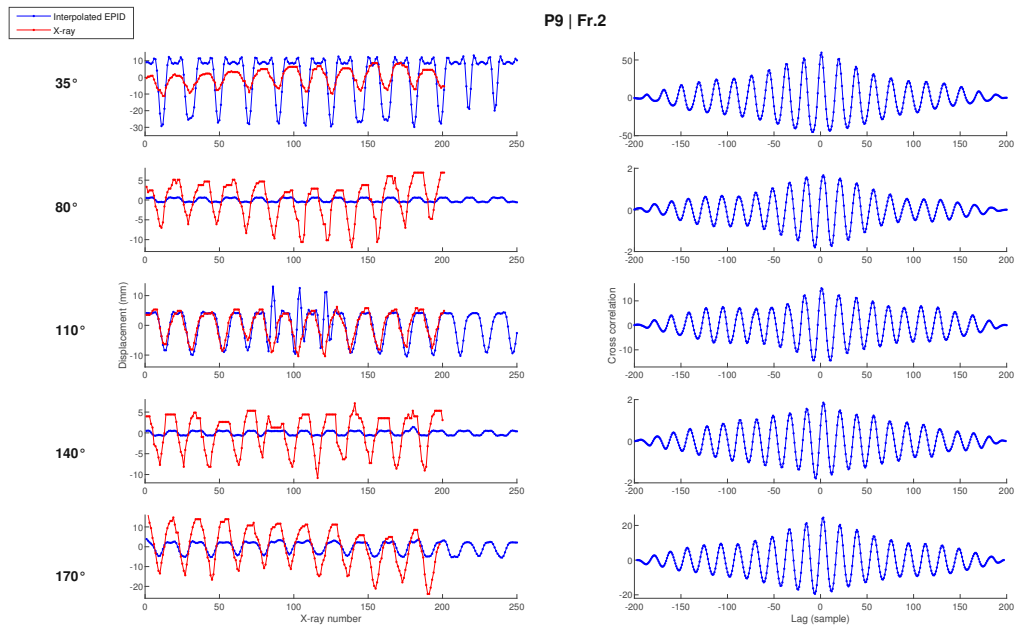


Figure 6.18: Patient 9 _ Fr.2, aligned kV-MV image pairs

The left column shows kV (red) and the interpolated MV (blue) motion signals, The right column shows the correlation between the two signals.

Patient 9 _ Fr.2

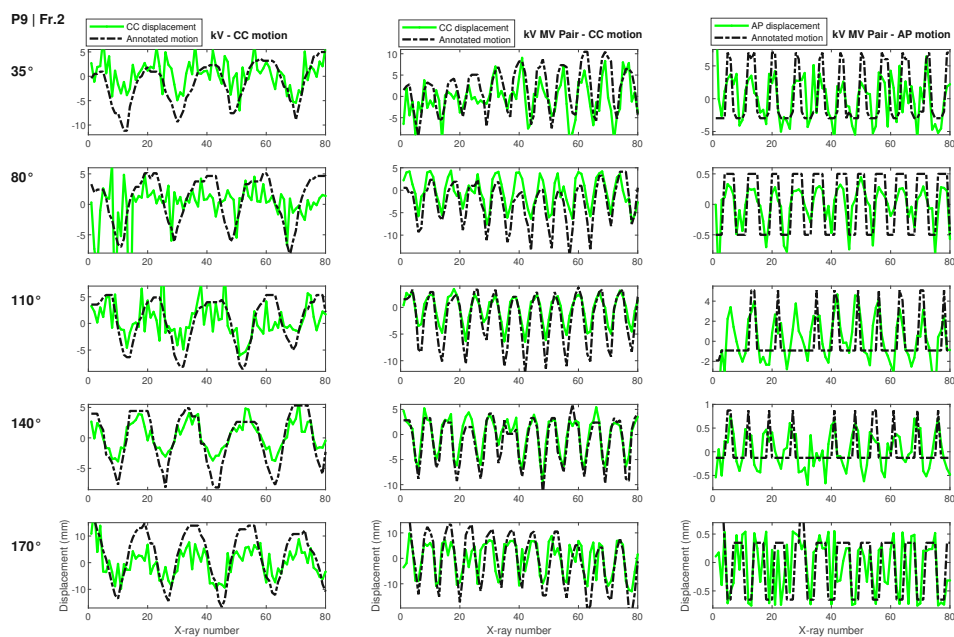


Figure 6.19: Patient 9 _ Fr.2,

The left column shows registration result in 5DOF along Ty axis for kV image set (green) vs. diaphragm motion in CC axis (black).

The Middle column shows registration result in 6DOF along Ty axis for kV-MV image pair (green) vs. extracted tumor motion in CC axis (black).

The right column shows registration result in 6DOF along Tz axis for kV-MV image pair (green) vs. extracted tumor motion in AP axis (black).

Patient 9 _ Fr.3, aligned kV-MV image pairs

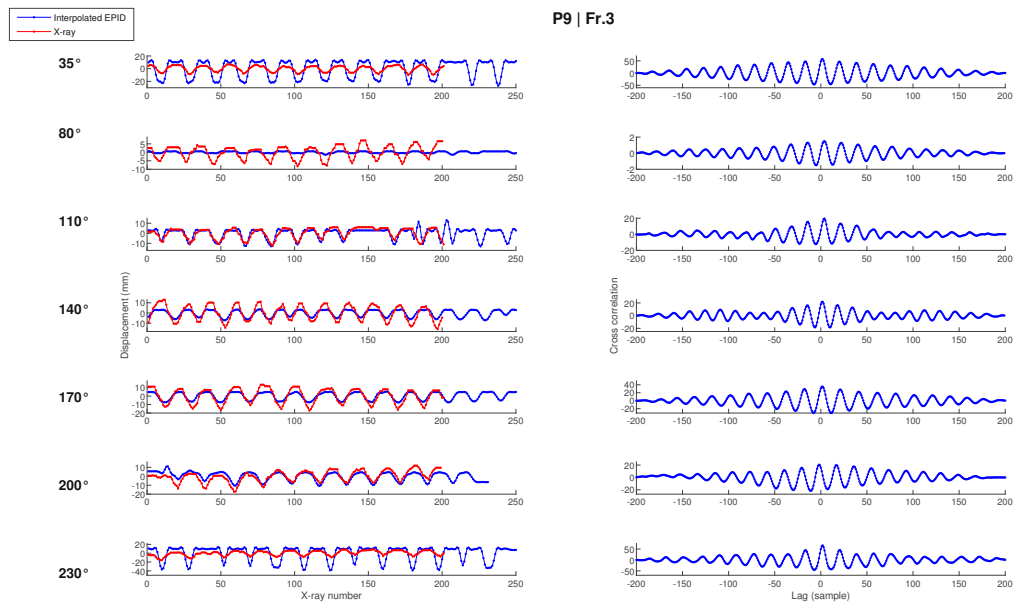


Figure 6.20: Patient 9 _ Fr.3, aligned kV-MV image pairs

The left column shows kV (red) and the interpolated MV (blue) motion signals, the right column shows the correlation between the two signals.

Patient 9 _ Fr.3

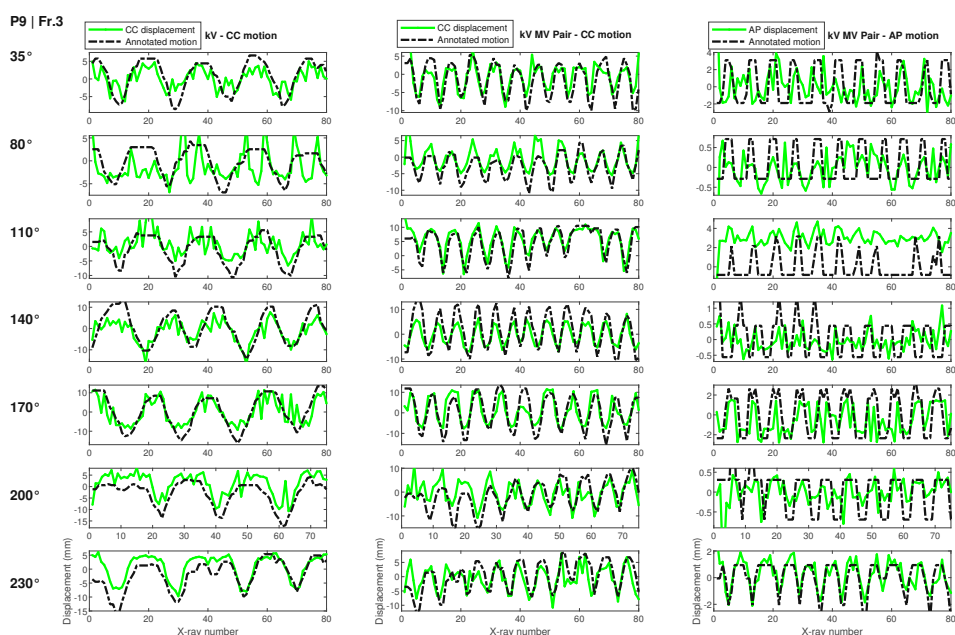


Figure 6.21: Patient 9 _ Fr.3,

The left column shows registration result in 5DOF along Ty axis for kV image set (green) vs. diaphragm motion in CC axis (black).

The middle column shows registration result in 6DOF along Ty axis for kV-MV image pair (green) vs. extracted tumor motion in CC axis (black).

The right column shows registration result in 6DOF along Tz axis for kV-MV image pair (green) vs. extracted tumor motion in AP axis (black).

6.6 Patient 12

Patient 12 _ Fr.1, aligned kV-MV image pairs

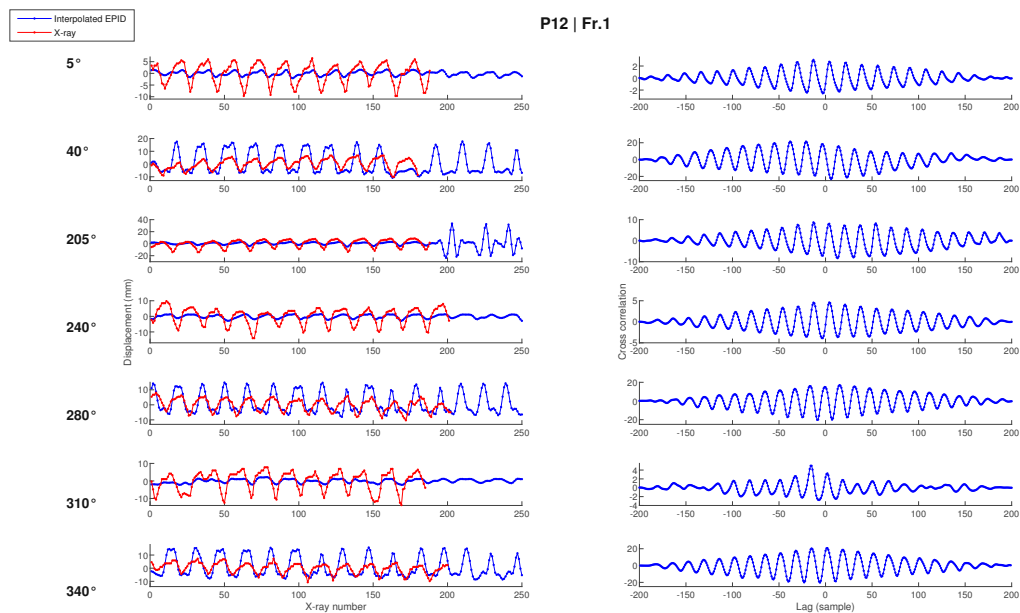


Figure 6.22: Patient 12 _ Fr.1, aligned kV-MV image pairs

The left column shows kV (red) and the interpolated MV (blue) motion signals, the right column shows the correlation between the two signals.

Patient 12 _ Fr.1

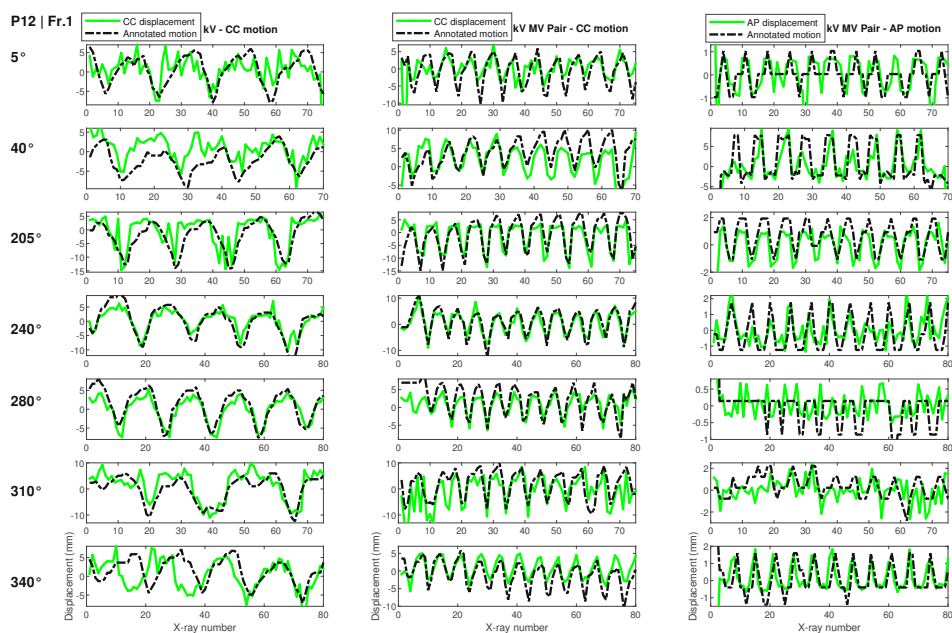


Figure 6.23: Patient 12 _ Fr.1,

The left column shows registration result in 5DOF along Ty axis for kV image set (green) vs. diaphragm motion in CC axis (black).

The middle column shows registration result in 6DOF along Ty axis for kV-MV image pair (green) vs. extracted tumor motion in CC axis (black).

The right column shows registration result in 6DOF along Tz axis for kV-MV image pair (green) vs. extracted tumor motion in AP axis (black).

Patient 12 _ Fr.2, aligned kV-MV image pairs

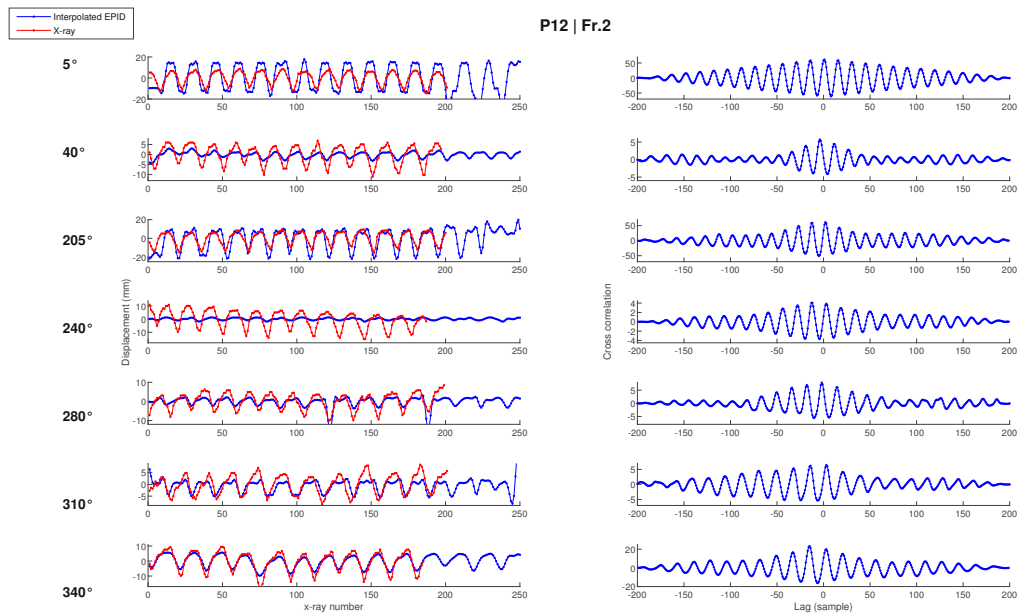


Figure 6.24: Patient 12 _ Fr.2, aligned kV-MV image pairs

The left column shows kV (red) and the interpolated MV (blue) motion signals, the right column shows the correlation between the two signals.

Patient 12 _ Fr.2

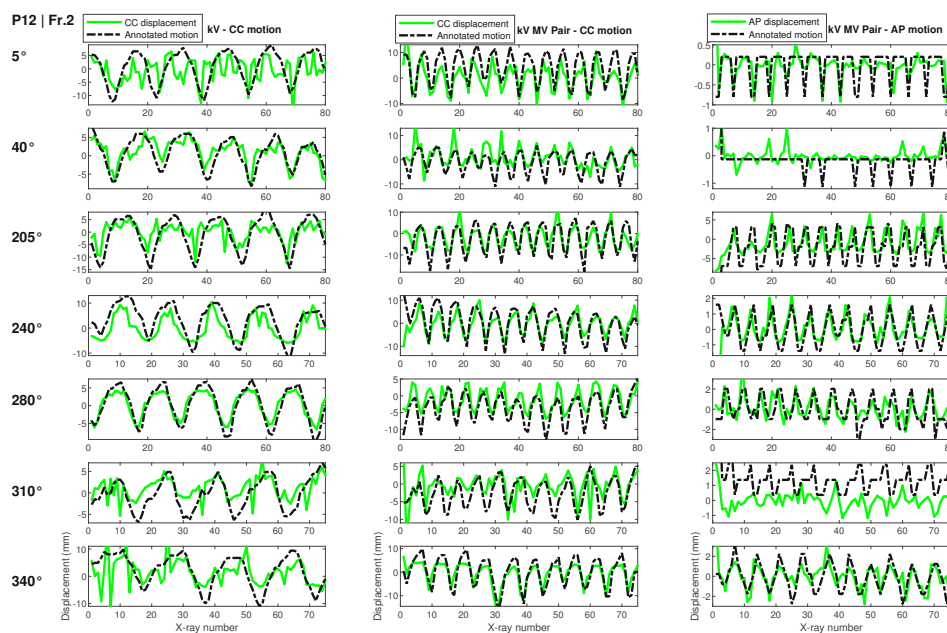


Figure 6.25: Patient 12 _ Fr.2,

The left column shows registration result in 5DOF along Ty axis for kV image set (green) vs. diaphragm motion in CC axis (black).

The middle column shows registration result in 6DOF along Ty axis for kV-MV image pair (green) vs. extracted tumor motion in CC axis (black).

The right column shows registration result in 6DOF along Tz axis for kV-MV image pair (green) vs. extracted tumor motion in AP axis (black).

Patient 12 _ Fr.3, aligned kV-MV image pairs

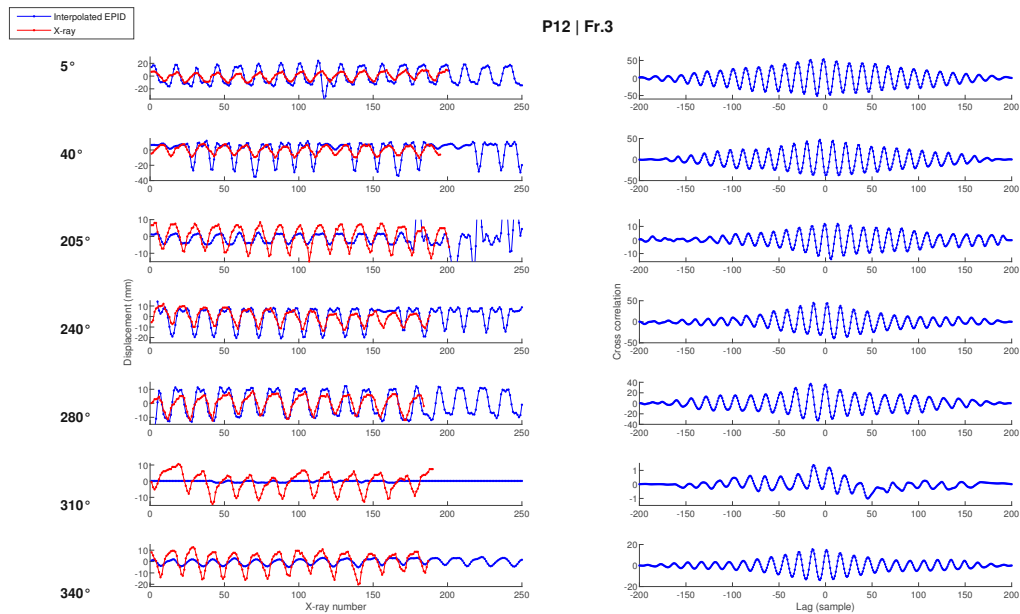


Figure 6.26: Patient 12 _ Fr.3, aligned kV-MV image pairs

The left column shows kV (red) and the interpolated MV (blue) motion signals, the right column shows the correlation between the two signals.

Patient 12 _ Fr.3

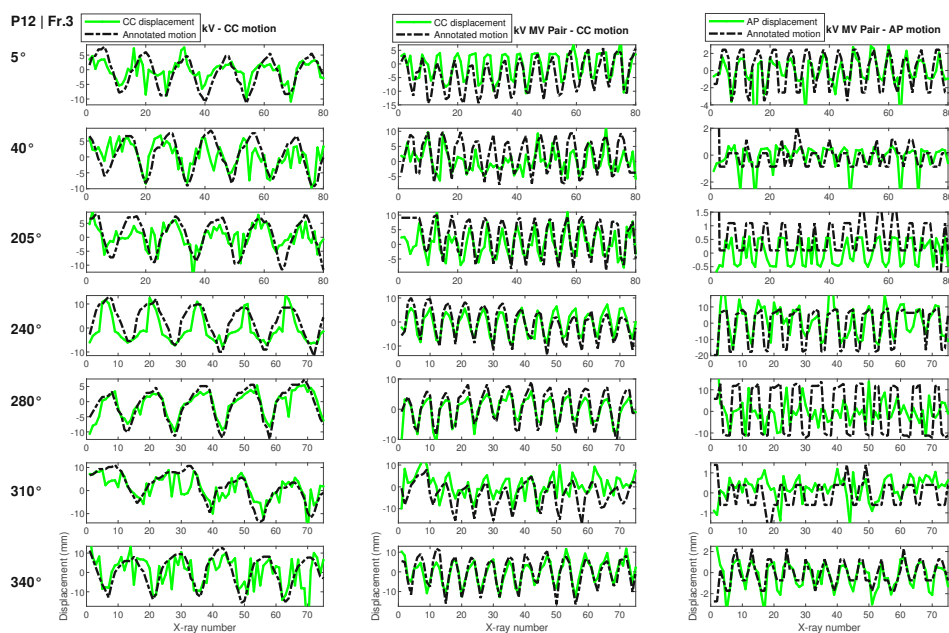


Figure 6.27: Patient 12 _ Fr.3,

The left column shows registration result in 5DOF along Ty axis for kV image set (green) vs. diaphragm motion in CC axis (black).

The middle column shows registration result in 6DOF along Ty axis for kV-MV image pair (green) vs. extracted tumor motion in CC axis (black).

The right column shows registration result in 6DOF along Tz axis for kV-MV image pair (green) vs. extracted tumor motion in AP axis (black).

Bibliography

- [1] *IGRT-online course*. URL <https://igrtonline.com>.
- [2] *Matlab Help*. URL <https://de.mathworks.com/help/matlab/ref/corrcoef.html>.
- [3] *radiologykey*. URL <https://radiologykey.com/respiratory-motion-management/#Fig2>.
- [4] Report 83. *Journal of the International Commission on Radiation Units and Measurements*, 10(1):NP, 2010. doi: 10.1093/jicru/10.1.Report83. URL <http://dx.doi.org/10.1093/jicru/10.1.Report83>.
- [5] *Accuracy Requirements and Uncertainties in Radiotherapy*. Number 31 in Human Health Series. INTERNATIONAL ATOMIC ENERGY AGENCY, Vienna, 2016. ISBN 978-92-0-100815-2. URL <https://www.iaea.org/publications/10668/accuracy-requirements-and-uncertainties-in-radiotherapy>.
- [6] W. Birkfellner. *Applied Medical Image Processing*. Boca Raton: CRC Press., 2014.
- [7] Wolfgang Birkfellner, Michael Figl, Joachim Kettenbach, Johann Hummel, Peter Homolka, Rüdiger Schernthaner, Thomas Nau, and Helmar Bergmann. Rigid 2d/3d slice-to-volume registration and its application on fluoroscopic ct images. *Medical Physics*, 34(1):246–255. doi: 10.1118/1.2401661. URL <https://aapm.onlinelibrary.wiley.com/doi/abs/10.1118/1.2401661>.
- [8] Wolfgang Birkfellner, Markus Stock, Michael Figl, Christelle Gendrin, Johann Hummel, Shuo Dong, Joachim Kettenbach, Dietmar Georg, and Helmar Bergmann. Stochastic rank correlation: A robust merit function for 2d/3d registration of image data obtained at different energies. *Medical physics*, 36(8):3420–3428, 2009.
- [9] Jean-Pierre Bissonnette, Peter A. Balter, Lei Dong, Katja M. Langen, D. Michael Lovelock, Moyed Miften, Douglas J. Moseley, Jean Pouliot, Jan-Jakob Sonke, and Sua Yoo. Quality assurance for image-guided radiation therapy utilizing ct-based technologies: A report of the aapm tg-179. *Medical Physics*, 39(4):1946–1963, 2012. doi: <https://doi.org/10.1118/1.3690466>. URL <https://aapm.onlinelibrary.wiley.com/doi/abs/10.1118/1.3690466>.
- [10] Kristy K Brock, Sasa Mutic, Todd R McNutt, Hua Li, and Marc L Kessler. Use of image registration and fusion algorithms and techniques in radiotherapy: Report of the aapm radiation therapy committee task group no. 132. *Medical physics*, 44(7):e43–e76, 2017.

- [11] Alexis Bujold, Tim Craig, David Jaffray, and Laura A Dawson. Image-guided radiotherapy: has it influenced patient outcomes? *Seminars in radiation oncology*, 22(1):50–61, January 2012. ISSN 1053-4296. doi: 10.1016/j.semradonc.2011.09.001. URL <https://doi.org/10.1016/j.semradonc.2011.09.001>.
- [12] Gary E Christensen, Xiujian Geng, Jon G Kuhl, Joel Bruss, Thomas J Grabowski, Imran A Pirwani, Michael W Vannier, John S Allen, and Hanna Damasio. Introduction to the non-rigid image registration evaluation project (nirep). In *International workshop on biomedical image registration*, pages 128–135. Springer, 2006.
- [13] A. J. Cole, G. G. Hanna, S. Jain, and J. M. O’Sullivan. Motion management for radical radiotherapy in non-small cell lung cancer. *Clinical Oncology*, 26(2): 67–80, February 2014. ISSN 0936-6555. doi: 10.1016/j.clon.2013.11.001. URL <https://doi.org/10.1016/j.clon.2013.11.001>.
- [14] Nicolas de Cillia. Feasibility and accuracy of 2d/3d registration for tumor motion tracking in image guided radiotherap. Master’s thesis, TUWien, 2015.
- [15] Frank C. Detterbeck, Daniel Joseph Boffa, Anthony W Kim, and Lynn T. Tanoue. The eighth edition lung cancer stage classification. *Chest*, 151 1:193–203, 2017.
- [16] M Figl, C Bloch, C Gendrin, C Weber, SA Pawiro, J Hummel, P Markelj, F Pernuš, H Bergmann, and W Birkfellner. Efficient implementation of the rank correlation merit function for 2d/3d registration. *Physics in Medicine & Biology*, 55(19):N465, 2010.
- [17] H Furtado, E Steiner, M Figl, M Stock, D Georg, and W Birkfellner. Pd-0576: Improved 2d/3d registration accuracy for tumor motion tracking using kv-mv image pairs in image guided radiotherapy. *Radiotherapy and Oncology*, 106:S221, 2013.
- [18] H Furtado, C Gendrin, J Spoerk, M Figl, D Georg, and W Birkfellner. Po-0930: Flirt: a software suite for real-time 2d/3d image registration for image guided radiotherapy. *Radiotherapy and Oncology*, 115:S485, 2015.
- [19] H. Furtado, Yvette Seppenwoolde, Elisabeth Steiner, M. Bsteh, Wolfgang Birkfellner, and D. Georg. Motion management for partial arc vmat treatments using intra-fractional 2d/3d registration. volume 119, pages S95–S96, 04 2016. doi: 10.1016/S0167-8140(16)31459-1.
- [20] Hugo Furtado, Christelle Gendrin, Christoph Bloch, Jakob Spoerk, Suprianto A Pawiro, Christoph Weber, Michael Figl, Helmar Bergmann, Markus Stock, Dietmar Georg, et al. Real-time intensity based 2d/3d registration for tumor motion tracking during radiotherapy. In *Bildverarbeitung für die Medizin 2012*, pages 207–212. Springer, 2012.
- [21] Hugo Furtado, Elisabeth Steiner, Markus Stock, Dietmar Georg, and Wolfgang Birkfellner. Real-time 2d/3d registration using kv-mv image pairs for tumor motion tracking in image guided radiotherapy. *Acta Oncologica*, 52(7):1464–1471, 2013.

- [22] Hugo Furtado, Elisabeth Steiner, Markus Stock, Dietmar Georg, and Wolfgang Birkfellner. Real-time intensity based 2d/3d registration using kv-mv image pairs for tumor motion tracking in image guided radiotherapy. In *Medical Imaging: Image Processing*, 2014.
- [23] Stock M Georg D Birkfellner W Furtado H, Figl M. Improved accuracy in 2d/3d registration for image guided radiotherapy by using kv-mv image pairs.
- [24] Christelle Gendrin, Hugo Furtado, Christoph Weber, Christoph Bloch, Michael Figl, Supriyanto Ardjo Pawiro, Helmar Bergmann, Markus Stock, Gabor Fichtinger, Dietmar Georg, et al. Monitoring tumor motion by real time 2d/3d registration during radiotherapy. *Radiotherapy and oncology*, 102(2):274–280, 2012.
- [25] Shikha Goyal and Tejinder Kataria. “image guidance in radiation therapy: Techniques and applications,”. *Radiology Research and Practice*, (705604):10, 2014. URL <http://dx.doi.org/10.1155/2014/705604>.
- [26] B. A. Groh, J. H. Siewerdsen, D. G. Drake, J. W. Wong, and D. A. Jaffray. A performance comparison of flat-panel imager-based mv and kv cone-beam ct. *Medical Physics*, 29(6):967–975. doi: 10.1118/1.1477234. URL <https://aapm.onlinelibrary.wiley.com/doi/abs/10.1118/1.1477234>.
- [27] AAPM Task Group. The role of in-room kv x-ray imaging for patient setup and target localization. techreport 104, American Association of Physicists in Medicine, 2009.
- [28] Roger A. Hälgl, Jürgen Besserer, and Uwe Schneider. Systematic measurements of whole-body imaging dose distributions in image-guided radiation therapy. *Medical Physics*, 39(12):7650–7661. doi: 10.1118/1.4758065. URL <https://aapm.onlinelibrary.wiley.com/doi/abs/10.1118/1.4758065>.
- [29] Stefan Hammerschmidt and Hubert Wirtz. Lung cancer: Current diagnosis and treatment. *Deutsches Ärzteblatt International*, 106(49):809–820, September 2009. ISSN 1866-0452. URL <http://www.ncbi.nlm.nih.gov/pmc/articles/PMC2797332/>.
- [30] Michael G. Herman, James M. Balter, David A. Jaffray, Kiarin P. McGee, Peter Munro, Shlomo Shalev, Marcel Van Herk, and John W. Wong. Clinical use of electronic portal imaging: Report of aapm radiation therapy committee task group 58. *Medical Physics*, 28(5):712–737, 2001. doi: <https://doi.org/10.1118/1.1368128>. URL <https://aapm.onlinelibrary.wiley.com/doi/abs/10.1118/1.1368128>.
- [31] INTERNATIONAL ATOMIC ENERGY AGENCY. *Radiation Oncology Physics*. INTERNATIONAL ATOMIC ENERGY AGENCY, Vienna, 2005. URL <http://www-pub.iaea.org/books/IAEABooks/7086/Radiation-Oncology-Physics>.

- [32] Paul J. Keall, Gig S. Mageras, James M. Balter, Richard S. Emery, Kenneth M. Forster, Steve B. Jiang, Jeffrey M. Kapatoes, Daniel A. Low, Martin J. Murphy, Brad R. Murray, Chester R. Ramsey, Marcel B. Van Herk, S. Sastry Vedam, John W. Wong, and Ellen Yorke. The management of respiratory motion in radiation oncology report of AAPM task group 76a). Technical Report 10, sep 2006. URL <https://doi.org/10.1118%2F1.2349696>.
- [33] Hunor Kertesz. Ardos phantom: reasearch applications including further developments. Master's thesis, FH Wiener Neustadt, 2016.
- [34] S S Korreman. Image-guided radiotherapy and motion management in lung cancer. *The British Journal of Radiology*, 88(1051):20150100, 2015. doi: 10.1259/bjr.20150100. URL <https://doi.org/10.1259/bjr.20150100>. PMID: 25955231.
- [35] Thomas Künzler, Jozef Grezdo, Joachim Bogner, Wolfgang Birkfellner, and Dietmar Georg. Registration of drrs and portal images for verification of stereotactic body radiotherapy: a feasibility study in lung cancer treatment. *Physics in medicine & biology*, 52(8):2157, 2007.
- [36] T. Landberg, J. Chavaudra, J. Dobbs, G. Hanks, K.-A. Johansson, T. Möller, and J. Purdy. Report 50. *Journal of the International Commission on Radiation Units and Measurements*, os26(1):NP, 1993. doi: 10.1093/jicru/os26.1.Report50. URL <http://dx.doi.org/10.1093/jicru/os26.1.Report50>.
- [37] T. Landberg, J. Chavaudra, J. Dobbs, J. P. Gerard, G. Hanks, J. C. Horiot, K. A. Johansson, T. Möller, J. Purdy, N. Suntharalingam, and H. Svensson. Report 62. *Journal of the International Commission on Radiation Units and Measurements*, os32(1):NP, 1999. doi: 10.1093/jicru/os32.1.Report62. URL <http://dx.doi.org/10.1093/jicru/os32.1.Report62>.
- [38] Michela Lecchi, Piero Fossati, Federica Elisei, Roberto Orecchia, and Giovanni Lucignani. Current concepts on imaging in radiotherapy. *European Journal of Nuclear Medicine and Molecular Imaging*, 35(4):821–837, Apr 2008. ISSN 1619-7089. doi: 10.1007/s00259-007-0631-y. URL <https://doi.org/10.1007/s00259-007-0631-y>.
- [39] Hassan Lemjabbar-Alaoui, Omer Hassan, Yi-Wei Yang, and Petra Buchanan. Lung cancer: biology and treatment options. *Biochimica et biophysica acta*, 1856(2):189–210, August 2015. ISSN 0006-3002. URL <http://www.ncbi.nlm.nih.gov/pmc/articles/PMC4663145/>.
- [40] JB Antoine Maintz and Max A Viergever. A survey of medical image registration. *Medical image analysis*, 2(1):1–36, 1998.
- [41] Primož Markelj, Dejan Tomaževič, Bostjan Likar, and Franjo Pernuš. A review of 3d/2d registration methods for image-guided interventions. *Medical image analysis*, 16(3):642–661, 2012.

- [42] Nahum A. (Ed.) Rosenwald J. (Ed.) Dale R. Evans P. Flower M. Nahum A. Aird E. Carlson G. Andreo P. Atthey M. Bidmead M. Blake P. Brunt J. Chapman D. Chavaudra J. Childs P. Greener T. Hansen V. Ingham D. Jakel O. Khoo V. Lord C. Loverock L. Ma C. Marinello G. Mazal A. McKay D. McKenzie A. Mubata C. Neal A. Oldham M. Rosenberg I. Rosenbloom M. Sage J. Saunders J. Shentall G. Steel G. Thwaites D. Warrington J. Webb S. Williams P. Rosenwald J.C. Jones C. Bielajew A. Dance D. Mayles, P. (Ed.). *Handbook of Radiotherapy Physics: Theory and Practice*. Boca Raton: CRC Press, 2007.
- [43] Martin J. Murphy, James Balter, Stephen Balter, Jose A. BenComo Jr., Indra J. Das, Steve B. Jiang, C.-M. Ma, Gustavo H. Olivera, Raymond F. Rodebaugh, Kenneth J. Ruchala, Hiroki Shirato, and Fang-Fang Yin. The management of imaging dose during image-guided radiotherapy: Report of the aapm task group 75. *Medical Physics*, 34(10):4041–4063, 2007. doi: <https://doi.org/10.1118/1.2775667>. URL <https://aapm.onlinelibrary.wiley.com/doi/abs/10.1118/1.2775667>.
- [44] Graeme P Penney, Jürgen Weese, John A Little, Paul Desmedt, Derek LG Hill, et al. A comparison of similarity measures for use in 2-d-3-d medical image registration. *IEEE transactions on medical imaging*, 17(4):586–595, 1998.
- [45] O.S. Pianykh. *Digital Imaging and Communications in Medicine (DICOM): A Practical Introduction and Survival Guide*. Springer Berlin Heidelberg, 2009. ISBN 9783642108501. URL <https://books.google.at/books?id=GpQmSXqhDcMC>.
- [46] Josien PW Pluim, JB Antoine Maintz, and Max A Viergever. Mutual-information-based registration of medical images: a survey. *IEEE transactions on medical imaging*, 22(8):986–1004, 2003.
- [47] William H Press, Brian P Flannery, Saul A Teukolsky, and William T Vetterling. Numerical recipes. *Cambridge University Press*, 78:134, 1990.
- [48] Yvette Seppenwoolde, Hiroki Shirato, Kei Kitamura, Shinichi Shimizu, Marcel van Herk, Joos V. Lebesque, and Kazuo Miyasaka. Precise and real-time measurement of 3d tumor motion in lung due to breathing and heartbeat, measured during radiotherapy. *International Journal of Radiation Oncology*Biophysics*, 53(4):822–834, 2002. ISSN 0360-3016. doi: [https://doi.org/10.1016/S0360-3016\(02\)02803-1](https://doi.org/10.1016/S0360-3016(02)02803-1). URL <https://www.sciencedirect.com/science/article/pii/S0360301602028031>.
- [49] Aristeidis Sotiras, Christos Davatzikos, and Nikos Paragios. Deformable medical image registration: A survey. *IEEE transactions on medical imaging*, 32(7):1153–1190, 2013.
- [50] Jakob Spörk. High-performance gpu based rendering for real-time, rigid 2d/3d - image registration in radiation oncology. Master’s thesis, TU Wien, 2010.
- [51] George Starkschall, Lei Dong, Peter A. Balter, Almon S. Shiu, Firas Mourtada, Michael Gillin, and Radhe Mohan. Chapter 2 - clinical radiation oncology physics. In

James D. Cox and K. Kian Ang, editors, *Radiation Oncology (Ninth Edition)*, pages 50 – 91. Content Repository Only!, Philadelphia, ninth edition edition, 2010. ISBN 978-0-323-04971-9. URL <http://www.sciencedirect.com/science/article/pii/B9780323049719000020>.

- [52] B.W. Stewart and C.P. Wild. *World Cancer Report 2014*. International Agency for Research on Cancer. International Agency for Research on Cancer, 2014. ISBN 9789283204299. URL <https://books.google.at/books?id=0QHbngEACAAJ>.
- [53] Markus Stock, Asa Palm, Andreas Altendorfer, Elisabeth Steiner, and Dietmar Georg. Igrt induced dose burden for a variety of imaging protocols at two different anatomical sites. *Radiotherapy and Oncology*, 102(3):355–363, March 2012. ISSN 0167-8140. doi: 10.1016/j.radonc.2011.10.005. URL <https://doi.org/10.1016/j.radonc.2011.10.005>.
- [54] Dejan Tomažević. *3D/2D Registration of Medical Images*. PhD thesis, 2008.
- [55] M van Herk, P Remeijer, C Rasch, and JV Lebesque. The probability of correct target dosage: dose-population histograms for deriving treatment margins in radiotherapy. *International journal of radiation oncology, biology, physics*, 47(4): 1121–1135, July 2000. ISSN 0360-3016. doi: 10.1016/s0360-3016(00)00518-6. URL [https://doi.org/10.1016/s0360-3016\(00\)00518-6](https://doi.org/10.1016/s0360-3016(00)00518-6).
- [56] Hansjoerg Wertz, Dzmitry Stsepankou, Manuel Blessing, Michael Rossi, Chris Knox, Kevin H. Brown, Uwe Gros, Judit Boda-Heggemann, Cornelia Walter, Jürgen W. Hesser, Frank Lohr, and Frederik Wenz. Fast kilovoltage/megavoltage (kvmv) breathhold cone-beam ct for image-guided radiotherapy of lung cancer. *Physics in medicine and biology*, 55 15:4203–17, 2010.
- [57] Wikipedia. 2018 . URL https://commons.wikimedia.org/wiki/File:Dose_Depth_Curves.svg#/media/File:Dose_Depth_Curves.svg.
- [58] Jae Chern Yoo and Tae Han. Fast normalized cross-correlation. *Circuits, Systems and Signal Processing*, 28:819–843, 12 2009. doi: 10.1007/s00034-009-9130-7.